The Dissertation Committee for Brendan Michael Elliott
Certifies that this is the approved version of the following Dissertation:

Wellbore Measurements and Fracture Diagnostics for Hydraulic Fracture Optimization

Committee:

Mukul M. Sharma, Supervisor

Jon E. Olson

Nicolas Espinoza

John T. Foster

Nico P. Roussel

Wellbore Measurements and Fracture Diagnostics for Hydraulic Fracture Optimization

by

Brendan Michael Elliott

Dissertation

Presented to the Faculty of the Graduate School of

The University of Texas at Austin

in Partial Fulfillment

of the Requirements

for the Degree of

Doctor of Philosophy

The University of Texas at Austin

May 2024

Dedication

The entirety of this work is dedicated to my beautiful wife, who has uprooted her life to join me in this quest in Austin. I couldn't have done this without her love, support and editing skills.

I also would like to thank all the friends at UT who have helped me along the way and provided fruitful comments and brainstorming sessions. I have never been in a room of smarter, more intelligent individuals than the research lab.

And finally, Dr. Sharma who has provided the guidance, and insight to chase down and run with ideas. His unique leadership style allows for truly exceptional concepts to germinate and flourish.

Acknowledgements

I would like to acknowledge the vast body of work the industry has shared and published on the topic of well interference. We are truly standing on the shoulders of giants.

I would especially like to acknowledge the contributions of Dr. Ripu Manchanda, who has guided me through this workflow and provided exceptional insights and friendship.

Abstract

Wellbore Measurements and Fracture Diagnostics for Hydraulic Fracture Optimization

Brendan Michael Elliott, PhD

The University of Texas at Austin, 2024

Supervisor: Mukul Sharma

This dissertation presents new methods for analyzing wellbore pressure and strain measurements to better diagnose and optimize hydraulic fracturing treatments. Pressure interference data between fractured wells in unconventional formations during fracturing can be used to estimate key unknown fracture parameters. Currently, only fracture to fracture or fracture to gauge fluid pressure measurements have been investigated, while little to no research has been done to understand the expected deformation/strain in the offset well due to hydraulic fracturing.

To address this gap, laboratory experiments were conducted to clearly show the expected ranges of deformation under applied loading, while numerical modeling computed the total deformation and volume reduction of the casing during hydraulic fracture intersection. A new semi-analytical model to calculate poro-elastic pressure interference between fractured horizontal wells was developed, and a fully coupled fracture simulator was deployed to investigate the 3D strain field of a propagating fracture and its effects on a steel wellbore in the subsurface.

Multiple techniques to interpret wellbore pressure data and deformation were developed to resolve additional variables and reduce uncertainty. These methods included developing workflows for Volume to First Response of a fracture arrival, fracture growth

rate extrapolations, Monte-Carlo simulations, and wellbore azimuthal strain. Simulating fracture propagation from the treatment well and finely meshing the monitoring wellbore within the same mesh allows for computing the strain and pressure change within the monitor wellbore accurately. These measurements together with the wellbore pressure response can then be interpreted to obtain the timing of frac-hits, the fracture geometry, and the cluster efficiency.

Finally, a diagnostic dashboard was developed to integrate the learnings from this and earlier work on measurements and methods to generate realizations of fracture geometry from pressure signatures. This dashboard sets the groundwork for real-time diagnostics of fracture interactions and provides the industry a tool in which to make faster decisions on a once tedious and difficult process. The results can be used to make important reservoir management decisions such as well spacing and well placement while optimizing hydraulic fracture treatments.

Table of Contents

List of Figures

Chapter 1. Project Statement and Research Objectives

1.1 INTRODUCTION

As multi-well pad operations become more complex and the natural variability of the formations is better recognized there is a continual need to advance tools utilized for fracture characterization. Pressure interference between wells in low permeability systems is induced by poroelastic interactions (not by pressure diffusion) during fracturing. This has been well documented in recent literature and has been used to estimate fracture parameters such as azimuth, length, width, and height of the fracture (Kampfer et al. 2016, Roussel and Agrawal 2017) There has been extensive numerical modeling of this poroelastic phenomenon using fully coupled geomechanical simulators (Seth et al. 2018, Seth et al. 2019). These results have been compared to field observations and confirmed with diagnostics (Daneshy et al. 2012, Dawson et al. 2016, Spicer et al. 2019). However, numerical modeling of this process is time consuming and does not lend itself to a near real-time, or real-time explanation of offset pressure signals. It is almost always done after the fracturing treatment is complete as a matching exercise with field data. There are few methods that utilize a physical measurement at the wellbore, such as deformation, and ovality that translate directly to fracture diagnostics. The efforts in this work show new methods to acquire downhole wellbore measurements, and to couple these wellbore strains and deformations to become a useful fracture diagnostic tool for real time applications.

In the last decade, unconventional development has rapidly matured, and well developments have gone from a single well per section, to closely stacked, staggered full unit developments. New tools are needed to quickly diagnose, understand and react to field observations of pressure responses during fracturing. This work seeks to develop the foundation of real time interpretation utilizing novel wellbore measurements and provide the workflow for

real time interpretation, and validation of such measurements through laboratory studies, analytical expressions and fully 3D numerical modeling.

1.2 Analytical Model Extension & Simulations

In Chapter 3 we expand upon previous work for an analytical stress shadow, to include fracture to fracture stress shadow as well as for fracture - wellbore interactions. The predicted stress that acts on a wellbore can be considered as an extracted line in the stress field, and thus the magnitude of deformation in the reservoir and casing can be estimated. The main goal is to combine and improve upon existing analytical models for fracture stress and wellbore deformation as a fracture diagnostic. Purely elastic analytical methods are applied to low permeability formations and unconventional reservoirs during the timescale of a typical stimulation, and an inversion solution for fracture geometry is presented.

1.3 Wellbore Strain and Diagnostics

Chapter 4 focuses on developing fully coupled wellbore and fracture models to understand expected strain responses in the formation and on the wellbore. Wellbore diagnostics consider any measurements that can be made using a drilled and cased wellbore, including wellbore deformation, sealed well pressure monitoring, and azimuthal strain to resolve a greater understanding for fracture geometry. Varying response types, and magnitudes have been observed in unconventional plays, so a regional understanding of varying fracture characteristics is necessary.

Physical measurement of strain on actual oilfield tubulars in a laboratory setting enhances the understanding of the wellbore deformation problem. By utilizing highly accurate load cells and strain gauges to characterize the expected strain from various loading scenarios greater

interpretability of downhole strain responses is obtained. Generating the empirical data to predict strain at various distances from the loading is critical to an inverse model. Azimuthal measurements are key to calibrate any downhole tools or inversion methods for fracture geometry.

1.5 DERIVATIVES FOR WELLBORE MEASUREMENTS

Chapter 5 extends wellbore measurements to extract additional insights for the fracture geometry, growth rates, etc. Utilizing a volume to first response, (VFR) and various combinations of statistical fracture geometry, growth rates, and Monte-Carlo simulations we can derive estimates for the remaining propagating fractures, and the final expected fracture geometry that can be implemented in a near real time environment. An assessment for wellbore azimuthal strain is also explored as a novel diagnostic method.

1.6 FIELD IMPLEMENTATION OF DASHBOARD

Chapter 6, leverages the learnings above and utilizes the measurements and calculations for fracture geometry to develop an interpretation dashboard which can be deployed for advanced field diagnostics. Data is interpreted by the platform which presents results in a near-real-time manner, streaming pressure, strain, or parent child interactions to diagnose fracture geometry and visualize the inverted results to advise on the completion.

Chapter 2. Existing Literature and Significant Prior Research

This Chapter reviews recent literature on fracture driven communication, wellbore strain, and real time modeling and optimization methods. The background research will review current work and is not meant to be an exhaustive list, but rather, a concise description of contemporary industry understanding, methods deployed to date, and current technical capability.

To make an effective case for utilizing a wellbore as a monitor and to devote time to researching techniques to leverage wellbores as measurement tools, we must first present the case that fractures do indeed extend and intersect offset wellbores. A conceptual model is introduced (Figure 1) to set the framework of the issue at hand. Barree et al. (2017) presents an illustration of modern unconventional developments. The initial completion indicates a large hydraulic fracture geometry from the primary well, with fractures lengths overlapping infill well positions. This image presents a simple yet extremely common scenario for hydraulic fracturing in unconventional reservoirs. The notion that fracture growth is in excess of current well spacing sets the stage for the utility of wellbore measurements as a key fracture diagnostic.

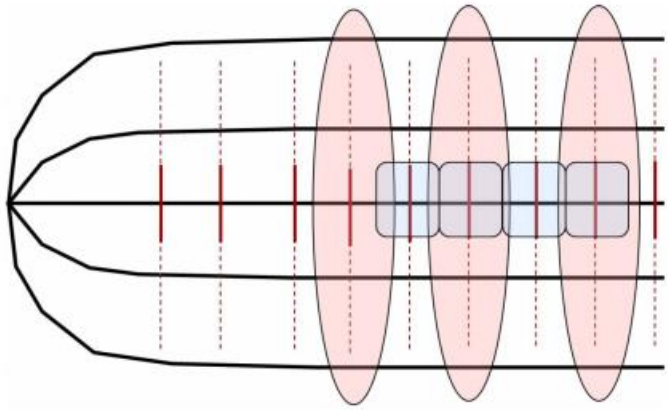

Drainage pattern established by pattern drilling of horizontal wells. The black lines represent the horizontal well sections, the red dashed lines the hydraulic half-lengths present while pumping a treatment (and can lead to "bashing"), and the solid red lines represent the effective production length.

Figure 1: Conceptual model for horizontal well development

2.1 CURRENT WELLBORE MONITORING AND DIAGNOSTIC TECHNIQUES

One of the most common fracture monitoring techniques is fracture shadow or offset pressure monitoring. Daneshy (2012) reviewed many topics on intra-well and inter-well communication and presents a qualitative analysis of field pressure data, through which he was able to infer some general characteristics of the fracture such as, fracture orientation, approximate fracture height, inter-well communication fluid exchange, and post-frac production communication. Daneshy (2012) cites this project as the first discussion of "fracture shadowing" in the literature. Later, in a 2014 paper, Daneshy gives the background, theory, and applications for this fracture shadow concept. Citing the original 2-D Sneddon solution from 1946, Daneshy describes the model interpretation for stresses induced by an active extending fracture (Figure 2). While the stresses associated with propagating fractures were well understood before this work, there were very few careful and deliberate measurements of pressures in offset wells.

The fracture driven interactions described by Daneshy were used by others to develop various methods of interpretation described below. These surface pressure responses are now widely recognized to be poroelastic responses caused by the actively propagating fracture and have since been measured on thousands of stages pumped by many operators. It should be noted that these responses are very different from "frac hits," which are characterized as direct fluid communication with the observation wellbore with large pressure spikes of greater than hundreds of pounds per square inch. A shadow response or elastic response can be much smaller (tens of psi) and can occur over a longer duration of time (five to ten minutes).

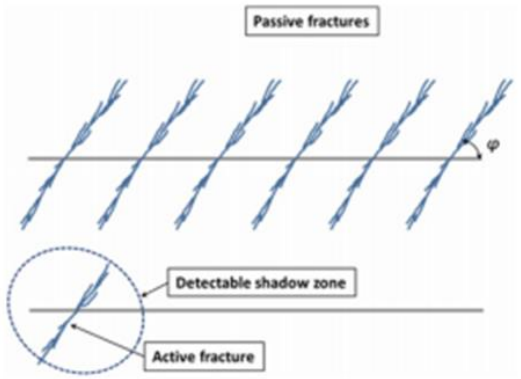

Figure 8—Schematic of fracture shadowing in offset wells

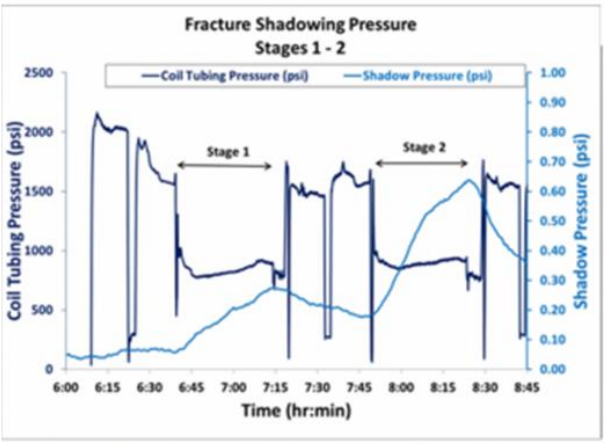

Figure 9—Fracture shadowing in offset wells (case history)

Figure 2: Fracture Shadowing Schematic and pressure Response from Daneshy SPE 170611,

Lehmann et al. (2016) presented a paper on the dynamic analysis of frac hits and inter-well connectivity in the Horn River Basin. They very elegantly describe the response characteristics of the pressure hits into four main components. First is the time delay, or difference observed between the start time of an offsetting hydraulic fracture stimulation and the observation of a pressure response; the value is interpreted as the distance covered by the fracture or as proof for the existence of connections between wells. The intensity, or rate of pressure increase observed in the passive wellbore, is the second component and presents information on conductivity or connection between wellbores. Thirdly, the magnitude, or peak pressure observed in the passive well, captures the active stimulation pressure and yields a degree of connectivity. The final components: falloff, or the rate of unsupported pressure decline observed after cessation of an active stimulation, gives insight into network complexity and system leakoff.

Roussel & Agrawal (2017) provide a quantitative model for poro-elastic responses and quantify fracture geometry from offset pressure monitoring. Their method uses the poro-elastic pressure responses on offset treatment wells and provides a quantitative framework for the interpretation of fracture signals. The paper includes support from modeling and numerical

simulations (Figure 3), which show the elastic response of the offset fracture growth. This paper also discusses critical differences between direct frac hits and poro-elastic responses.

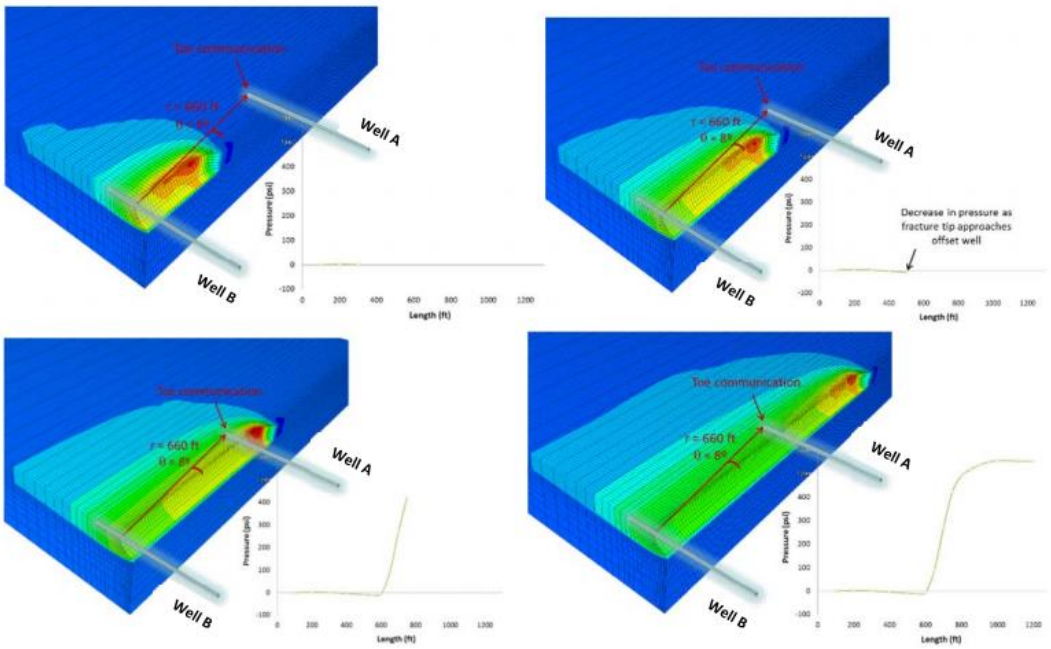

Figure 3: Evolution of poro-elastic response measured in offset well A during propagation of stage 1 in well B From SPE 2645414

An increasingly common technique is to deploy downhole fiberoptic cables to measure and monitor the stimulation exiting and approaching the wellbore. Gustavo et al. (2019) presents an interpretation of Distributed Acoustic Sensing - Strain Front (DAS-SF) as a diagnostic method to assess the far field efficiencies of stimulations in unconventional reservoirs. In this paper Ugueto details the process of cross well strain fiberoptic measurements. Hydraulic fractures are observed to be mostly planar, with some shear fracture in blue. The DAS_SF response show the strain pattern as the hydraulic fracture approaches and intersects the wellbore at varying times. These strain patterns along the fiber can be used to interpret fracture arrival, cluster efficiency, frac azimuth and geometry.

Fiberoptic sensing is highly sensitive to the fracturing propagation and has been observed to measure the tension (extensional) behavior ahead of the fracture before the propagating fracture intersects the monitor well. As can be seen in Figure 4, this strain front is from point (1) to point (a) where the actual fracture arrival is picked. At point (a), note the compressive region on either side of the fracture, which is interpreted as the fracture stress shadow. During the intersection of the well, there is a strong extension (red) signature in the fracture domain, with the coupled compression (blue) on either side of the fracture. As additional fractures arrive, this signature is repeated, and as the pumps shut down at point (2), all of the initiated fractures begin to relax and revert to a compressive state. This technology is perhaps the most relevant and immediately usable for wellbore strain research and measurements. Since the fiber cable is not directly coupled or imbedded in the casing, this strain is only a relative strain, and has no magnitude assigned. This is a major limitation, such that one cannot compute any real deformation from these fiber strain observations. A direct measure of strain is needed.

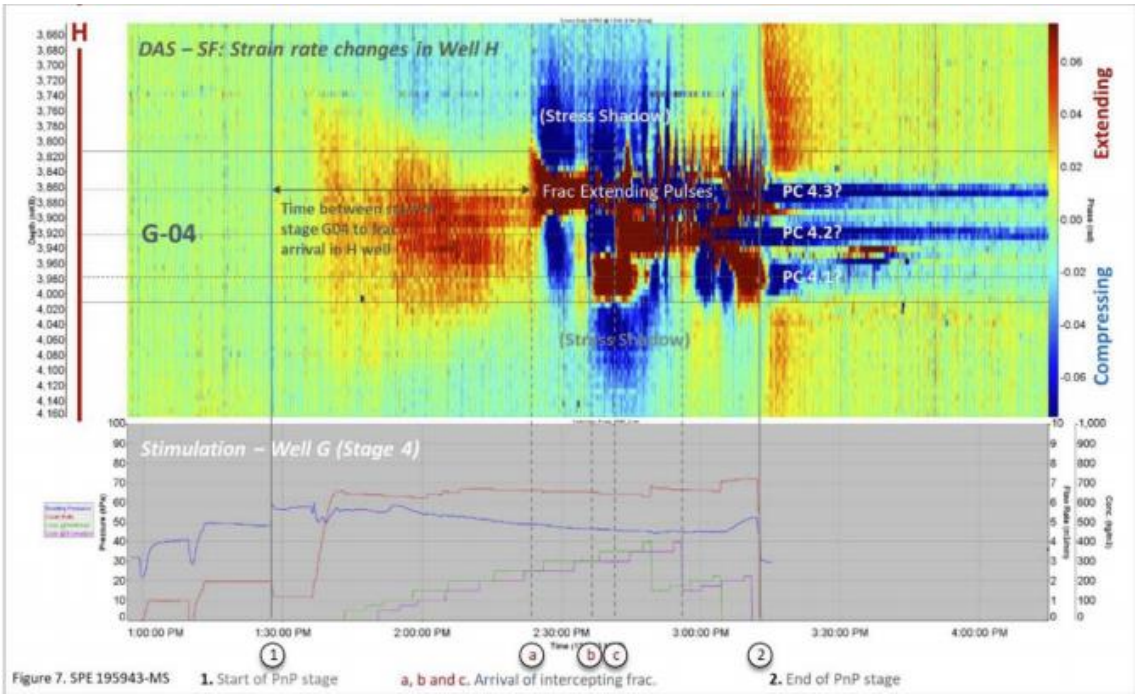

Figure 4: Annotated FO display of Cross Well DAS Strain front from a nearby well with 4 perforation clusters.

2.2 DOWNHOLE STRAIN TOOLS AND METHODS

There is an extensive collection of literature in the field of seismology and geophysics for long duration wellbore strain measurements using borehole strain meters. The borehole strain meters are typically deployed in shallow (100m-250m) vertical wellbores and measure change in borehole diameter along three azimuths at 120 degree phasing perpendicular to the borehole. The strain meters are highly sensitive, on the order of four picometers, and are typically used to measure strains induced by earth tides and the effect of the sun and moon on the earth's crust, which typically responds in tens of nanostrains. Gladwin et al (1985,1987) reviews design parameters for borehole strain instrumentation and applications of borehole tensor strain measurements in California. This technique has also been used to track plate movement and earthquakes that are much larger magnitudes. Figure 5 shows a schematic of the downhole strain gauge installation in a shallow borehole on the left and two images of the strain tool on the right.

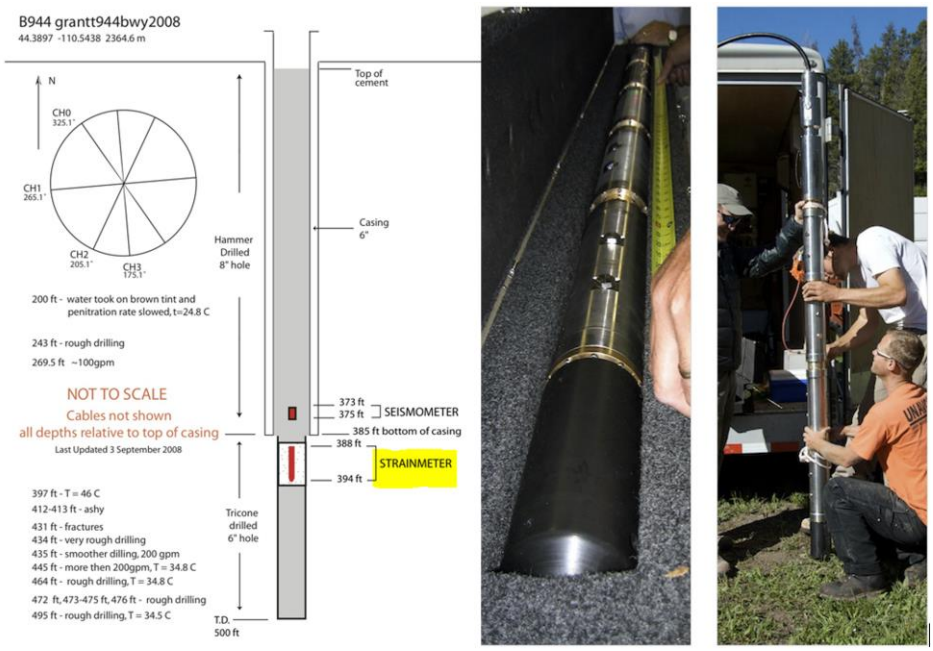

Figure 5: Schematic of a Borehole Strainmeter and Close up images of Strain tool.

Data from these studies has been made public through the Geodetic Facility for the Advancement of Geosciences (GAGE) project operated by UNAVCO and funded by NSA and NASA. The project includes an array of shallow measurement boreholes, which measure a wide variety of occurrences including plate boundary movements, episodic tremor and fault slip events, aseismic and co-seismic events, tidal and volcanic activity, and earthquakes. There is no evidence in the literature that this tool and process has been used to measure deformations induced by a hydraulic fracture, nor any mention of being deployed in any deep or horizontal wellbore.

A secondary method of measuring strain in the subsurface is known as the overcoring method, where *in-situ* stresses are measured based on the relief around the borehole. The relief of external forces causes changes in the borehole diameter and resulting strain on the borehole wall. If the elastic properties of the rock in the subsurface are known, the changes in the borehole diameter can be converted to the *in-situ* stresses in the rock. Hooker et al. (1974) describes the overcoring equipment used in rock stress determination.

A third method, again common in underground mining is the Compact Conical ended Borehole Overcoring (CCBO). Waclawik et al. (2016) presented this modified overcoring method that omits the overcoring or stress relief phase, as the probe is glued directly on the conically shaped end of the borehole. This probe is then allowed to make continual strain changes azimuthally in the borehole. Figure 6 displays The CCBO Cone with associated strain gauge geometry on the left, with radial strain gauge data measured radially by the probe (figure on the right).

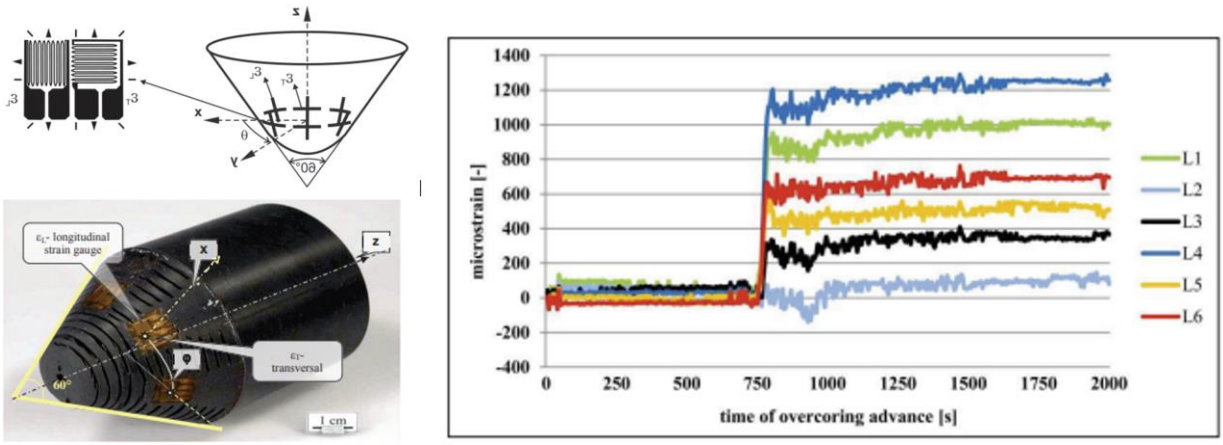

Figure 6: CCBO Probe geometry (left), and example Radial strain data recorded in time (right)

Since both of the previous methods of overcoring, are applied primarily in underground mining, and direct access to the formation with delicate equipment and coring tools is required, it is unlikely these methods could ever be deployed in a oil/gas development environment, but they establish the case for the utility of measuring deformation and strain in the subsurface setting.

Researchers from Lawrence Berkely National Lab developed a downhole tool to measure 3D borehole displacements induced by fluid injection into faults Guglielmi et al. (2020). They show how adding the 3D borehole displacement measurement tool while conducting hydraulic injection tests better constrains the principal stress orientations and magnitudes. They utilize a step rate injection method for fracture in-situ properties (SIMFIP). For this experiment the downhole tool was installed in the well being fractured, and when fault slip occurred, measurements were taken and recorded, then numerically modeled.

Kacper et al. (2020) introduce a high resolution acoustic based imaging method currently deployed to measure perforation entry hole diameters and perforation errosion, along with lost items in the well. It utilizes sound waves that reflect off the internal surface of the casing back to the tool, where the signal is recorded. From this signal, a distance can be measured azimuthally, and any ovality present can be precisely measured. Kacper also reports the presence of ovality

correlates with plug failures. This tangible measurement of ovality and azimuthial differenes in casing shape after hydraulic fracturing yield further evidence of the need to understand azimuthal variations in deformation and support of the utility of wellbore strain measurements.

2.3 REAL TIME OPTIMIZATION INDUSTRY EXAMPLES

The concept of "real time" fracturing, simulation and optimization has been around for many decades in the oil and gas industry. In fact, even before most computers were very powerful many individuals were developing real time simulation and optimization workflows. Clearly et al. (1988), and Meyer et al. (1990) were clearly some early innovative thinkers, each with papers on "Enhancing Real Time Hydraulic Fracturing Models" and "Real Time 3D Fracturing Simulations" in 1988 and 1990 respectively. For many, the business case and opportunity to optimize is well understood, but the industry has been challenged in mass adaptation of any specific example in literature or offering from major service companies.

Diagnostics have been key in the past to any real time optimization case, as can be seen by Wright et al. (2001), where tilt meters were deployed to measure fracture deformation in real time and to observe changes in height and width of the fracture. They show a field example of a well stimulated at varying rates and observe the dynamic change on the fracture tilt from by changing rate from 20 to 50 bbl/min.

More recently, many others have deployed more advanced methods to develop a better understand of stimulations in real time. Paryani et al. (2018) discuss a method of real time completion optimization using commonly available surface data from drilling and fracturing. The workflow captures stress and properties along the wellbore to help design the completion and subsequently surface treating pressures are used to model and match fracture geometry. The novel

part of this work is real-time frac modeling. When there is a significant difference in the predicted treatment profile, the actual model parameters are adjusted to match the stimulation response (leakoff, perf friction, wellbore friction). This work was limited in the sense that no real time decisions or optimization efforts were made during the stimulation.

Occidental (Shen et al. 2020) presents a deep-learning based fracture event recognition for stage wise analysis, enabling automated stage start times, ball pumpdown/seat signatures, and segmentation of the job. While this work is quite novel utilizing advanced computing, it is more for quality assurance and event identification, rather than optimizing the fracturing operations in real time.

One of the better studies that truly focuses on real time optimization utilizes poroelastic stress shadow monitoring to inform decisions is by Ji et al. (2020). Methods for analyzing surface pressure data in real time are used to improve the completion design and cluster efficiency of child wells while protecting the nearby parent wells.

One of the major stimulation service providers has been working on the real time concept for many years now. Ming et al. (2017) reports a case for near real time return on fracturing investment optimization, which leverages log data, fracture modeling and neural networks. This method looks at how fractured well productivity is affected by different fracturing treatment parameters. The neural net is trained and validated to provide near real time solutions for fracture characterization. Other examples of major service providers offering intelligent fracturing systems, with dashboards that gives operators real time fracturing control while pumping by integrating subsurface fracture measurements, live 3D visualization and real time fracture commands. A visualization of the interface can be seen in Figure 7,where downhole fiberoptic sensing data is integrated to both a treatment plot and a 3D view of the wells.

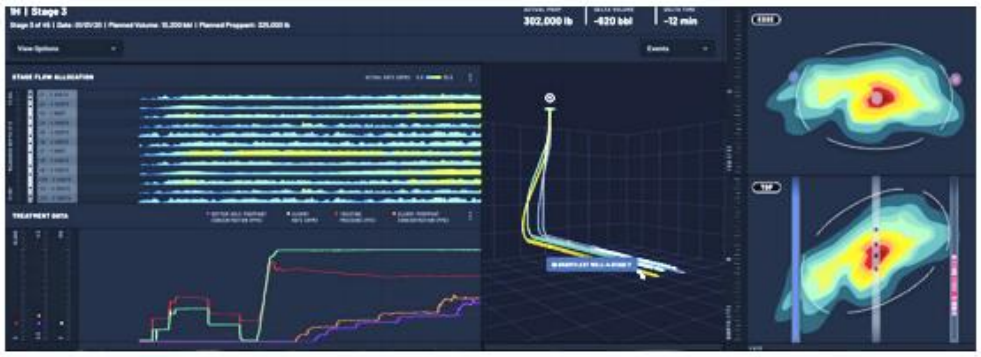

Figure 7: Example view from large service provider service offering Smart Fleet

2.4 SEALED WELLBORE PRESSURE MONITORING

Sealed wellbore pressure monitoring (SWPM) is a technique used to evaluate and quantify fracture growth rates using wellbore deformation and surface pressure changes Haustveit & Elliott et al. (2020). The authors cite the link between fracture arrivals on a wellbore observed with DAS fiberoptic cross well strain events with the subsequent pressure inflections on the monitor well indicating the fracture intersection and arrival at the location of the sealed monitor wellbore.

Brinkley et al (2021) monitored fracture propagation in the Eagleford shale. Mckimmy et al. (2022) used it to understand fracture morphology in the Bakken. Cipolla et al. (2023) utilized SWPM in conjunction with permanent fiber-optics to evaluate stimulation effectiveness in the Bakken. Ballanger et al. (2022) coupled SWPM and the Chow Pressure Group to quantify hydraulic and conductive fracture geometries, Chin et al. (2022) deployed the technology in the Montney in Canada.

Using a different but related approach, Elliott et al. (2022) deployed laboratory measurements and novel fracture modeling to measure and calculate the deformation of the casing as the load on the casing is altered along the wellbore. The ovality of the borehole (which can be measured downhole) was used as an indication of the level of pressure depletion. The deformation

is directly related to the SWPM response magnitudes. The wellbore strain induced on the casing can be used to compute the changes in fluid pressure measured in the SWPM method. Zheng et al. (2021) expanded on this work to leverage azimuthal measurements and showed how the ovality of the wellbore can be interpreted as fractures intersect a wellbore or as depletion reduces the stress around the casing over time.

Finally, Iriarte et al (2021) developed a scalable process for SWPM with standardized input workflows, and visuals, while Ramirez et al 2022, developed an automation workflow to recognize the SWPM signatures. Olson et al. (2023), utilized the SWPM technology in to develop workflows for calibrated fracture modeling.

2.5 DISCUSSION OF PRESENT STATUS AND UNRESOLVED ISSUES

As can be seen from the literature review, many operators either have experienced or are currently experiencing issues with fracture driven interaction, and it is becoming a more common occurrence as fields mature. There is a general industry consensus that the main drivers of fracture interference between wells is lower well spacing, typically large completion job volumes, as well as the tendency to have asymmetric and unequal distribution between the treatment clusters. The industry has developed technology to distinguish between direct frac hits and poroelastic responses, using a wide variety of fracture measurements.

Current technologies such as fiberoptic monitoring and SWPM, have proven to be effective but do not allow for an exact measure of strain that can be coupled to deformation of the wellbore.

Other industries have explored downhole strain measurement techniques like borehole strainmeters in shallow wells to measure earthquakes or overcoring to determine stresses and strains in underground mining. Neither have proven capable of determining strains in modern oilfield horizontal wells and have severe limitations in application. Neither technique has been

deployed specifically to monitor fracture growth, and there is an existing technology gap to measure strain in wellbores.

Real time monitoring has been discussed for over 30 years. As computing power has increased, some of these ideas can be brought to fruition. Still, no technique has proven to be the established method and there is no systematic deployment of this in the industry today. Rarely are these real time methods targeting on-the-fly treatment design changes, and even more sparse is a solid technical framework to make firm recommendations for what type of alterations to the fracture treatment should be pursued at any given time in the job. This dissertation aims to address some of these issues.

Chapter 3. Extension of an Analytical Model for Estimating

3.1 Stresses Induced by Propagating Fractures [1]

Using offset well pressure measurements to diagnose the geometry of propagating fractures is now popular in unconventional tight oil environments (Kampfer and Dawson, 2016; Roussel and Agrawal, 2017; Seth et al. 2019c). The fundamental mechanism for the observation of these pressure measurements lies in the stress shadow induced by a fracture (Manchanda 2015 ; Roussell 2017). The opening of a fracture in the subsurface can induce higher compressive stress in its vicinity. This compressive stress can effectively squeeze rock or another open fracture and increase the pore pressure in the region (Daneshy, 2014; Manchanda et al. 2018). Many authors have shown evidence of this through measurements made using cemented pressure gauges outside the casing (Elliott et al. 2019), observing surface pressure after toe-prep operations (Roussel and Agrawal, 2017), and monitoring surface pressure changes with bridge-plugs isolating fracture stages (Kahn et al. 2018; Seth et al. 2019a, 2019b; Spicer and Coenen, 2018). In previous work, an analytical 3-D model was developed to estimate the pressure changes in the cemented pressure gauges outside the casing (Elliott et al. 2019; Manchanda et al. 2019a). An inversion algorithm was developed to obtain accurate estimates of the fracture geometry of a propagating fracture. Cemented pressure gauges outside the casing can be a powerful diagnostic technique to observe these pressure changes and capture unique insight into the geometry of the propagating fractures. However, installing downhole pressure gauges in horizontal wells is expensive and can create an

[1] 1 This chapter is adapted from paper SPE-199720-MS (Manchanda, Ripudaman , Elliott, Brendan , Seth, Puneet , and Mukul Sharma. "Multi-Well Poroelastic Pressure Interference Analysis: Towards Real-Time Fracture Diagnostics." Paper presented at the SPE Hydraulic Fracturing Technology Conference and Exhibition, The Woodlands, Texas, USA, February 2020 *Manchanda and Elliott Contributed equally to this work and is an extension of previous work from Elliott's Masters thesis and previous collaborations. Manchanda and Elliott collaborated to derive the multi-well solution and Elliott deployed it to actual field cases presented here.

operational challenge. In practical industry applications, monitoring pressure through a toe-prep or an isolated stage is more convenient and cost effective and thus done more regularly. So far, the analysis of the pressure changes in a monitoring well with fractures caused by fractures in nearby wells has only been possible through computationally expensive geomechanical numerical simulations (Seth et al. 2019c, 2018).

This chapter describes the development of a new semi-analytical model that is an extension of a previously developed analytical model (Manchanda et al. 2019b). This new semi-analytical model has been developed to calculate the pressure changes in one or more monitor wells that are connected to the reservoir through one or more fractures because of the opening and propagation of one or more fractures in a treatment well. The semi-analytical model is validated with a fully-coupled numerical model. The impact of various operational and reservoir parameters on the model predictions are presented. The model is applied to a field scenario comprised of several treatment stages and two monitor wells. An inversion analysis using the model provides estimates of the fracture geometries in the treatment and monitor wells.

Model Development:

As mentioned above, this model is an extension of the model discussed in previous work (Elliott et al. 2019; Manchanda et al. 2019a). The model discussed in this work has been developed with computational efficiency as a priority while maintaining reasonable accuracy. This allows for faster inversion model development and extension of the model to real-time analysis, interpretation, and actionable recommendations. This can be crucial for sensitive real-time scenarios such as parent-child interactions and inter-well fracture interference (Bommer et al. 2017; Bommer and Bayne, 2018).

3.2 Analytical Stress Shadow Induced by Multiple Fractures

Stress Shadow of a Finite-Height Fracture

Nordgren (1972) has shown that the width profile of a constant height fracture along the length of the fracture can be estimated using Eq. (1).

$$\phi\left(\frac{x}{X_f}\right) = \frac{w(x)}{w_{max}} = \left[\frac{x}{X_f}\sin^{-1}\frac{x}{X_f} + \left(1 - \left(\frac{x}{X_f}\right)^2\right)^{\frac{1}{2}} - \frac{\pi}{2}\frac{x}{X_f}\right]^{\frac{1}{4}} \quad (1)$$

Additionally, the fracture width at the wellbore is given by Eq. (2).

$$w_{max} = \frac{2P_{net}h(1-\nu^2)}{E} \quad (2)$$

For scenarios in which the fracture length is much larger than the fracture height, we can assume the fracture geometry to be a sequence of several 2-D fractures arranged alongside each other from the wellbore to the fracture tip as illustrated in Figure 8. This is similar to the representation of a PKN fracture as discussed in Nordgren (1972). Analogously, the calculation of the stress shadow induced by the PKN fracture can be done as shown in Elliott et al. 2019 and Manchanda et al. 2019. It can be noted that these equations are using the assumption of plane strain elements that are discretized along the length of the fracture.

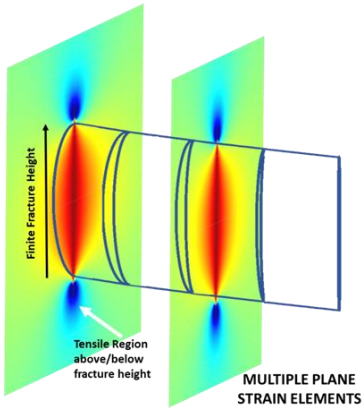

Figure 8: Representation of a finite height fracture using plane strain elements in the length direction.

For a line crack that is opened by a constant net pressure inside the fracture, the stress shadow of that fracture is defined by the following equations:

$$\Delta\sigma_{xx} + \Delta\sigma_{yy} = -2P_{net}\left[\frac{r}{\sqrt{r_1 r_2}}cos\left(\theta - \frac{\theta_1 + \theta_2}{2}\right) - 1\right] \quad (3)$$

$$\Delta\sigma_{yy} - \Delta\sigma_{xx} = -2P_{net}\left[\frac{rsin\theta}{X_f}\left(\frac{X_f^2}{r_1 r_2}\right)^{\frac{3}{2}}\sin\left(\frac{3}{2}(\theta_1 + \theta_2)\right)\right] \quad (4)$$

$$\Delta\sigma_{xy} = P_{net}\frac{rsin\theta}{X_f}\left(\frac{X_f^2}{r_1 r_2}\right)^{\frac{3}{2}}\cos\left(\frac{3}{2}(\theta_1 + \theta_2)\right) \quad (5)$$

Combining Eq. (3) and Eq. (4), we see that the stress shadow in the plane of a 2-D fracture can be expressed as:

$$\Delta\sigma_{yy} = -P_{net}\left[\frac{r}{\sqrt{r_1 r_2}}cos\left(\theta - \frac{\theta_1 + \theta_2}{2}\right) - 1 + \frac{rsin\theta}{X_f}\left(\frac{X_f^2}{r_1 r_2}\right)^{\frac{3}{2}}\sin\left(\frac{3}{2}(\theta_1 + \theta_2)\right)\right] \quad (6)$$

Now, realize that the w_{max} in Eq. (2) is the maximum width of each 2-D fracture cross-section along the length of the fracture with $X_f = h/2$. Thus, we can now transform Eq. (6) to get Eq. (7) where $r', r_1', r_2', \theta', \theta_1', \theta_2'$ are transformed appropriately into the new coordinate system. This is visualized in Figure 9 and Figure 10.

$$\Delta\sigma_{yy} = -P_{net}\left[\frac{r'}{\sqrt{r_1' r_2'}}cos\left(\theta' - \frac{\theta_1' + \theta_2'}{2}\right) - 1 + \frac{2r'sin\theta'}{h}\left(\frac{h^2}{4r_1' r_2'}\right)^{\frac{3}{2}}\sin\left(\frac{3}{2}(\theta_1' + \theta_2')\right)\right] \quad (7)$$

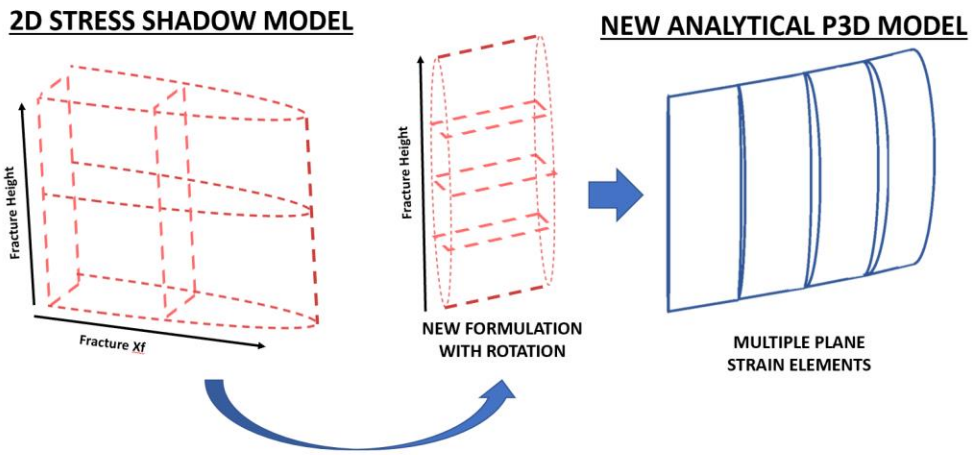

Figure 9: Transformation of a 2-D fracture to plane strain elements in a 3-D fracture.

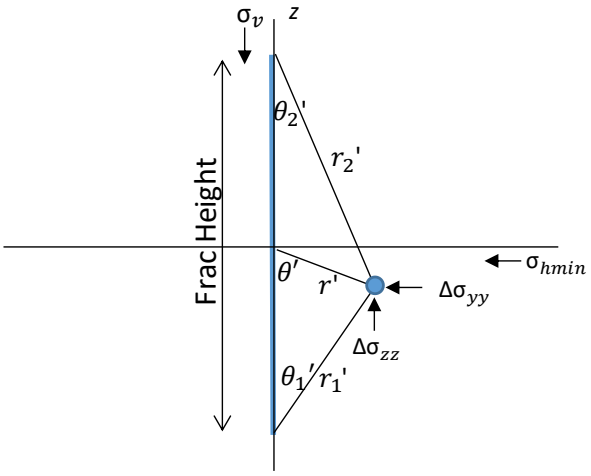

Figure 10: Cross-section view of a PKN type fracture with a representation of the transformed coordinate system.

A two-step approach is utilized to calculate the stress shadow induced by multiple fractures. In the first step, net pressure is calculated in each fracture for the same fluid pressure and under the stress shadow of the neighboring fractures. Then the effective net pressure and superposition are used to calculate the stress shadow induced by multiple fractures at a certain distance away from the fractures. Since superposition is being used the overarching assumption is a fracture shadow is the net response induced by the multiple fractures, and that the stress shadow can be thought of as a linear system perpendicular to the propagating fractures.

Consider the opening of three parallel 2-D line cracks at the same fluid pressure (P_{f0}) under a uniform confined stress (S_{y0}) as shown in Figure 11, where the coordinate perpendicular to the fracture face is represented by the y subscript. The net pressure of the three fractures can be described as shown in Eq. (8).

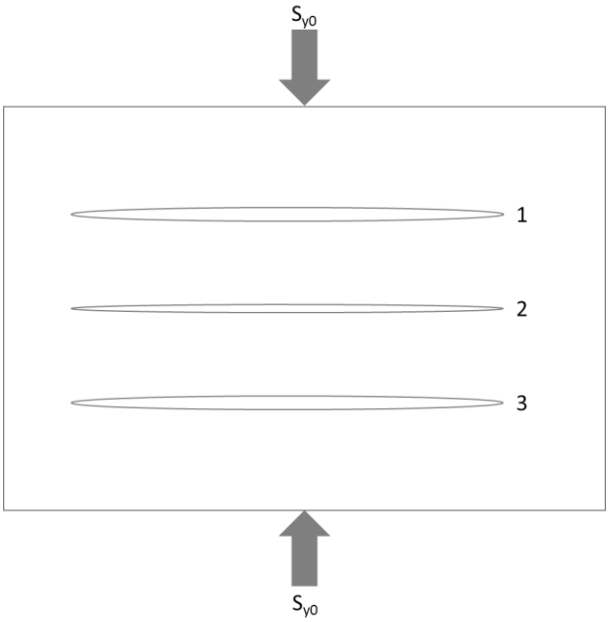

Figure 11: Illustration of three parallel line cracks open under constant fluid pressure

$$\begin{aligned} P_{net}^{1} &= P_{f0} - S_{y0} - \Delta S_y^2 - \Delta S_y^3 \\ P_{net}^{2} &= P_{f0} - S_{y0} - \Delta S_y^1 - \Delta S_y^3 \\ P_{net}^{3} &= P_{f0} - S_{y0} - \Delta S_y^1 - \Delta S_y^2 \end{aligned} \tag{8}$$

The ΔS_y^i terms represent the stress shadow induced by the i^{th} fracture. In general, the above equations can be expressed as:

$$P_{net}^{i} = P_{f0} - S_{y0} - \sum_{i \neq j} \Delta S_y^j \tag{9}$$

Though the ΔS_y^j terms are a function of spatial coordinates in reality, in this work we assume that an averaged value of the stress shadow of each fracture suffices the interaction between the fractures. Thus, we get,

$$P_{net}^i = P_{f0} - S_{y0} - \sum_{i \neq j} \overline{\Delta S_y^J} = P_{f0} - S_{y0} - \sum_{i \neq j} P_{net}^j \left(\overline{\Delta S_y^J} / P_{net}^j \right) \tag{10}$$

This creates a system of linear equations that can be solved together to estimate the net pressure in each fracture. Using the equations shown in the previous section and the net pressure calculated above we can determine the stress shadow induced by each fracture at a coordinate location anywhere in the 3-D domain. By using the concept of superposition, the total stress shadow induced by a cluster of fractures can be calculated to be:

$$\Delta S_y(x, y, z) = \sum_i \Delta S_y^i(x, y, z) \tag{11}$$

Pressure Change in Monitor Well

The pressure change in the monitor well caused by the compression of the fractures in the monitor well can be calculated using the compressibility equation.

$$dP = \frac{1}{C_t} \left(\frac{dV}{V} \right) \sim \Delta \mathrm{P_{MW}} = - \frac{K_{fluid}}{V_{MW} + \sum V_{fracs}^{MW}} \Delta V_{fracs}^{MW} \tag{12}$$

Where C_t is fluid compressibility and the inverse (K_{fluid}) is the bulk modulus of the fluid. The volume of the compressible system is the sum of the monitor well volume inside the casing, and the monitor well fracture volume. The change in volume of the monitor well fractures can be cumulatively calculated by the change in the volume of individual cross-sections along the length of the fractures. This can be done by evaluating the change in the net pressure along the length of

the monitoring well fractures because of the creation of the treatment well fractures. Assuming infinite conductivity of the fractures in the monitoring well,

$$\Delta \mathrm{P}_{\mathrm{net}}^{\mathrm{MW}} = \left(P_f^{MW} - S_y\right) - \left(P_f^{MW0} - S_y^0\right) = \Delta P_{MW} - \Delta S_y^{TW} \tag{13}$$

And this change in net pressure can be related to the change in fracture volume as

$$\Delta \mathrm{V}_{\mathrm{f}}^{\mathrm{MW}} = \frac{\pi}{2\mathrm{E}'} \sum_i h_i^2 \sum_{x_j} \Delta P_{net,i}^{MW} dx_j = \frac{\pi}{2\mathrm{E}'} \Delta P_f^{MW} \sum_i h_i^2 \sum_{x_j} dx_j - \frac{\pi}{2\mathrm{E}'} \sum_i h_i^2 \sum_{x_j} \Delta S_y^{TW} dx_j \tag{14}$$

Where x_j and h_i are the elements along the length of the fracture, and E' is the modulus of the formation. Substituting this equation in Eq. (12) and rearranging we get,

$$\Delta P_{MW} = \frac{\frac{K_{fluid}}{V_{MW} + \sum V_{fracs}^{MW}} \frac{\pi}{2\mathrm{E}'} \sum_i h_i^2 \sum_{x_j} \Delta S_y^{TW} dx_j}{1 + \frac{K_{fluid}}{V_{MW} + \sum V_{fracs}^{MW}} \frac{\pi}{2\mathrm{E}'} \sum_i h_i^2 \sum_{x_j} dx_j} \tag{15}$$

This equation can now be used to calculate the pressure change induced in the monitor well (a quantity that we can measure).

3.3 NUMERICAL VALIDATION

The stress shadow predicted by the semi-analytical model developed in this work is compared with a fully coupled poroelastic numerical geomechanical model developed in previous work (Seth et al. 2018, 2019b). The model schematic used for this comparison is shown in Figure 12. The parameters used to model the stress shadow are shown in Table 1. The results from the two models are compared along lines that are described in Table 2.

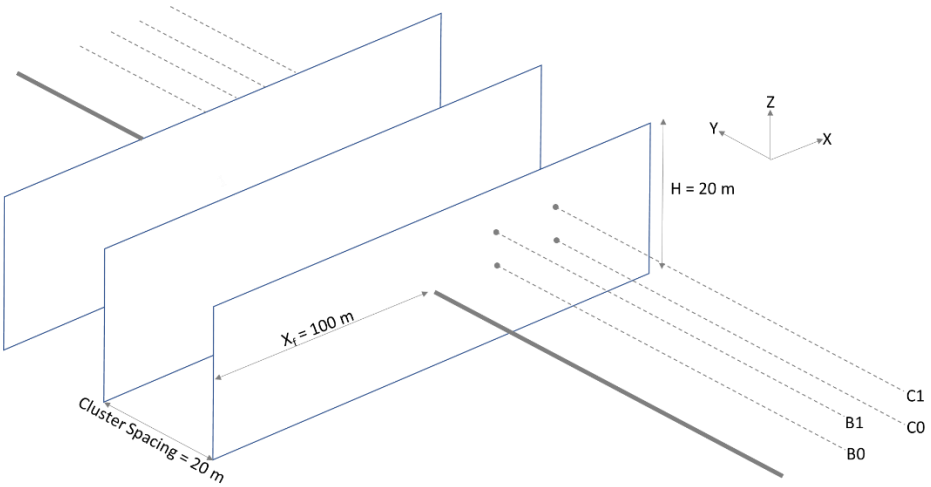

Figure 12: Model schematic used for numerical validation. Solid grey line shows the location of the well. Dashed lines depict the locations along which the comparison is made.

Table 1 – Parameters defined for numerical comparison

Cluster spacing (m)	20
Fracture half-length (m)	100
Fracture height (m)	20
Fracture pressure (MPa)	52
In situ Shmin (MPa)	50
In situ Shmax (MPa)	55
In situ Sv (MPa)	60
Young's Modulus (GPa)	20
Poisson's ratio	0.25

Table 2 –Lines along which the analytical model is compared with the numerical model. The fracture stage is centered at x = 0 and z = 0.

Lines	Z = 0m	Z = 5m	Z = 15m
X = 0m	A0	A1	A2
X = 25m	B0	B1	B2
X = 50m	C0	C1	C2
X = 75m	D0	D1	D2

A grid-block size of 0.625 m adjacent to the fractures was used to obtain the numerical model results. As can be seen in Figure 13, the semi-analytical model results match fairly well with the numerical model along different lines as described in Table 2. The stress-shadow is highest adjacent to the fractures and decays with distance away from the fractures. The stress

interference between the fractures is captured accurately by the semi-analytical model as shown in Figure 14.

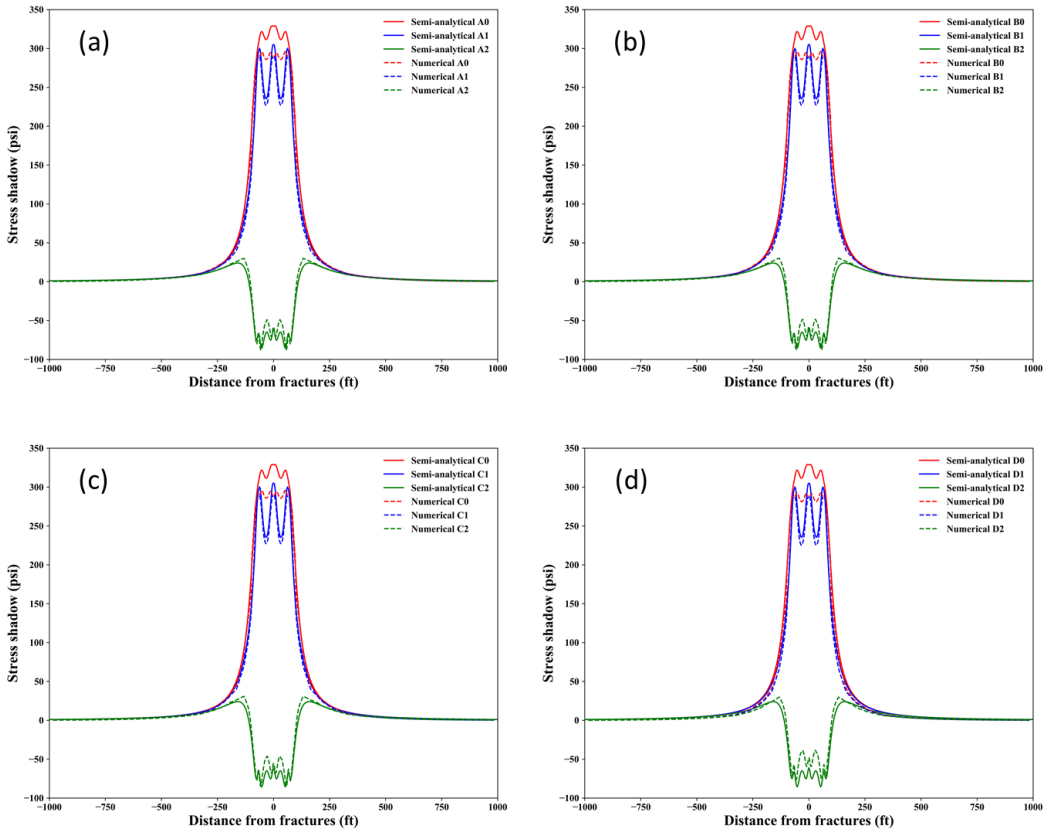

Figure 13: Comparison between semi-analytical model developed in this work and numerical model developed in previous work. The stress shadow of the simulated fractures is plotted along different lines perpendicular to the fractures.

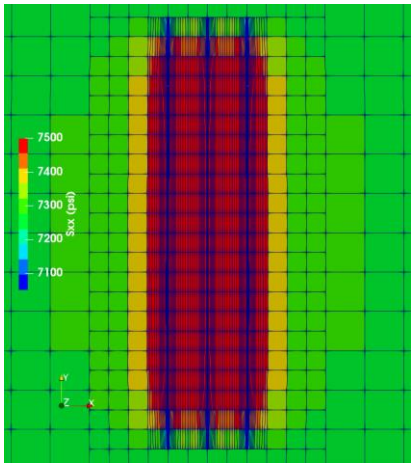

Figure 14: Map view of the numerical simulation results showing the stress perpendicular to the three open fractures. Note that in the numerical simulations, the fractures are parallel to the Y-direction.

Results and Discussion

In order to understand the various factors that govern the change in the monitor well pressure, a sensitivity analysis is presented. The Base Case schematic (Figure 15) includes two wells with three fractures in each well. One well is the monitoring well, and the other well is the treatment well. For the base case scenario described in

Table 3, a 70 psi simulated change is observed in the monitor well pressure. For simplicity, pressure drop down the fracture is ignored in both wells. The model can handle variable values of fracture lengths and heights for both the monitoring and treatment wells, but for simplicity, uniform fracture lengths and heights are also assumed in both wells.

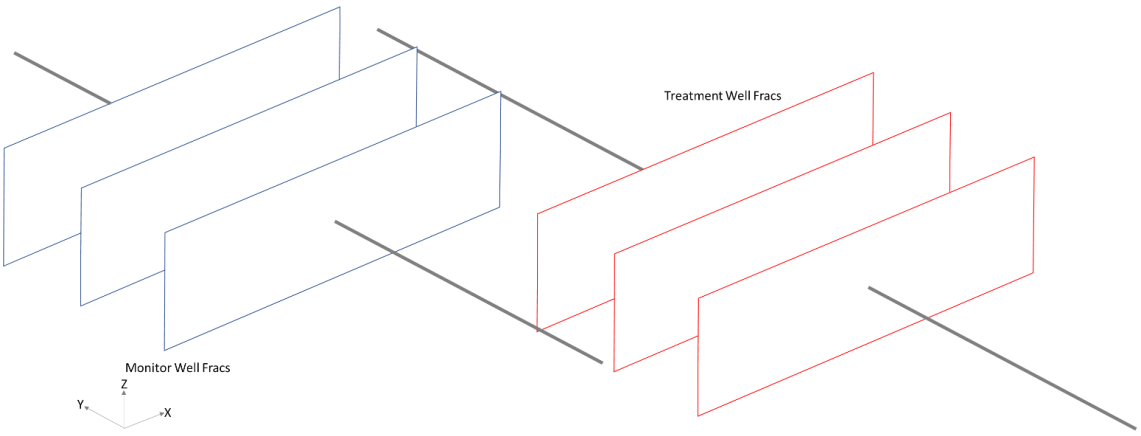

Figure 15: Schematic for sensitivity analysis

Table 3 – Parameters defined for base case

	Monitor Well	Treatment Well
Number of fractures	3	3
Cluster spacing (m)	10	10
Fracture half-length (m)	250	250
Fracture height (m)	50	50
Fracture pressure (MPa)	52	60
In situ Shmin (MPa)	50	50
In situ Shmax (MPa)	55	55
In situ Sv (MPa)	60	60
Young's Modulus (GPa)	20	20
Poisson's ratio	0.25	0.25
First cluster Y coordinate (m)	-100.0	100.0
Well X coordinate (m)	0.0	100.0

Impact of Fracture Half-length

Fracture half-length in both the monitoring well and the treatment well is varied while keeping all the other parameters constant. Figure 16 shows the changes in the monitor well pressure as a function of the monitor fracture half-length. For small monitor fracture half-length and large treatment fracture half-length, the pressure change in the monitor well is not observed because the overlap of the monitor well fractures and treatment well fractures does not change for the range of values considered. In previous work, using numerical simulations, the authors have shown that this overlap area governs the observed pressure response in the monitoring well (Seth et al. 2018). For longer monitor fracture half-lengths the overlap area decreases, and thus for the same treatment fracture half-length, the monitor well pressure change decreases. Similarly, increasing the treatment well fracture half-lengths increases the overlap area and causes an increase in the monitor well pressure change. The semi-analytical model presented here captures these trends very well.

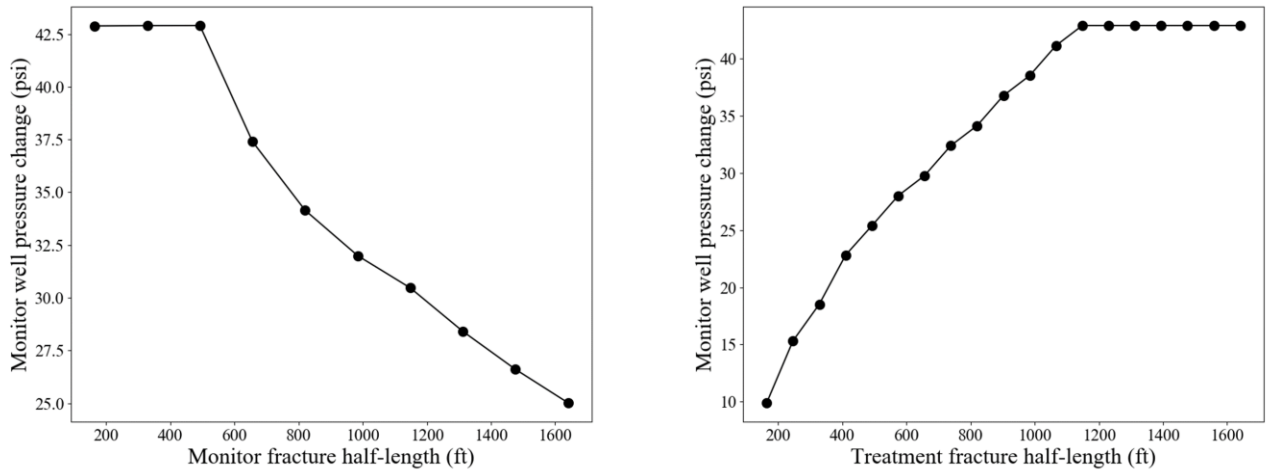

Figure 16: Impact of the monitor well fracture half-length and treatment well fracture half-length on monitor well pressure change.

Impact of Fracture Height

Fracture height in both the monitoring well and the treatment well while keeping all the other parameters constant. Figure 17 shows the changes in monitor well pressure for the considered scenarios. An increase in the monitor fracture height decreases the overlap area percentage between the treatment well fractures and the monitor well fractures. This causes an increase in the volume of the monitor well compressible system and thus decreases the amount of the pressure change observed in the monitor well. Increasing the treatment well fracture height increases the stress shadow on the monitor well fractures. This increased stress causes the monitor well fractures to be compressed more and hence induces a higher pressure change in the monitor well. Note that the monitor well pressure change is more sensitive to the height of the treatment well fractures than the height of the monitor well fractures.

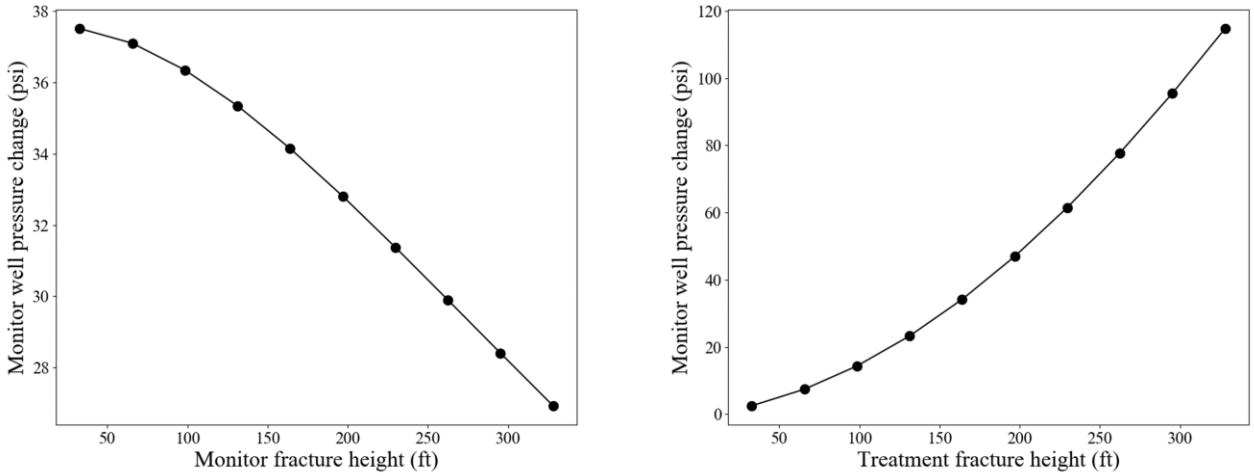

Figure 17: Impact of the monitor well fracture height and treatment well fracture height on monitor well pressure change.

Impact of Fracture Pressure

The treatment well fractures' final pressure is varied while keeping all the other parameters constant. The observed monitor well pressure change is shown in Figure 18. An increase in the

treatment pressure causes a proportionate increase in the stress shadow induced at the monitor well fractures' locations. This causes the monitor well pressure change to linearly increase with the increase in the treatment fracture pressure.

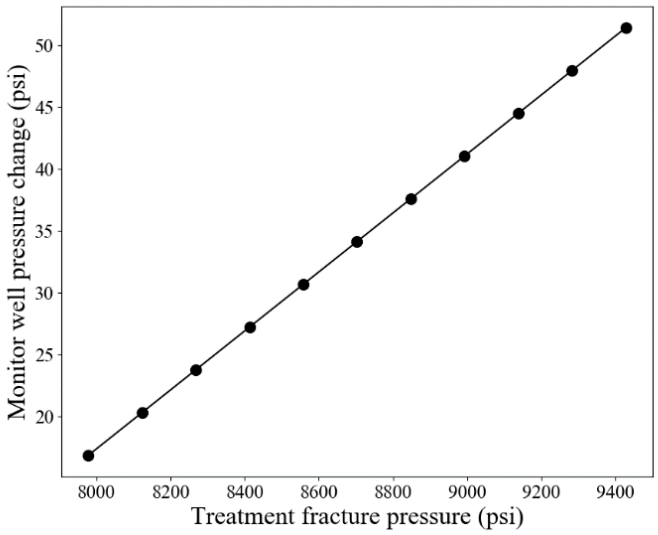

Figure 18: Impact of treatment well fracture pressure on monitor well pressure change

Impact of Number of Fractures

Next the impact of the number of monitor well fractures and the number of treatment well fractures is investigated while keeping all the other parameters constant. The monitor well pressure change for the different scenarios is shown in Figure 19. From the figure a non-monotonic impact of the number of monitor well fractures on the monitor well pressure change is evident. This suggests that a monitor well with a single fracture will observe a smaller pressure change than a monitor well with two to four fractures. However, it is important to note that beyond four open fractures in the monitor well, the observed pressure change sharply decreases. This is likely due to the competition between stress induced by adjacent fractures and the increase in monitor well fracture volume, which would cause the pressure change to decrease. At some point the more

fractures in the monitor well the increased volume begins to overtake the shadowing effect, here that breakover occurs at 4-5 monitor fractures. An increase in the number of treatment well fractures, on the other hand, shows a monotonic increase in the monitor well pressure with the number of treatment well fractures. This is because the developed model uses superposition and shows an increase in the stress shadow observed at the monitor well fractures with an increase in the number of treatment well fractures. This suggests the potential in using the developed model to determine completion effectiveness and identifying the number of propagating fractures in the treatment well and the number of fractures created in the monitoring well.

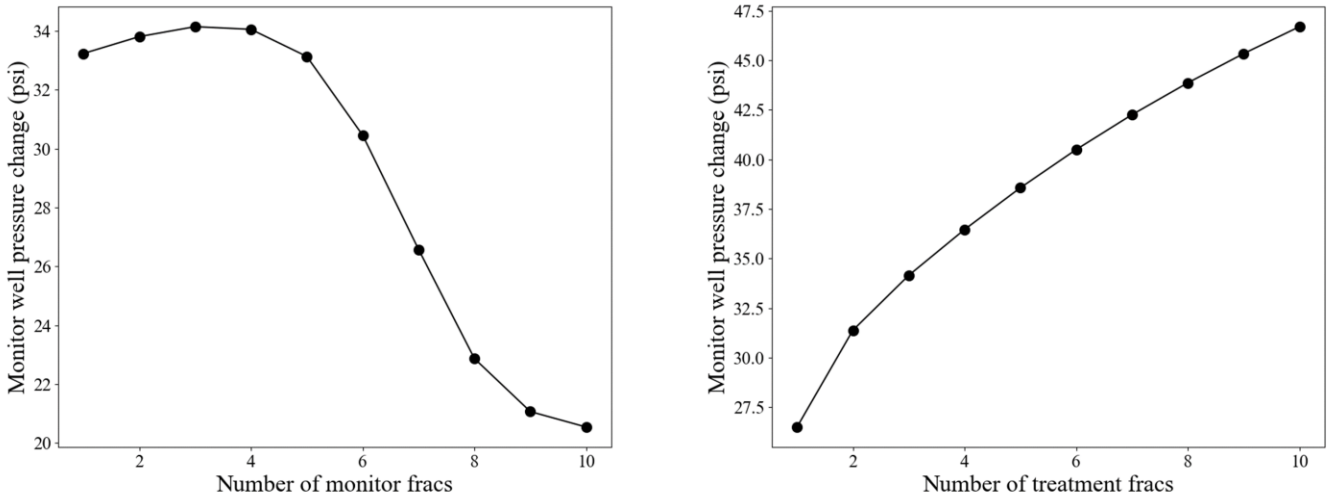

Figure 19: Impact on the number of monitor well fractures and the number of treatment well fractures on monitor well pressure change

Impact of Cluster Spacing

Changing the cluster spacing in the monitor well and the treatment well affects the monitor well pressure change as shown in Figure 20. Increasing the spacing between the monitor well fractures leads to an increase in the simulated monitor well pressure change. This is because increasing the cluster spacing in the monitor well decreases the stress interference between the

monitor well fractures. Additionally, and more importantly, increasing the cluster spacing in the monitor well moves the fracture nearest to the treatment well fractures even closer. This increases the stress interference on the monitor well fracture and hence increases the simulated monitor well pressure change. Analogously, a large monitor well pressure change is observed for larger cluster spacing in the treatment well. At small values of treatment well cluster spacing, the high-stress interference between the treatment well fractures can cause the middle fracture to have a small width and the outer fractures to induce a much larger stress shadow. This causes the monitor well pressure change to increase at very low values of treatment stage cluster spacing.

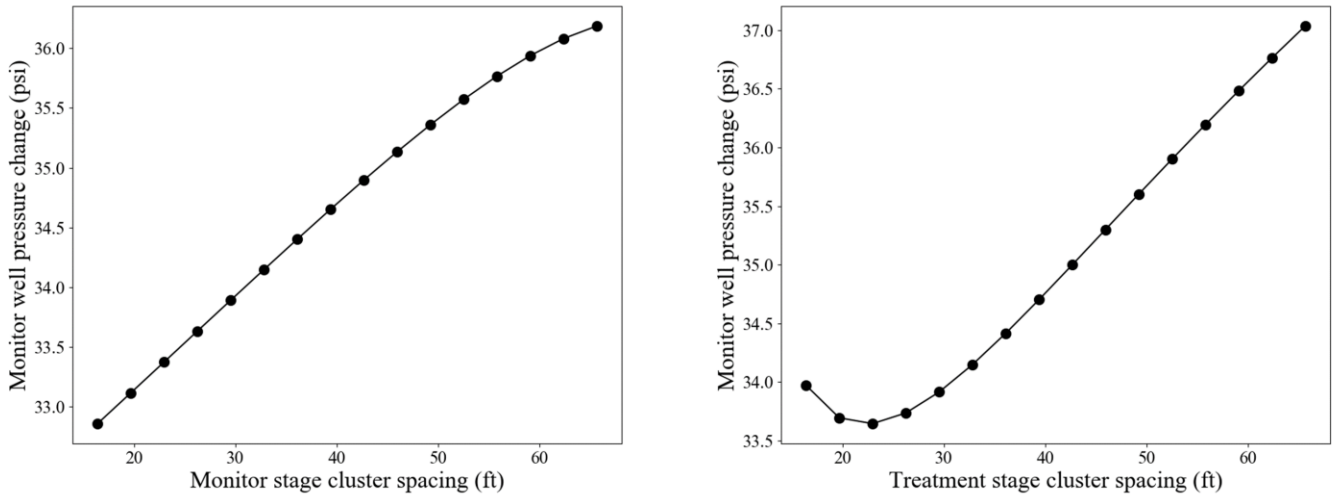

Figure 20: Impact of monitor well cluster spacing and treatment well cluster spacing on monitor well pressure change.

Impact of Lateral Distance Between Fractures

The stress interference induced by the treatment well fractures on the monitor well fractures decreases with an increase in the distance between the two stages. This decrease in the distance leads to a decrease in the simulated monitor well pressure change as shown in Figure 21. As the stages are placed far enough away, the simulated monitor well pressure change becomes negligible.

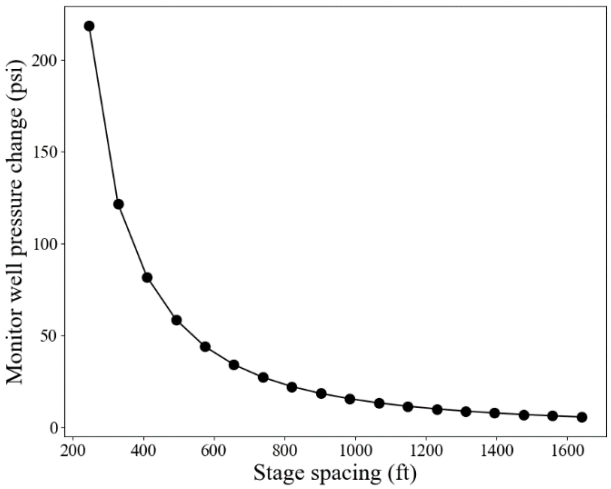

Figure 21: Impact of perpendicular distance between first clusters of the monitor and treatment wells on the monitor well pressure change

Impact of Horizontal Well Spacing

The horizontal distance between the wells directly affects the overlap area between the treatment and monitoring well fractures. An increase in the horizontal well spacing reduces the overlap area between the sets of fractures and reduces the monitor well pressure change. This is clearly illustrated in Figure 22.

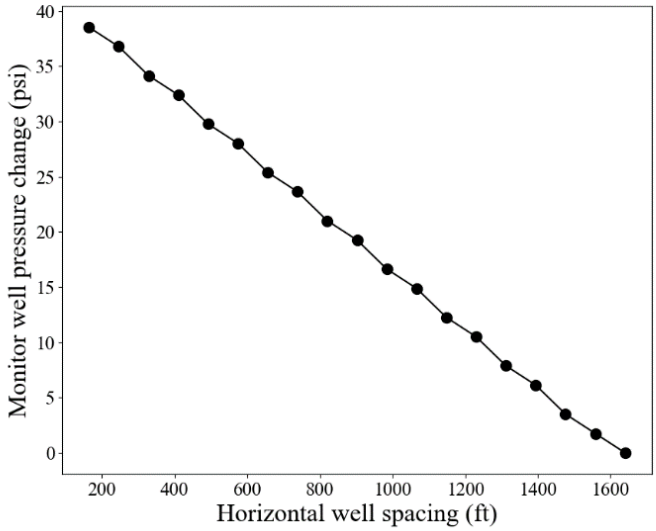

Figure 22: Impact of horizontal distance between the monitor well and the treatment well on the monitor well pressure change

Impact of Vertical Well Spacing

Figure 23 illustrates the impact of the vertical distance between the monitor well and the treatment well on the simulated monitor well pressure change. The results shown are symmetric around the center point which signifies that both the wells are in the same horizontal plane. Moving the wells above or below leads to a decrease in the stress interference between the fractures and decreases the simulated monitor well pressure change.

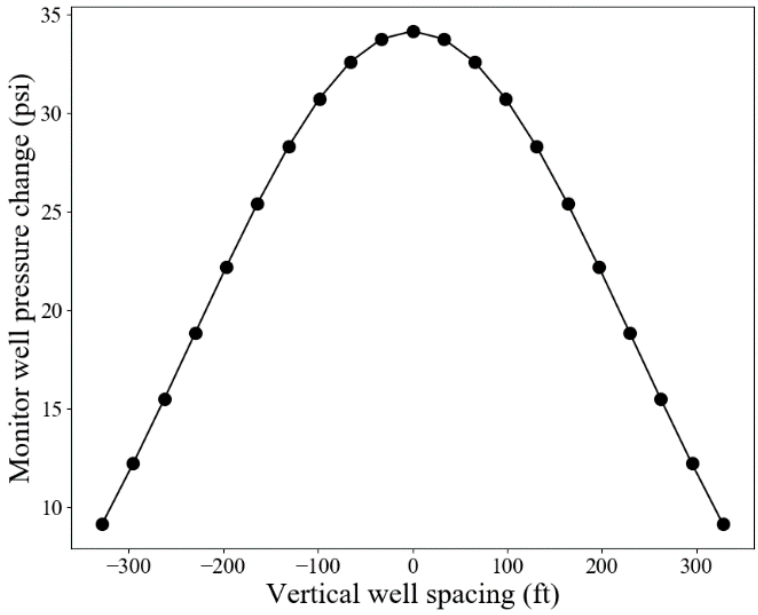

Figure 23: Impact of the vertical distance between monitor well and treatment well on the monitor well pressure change

Inversion Algorithm

The parameter sensitivity results shown above suggest that the observed monitor well pressure change depends on several different parameters. Some of these parameters are accurately determinable in the field while others are unknown. The fracture geometry parameters are the primary unknowns in most field scenarios. Using the monitor well pressure change in multiple monitoring wells, an estimate can be made with reasonable accuracy about the fracture geometry

in the considered wells. This makes the fracture half-length and fracture height the independent variables that need to be calculated in a realistic scenario. These variables can be calculated by inverting for the observed monitor well pressure response. An objective function is defined and shown in Eq. (16). This objective function can be minimized by changing the length and height of the fractures in the treatment and monitor well stages involved.

$$Obj\_fun\_rel = \sqrt{\sum_{i=1}^{n}\left(1 - \frac{\Delta p_{mi}(l_t, h_t, l_{mi}, h_{mi})}{\Delta p_{mi}^{measured}}\right)^2} \tag{16}$$

Sometimes, the observed pressure change in the monitor wells for the same treatment stage can differ by more than an order of magnitude. In those scenarios, it is recommended to use an absolute error objective function (Eq. (17)) to improve the estimation of the fracture geometries.

$$Obj\_fun\_abs = \sqrt{\sum_{i=1}^{n}\left(\Delta p_{mi}^{measured} - \Delta p_{mi}(l_t, h_t, l_{mi}, h_{mi})\right)^2} \tag{17}$$

3.4 FIELD CASE STUDY

The field data analyzed in this study consisted of several multi-fractured horizontal wells in the Permian Basin. The larger project consisted of 11 wells in total, however, this research focused on a subset of the well data (4 wells and 6 stimulation stages). Figure 24 describes the gun-barrel and cross-section views of the project. The active well or the well that is being stimulated is the B17H, while the three surrounding wells in bold and colored are A13H, B54H, and C37H. One major goal of this project was to determine if communication was present between the three landings or benches within this formation. If fracture overlap and poroelastic signals originating from one bench are present in another, one can conclude fractures have crossed these

layers in the vertical direction. The pressure responses for the treatment in well B17H were recorded on surface pressure gauges in the monitoring wells. Figure 25 shows this observed pressure response in wells A13H and B54H during the stimulation of stage 37 and stage 38 in well B17H.

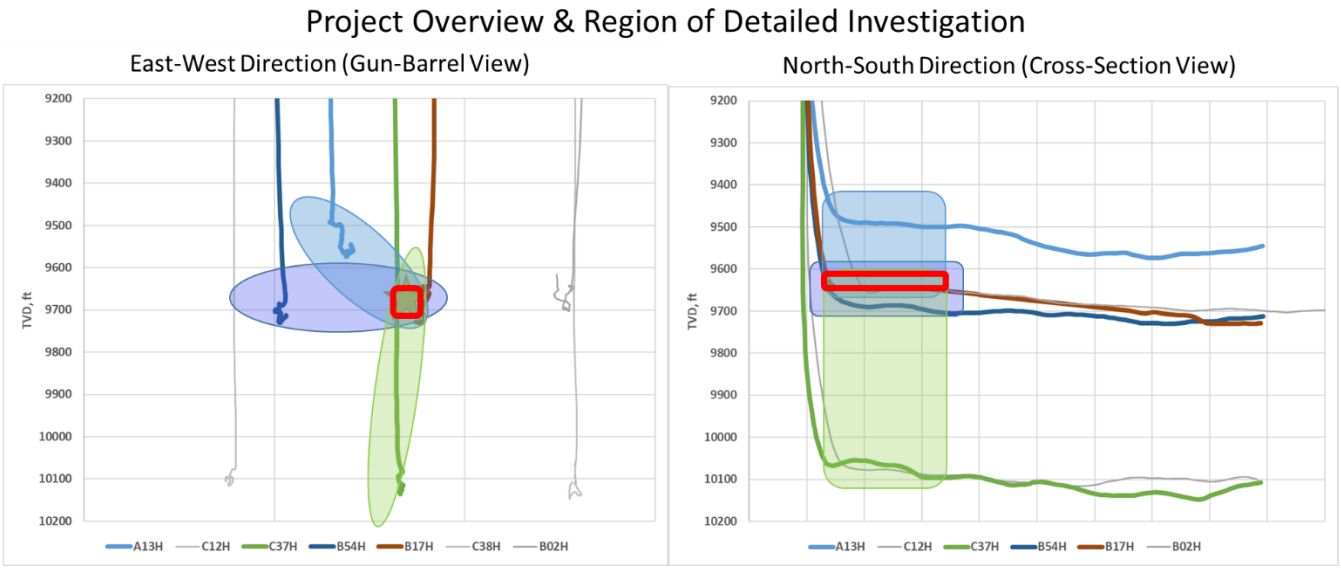

Figure 24: Project overview and region of detailed investigation. Red boxes indicate active stimulation stages which generated responses on monitors in surrounding wells (color-coded by translucent ovals and rectangles).

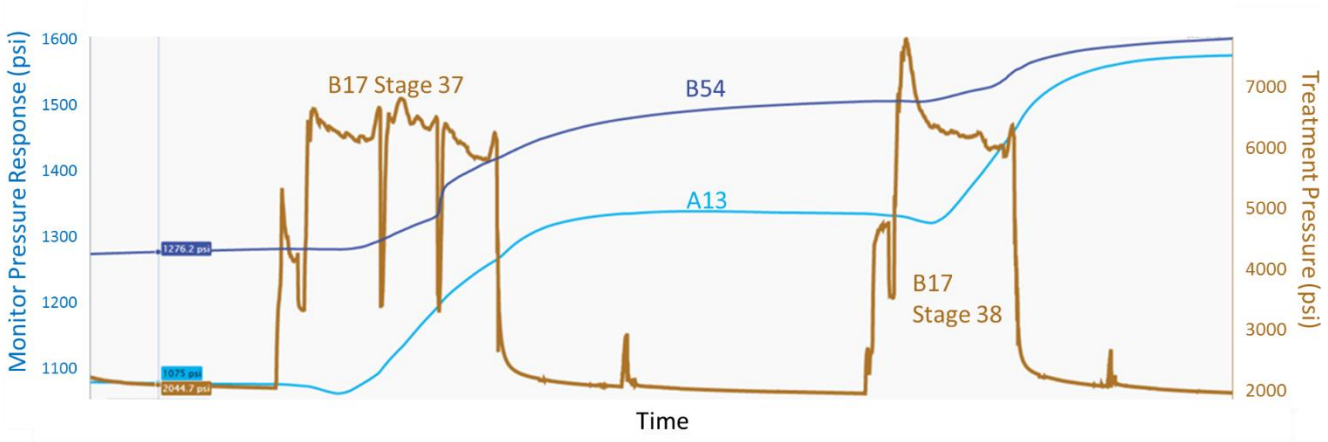

Figure 25: Pressure responses in the monitor wells (A13H and B54H) during offset fracturing of well B17H.

Table 4 shows the calculated bottom-hole pressures in the monitoring wells A13H and B54H during the stimulation of stage 37 and stage 38 in well B17H. The values are directly used in the numerical simulation to compute the stress shadow induced by the monitoring fractures on each other and other fractures using the provided pressure values. Both stages depict a strong poroelastic pressure signal as shown in Table 4 and Figure 25 above. The actual physical poroelastic response in this case could be described as a mixed signature, due to the continual increase in pressure after pumping shuts down. This could be explained by a poroelastic response and either additional fluid moving into the monitor system, or continual fracture growth and overlap. Exact mechanisms are sometimes difficult to identify, and care should be taken to properly interpret the poroelastic pressure response. Given the response time was not immediate, we can interpret this as an actual fracture overlap signature and not a short circuit or direct connection.

Table 4 – Pressures observed in the monitoring wells A13H and B54H during the stimulation of a few stages in well B17H.

	A13H			B54H		
	Initial Pressure (psi)	Final Pressure (psi)	Delta (psi)	Initial Pressure (psi)	Final Pressure (psi)	Delta (psi)
Stage 37	5335	5535	200	5645	5785	140
Stage 38	5595	5740	145	5871	5917	46

The treatment fracture geometry can be calculated for each stage origination and arrival, thus, X, Y, Z location data for each stage and distances calculated between them are needed. A sample of the subset data can be seen in Table 5, which displays active and monitor well details, as well as x, y, z relative distances between the mid-point of each stage and the most notable perpendicular distance between them, which utilizes the regional fracture azimuth of N78^{o}E. Both

monitor wells have the heel stage open and three clusters with 40 ft cluster spacing were stimulated in both wells. The treatment well stages also have three clusters per stage but with 60 ft cluster spacing. Incorporating the fracture azimuth and location of the different fracture clusters in the treatment and monitor wells, we can estimate the effective horizontal well spacing and the stage spacing between the treatment well stages and monitoring well stages. These values have been illustrated for stage 38 in Figure 26.

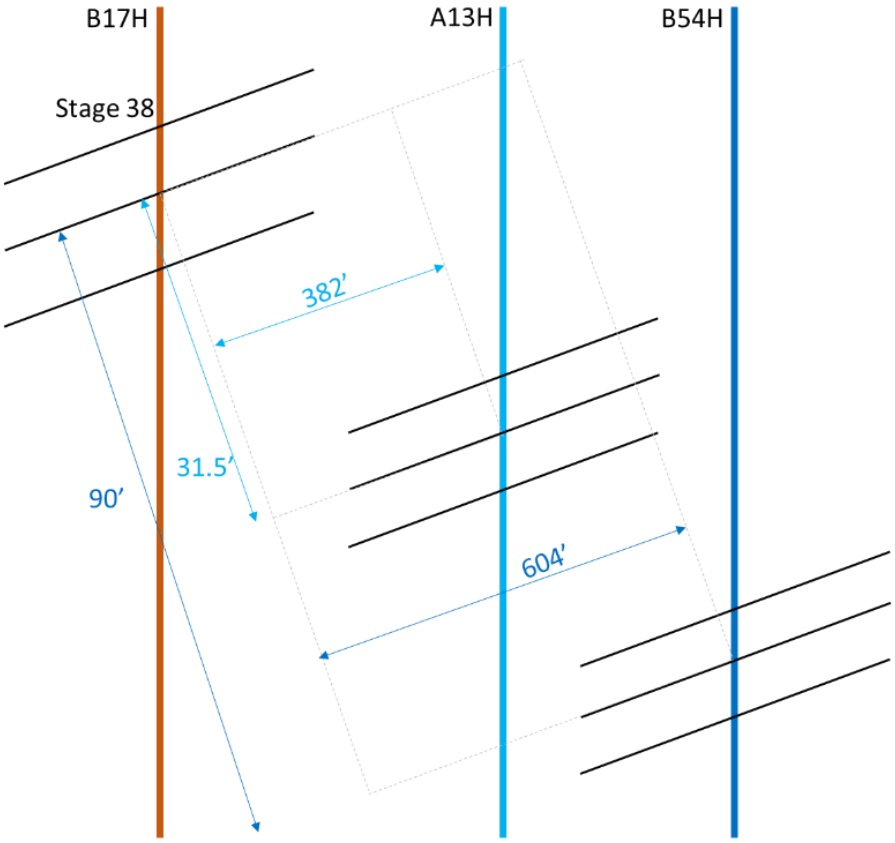

Figure 26: Illustration of the orientation and location of stage 38 in Well B17H and the monitoring stages in wells A13H and B54H. The figure is not to scale.

Table 5 – Stage and well distance summary

Active Stage	Monitor Well	Frac Azimuth Input	TVD Active Stage	Z Distance	Y Distance	X Distance	Horizontal Well Spacing	Treatment – Monitor Stage Spacing
		(Degrees)	(ft)	(ft)	(ft)	(ft)	(ft)	(ft)
34	A13H	78	9646	164	897	497	1025	775
34	B54H	78	9646	23	1009	742	1247	833
35	A13H	78	9646	164	708	501	865	589
35	B54H	78	9646	23	820	746	1087	647
36	A13H	78	9646	163	519	503	704	403
36	B54H	78	9646	23	631	748	926	462
37	A13H	78	9646	163	330	505	543	218
37	B54H	78	9646	23	442	750	765	277
38	A13H	78	9646	163	140	510	382	32
38	B54H	78	9646	23	252	754	604	90
39	A13H	78	9646	163	49	512	305	-58
39	B54H	78	9646	23	62	757	442	-96

For stages 37 and 38 in well B17H, the measured ISIP values converted to downhole conditions are 6745 psi and 6500 psi respectively. The corresponding monitor well pressure changes induced by these stages have been tabulated and shown above. Using the parameter values described above and using the inversion model developed in this work, the fracture dimensions can be determined for the fractures in the treatment and monitor wells. In order to reduce the number of unknowns, an assumption is made that the fracture half-length and height of the fractures in each stage are uniform. An additional constraint is included in the system that uses the same fracture geometry in the monitoring stage of wells A13H and B54H. Thus, there are eight unknowns in the system – half-length and height of monitoring stage fractures in well A13H, of monitoring stage fractures in well B54H, of stage 37 fractures in well B17H, and of stage 38 fractures in well B17H. The Simplicial Homology Global Optimization algorithm that is part of the scipy library (Virtanen et al. 2019) in python is used to find the global minima of the objective function shown in Eq. (16). Three scenarios were considered: one fracture per stage, two fractures per stage and three fractures per stage. For each scenario, an estimate of the geometry was obtained for the fractures by minimizing the objective function. The results of this exercise are shown in

Table 6. The fracture geometries vary significantly depending on the number of fractures created in each stage. This non-uniqueness in the simulation results can be decreased by constraining the solution using other possibly available data from the field operations. For example, the total pumped slurry volume can be used to constrain the solution and help ignore the solutions that depict fracture volumes larger than the volumes pumped. Microseismic data, if available, could be used to constrain the fracture half-length and height. Water-hammer data can also provide estimates of fracture geometries that can help bind the results from the methods discussed in this work (Hwang et al. 2017).

Table 6 – Results of global minimization of the objective function for the shown field scenario

	1 fracture per stage		2 fractures per stage		3 fractures per stage	
	Half-Length (ft)	Height (ft)	Half-Length (ft)	Height (ft)	Half-Length (ft)	Height (ft)
A13	435	435	364	809	644	928
B54	729	729	937	850	582	805
B17 Stage 37	683	683	929	363	923	354
B17 Stage 38	745	745	523	344	367	50

The number of fractures in the monitoring stages and treatment stages are uniform across the three scenarios. In reality there could be a different number of fractures created in each considered stage. There are actually 3^4 possible combinations of the number of fractures between all the stages. The number of fractures per stage could also be optimized using the minimization algorithm. This would make the total number of unknowns twelve instead of eight. Off-balance growth of fractures is commonly observed in 3-D numerical simulations (Manchanda et al. 2019c). Thus, the model needs to be extended to consider individual wings of the fractures and determine the half-length of each fracture wing independently. The application of the developed model in real-time requires real-time estimation of the treatment fracture pressure by eliminating the pressure drop across the wellbore, perforations, and near-wellbore region. Another requirement for real-time application is to make the developed model in this work more efficient so that it can

run faster. This can be done by eliminating some of the numerical integration components used in the model with analytical integration.

Conclusions

A new semi-analytical model to calculate poroelastic pressure interference between fractured horizontal wells has been developed. The model is significantly more efficient than a numerical simulation and can be inverted to estimate the fracture dimensions of propagating and monitoring fractures. The model is very accurate, as shown by the comparison with a representative numerical model. The model's sensitivity to various parameters has been evaluated, and the results have been physically explained. The most critical parameters that affect the model calculations are the overlap area of the treatment and monitor well fractures, the lateral distance between the treatment and monitor well stages, the horizontal well spacing, and the vertical well spacing. This is in agreement with the conclusions from previous numerical work (Seth et al. 2018).

The new methodology is applied to a field scenario in the Delaware Basin. The response of the stimulation of two stages in the treatment well (B17) on two monitor well stages (A13 and B54) are compared with model predictions. The model predictions are used to estimate the fracture half-length and the fracture height in each well using a global optimization inversion model. By changing the number of assumed fractures in each stage in the system, a solution can be obtained for different estimates of the fracture geometries.

Chapter 4. Wellbore Strain as a Fracture Diagnostics Tool[2]

This section seeks to establish a fundamental understanding and tools necessary to develop new workflows and methods of using wellbore measurements and strain for fracture diagnostics. Fully coupled simulations using Multi-Frac-3D have yielded clear insights into the expected strain and displacements in the subsurface during fracturing. These models have been leveraged and improved upon to develop methods for interpretation of downhole strain measurements. Several mechanisms will be discussed in this section, but as technology progresses, the list of solutions will undoubtedly expand.

Pressure interference and fracture to well interaction in unconventional formations during hydraulic fracturing has been shown to yield great insights into the geometry of propagating fractures. Interpretation of this poroelastic pressure response data can be used to estimate key unknown elements of the fracture geometry. Currently, only fracture shadowing solutions or fiberoptic strain events have been investigated in great detail, with little to no research on understanding the impact on the wellbore deformation/strain expected due to offset hydraulic fracturing. Recent field measurements of wellbore strain from fiber optics have shown casing deformation in various basins. Wellbore measurements such as DAS, DTS, and DSS collected through permanent or temporary downhole fiber optics have proven to be exceptionally useful but are typically prohibitively expensive to install in thousands of wells. There is a need for simple,

[2] This section is adapted from paper SPE-209120-MS (Elliott, Brendan, Zheng, Shuang, Russel, Rod, Sharma, Mukul, Haustveit, Kyle, and Jackson Haffner. "Integration of Sealed Wellbore Pressure Monitoring Responses with Wellbore Strain and Deformation Measurements for Fracture Diagnostics." Paper presented at the SPE Hydraulic Fracturing Technology Conference and Exhibition, The Woodlands, Texas, USA, February 2022
* Elliott was the main contributor to this work, developing the relationships of wellbore strain to sealed wellbore pressure changes, analytical modeling, laboratory validation experiments, and numerical modeling, as well as history matching field responses. Zheng develop code advancements in the numerical code and deployed novel meshing methods in the simulator, Russel guided the laboratory experiment setup and equipment, and Sharma supervised the research.

high-speed tools that can guide the design and execution of stimulations with insight into the position and geometry of the propagating fractures. This can be done through a coupled understanding of fracture propagation, wellbore strain, deformation, and resulting sealed wellbore pressure responses.

4.1 FRACTURE INTERSECTIONS OF WELLBORES

Recently the industry has monitored wells and fracture intersections via fiberoptic cross well strain (Ugueto et al. 2019). This known phenomenon is becoming increasingly common as a fundamental diagnostic technology for unconventional developments. Fiberoptic cable, whether permanently or temporarily installed, is used to measure strain as a hydraulic fracture propagates. This technology has clearly shown tensional strain fronts leading the fractures, and compressive regions around the fractures as it passes the wellbores (Figure 27). Furthermore, the relaxation, or strain reversal, has been seen as the pumps shut down and the job ends. This diagnostic provides field observations that hydraulic fractures do indeed intersect offset wells in many unconventional reservoirs, providing validation and utility for wellbore measurements, which is the focus of this proposal.

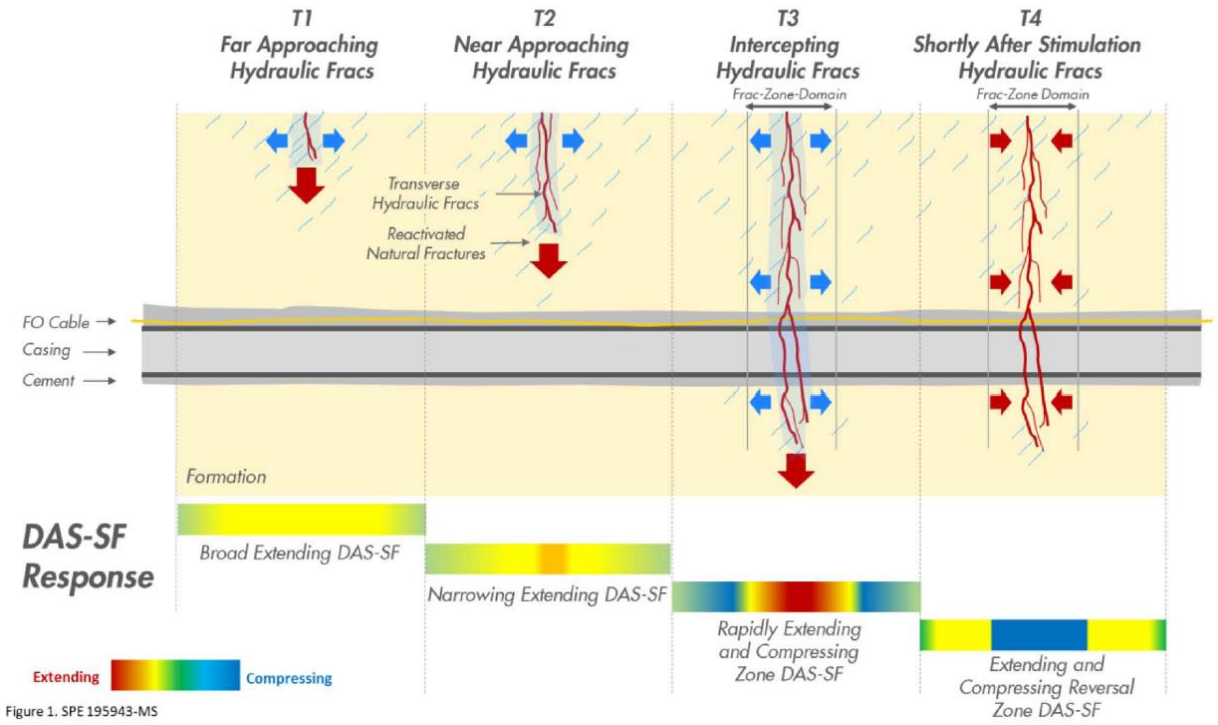

Figure 27: Example downhole fiber optic DAS responses from fracture intersecting the wellbore

The methods and procedures deployed in this work fit into four main categories: lab testing, analytical modeling, numerical modeling, and field data history matching as seen in Figure 28. In a laboratory environment, the physical deformation and strain on a joint of casing due to applied loads can be directly measured. This simple yet critical experiment guides our future expectations for wellbore deformation and characterizes the magnitudes of strain and displacement that should be emulated through numerical modeling. The second phase is deploying existing analytical models for thick wall pressure vessels. These expressions allow for the prediction of internal pipe displacement given external loads, under a wide variety of pressure and casing wall thickness and size ranges. Numerical modeling captures the coupled nature of the fracture to rock interaction and incorporates a far field strain response during propagation. Furthermore, numerical models allow for greater utility and prediction of true strain responses once calibrated to the laboratory and analytical models. Finally, induced deformation can be modeled, and history matched using

field data from sealed wellbore pressure monitoring or fiber cross well strain. This step is the key to developing a robust diagnostic method anchored to multiple field measurements.

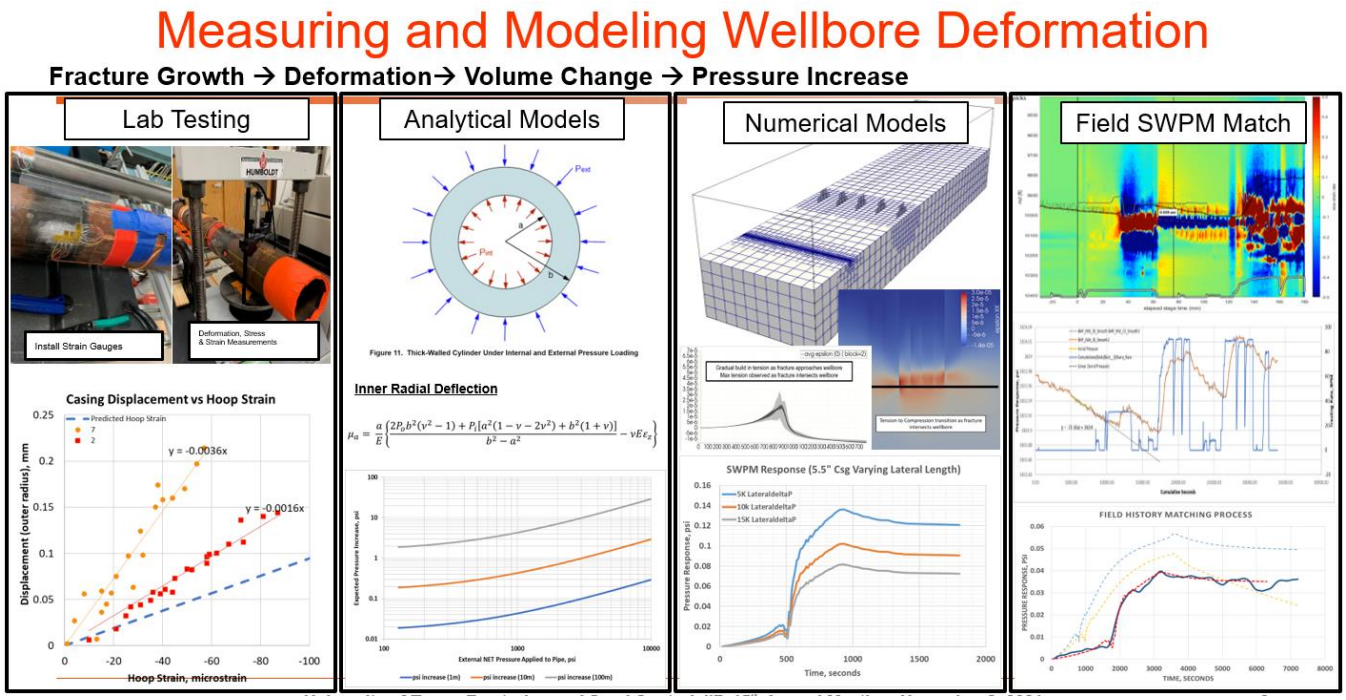

Figure 28: Methods deployed to measure and model wellbore strain and deformation

4.2 LABORATORY VALIDATION OF CASING DEFORMATION

To understand the complex dynamics of downhole wellbore strain measurements some fundamental comprehension and basic measurements must be conducted in a controlled laboratory setting. Developing extensive measurements that can be predictable and correlated to known analytical or numerical solutions is fundamental to ensure the predictive accuracy of the proposed strain measurement methods. Laboratory work making detailed measurements of casing deformation, strain, and stress has been completed and is discussed in this section.

A joint of 5.5" 23# P-110 casing was prepared for strain gauge installation by sanding and polishing the external surface, wherein multiple strain gauges were installed azimuthally in

multiple orientations to make hoop and longitudinal strain measurements (Figure 29). A Humboldt load frame applied a systematic and incremental load on the pipe while the physical pipe deformation and strain measurements were recorded with high accuracy linear variable differential transducer (LVDT) sensors.

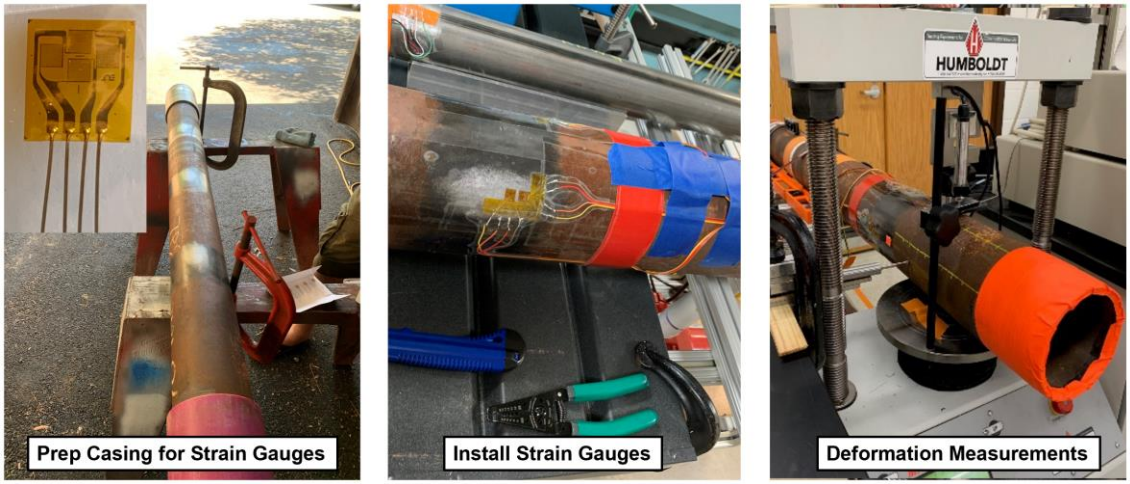

Figure 29: Images of casing preparation and laboratory setup on 5.5" P110 23# casing

The casing was stressed up to 10,000 lbs. This maximum load exerted results in loads of up to 40,000 psi on the casing over a measured $0.25in^2$ area of interaction. Through the investigation of laboratory strain measurements on the casing, the measured circumferential strain is on the order of 0-300 microstrains for deformations of 0-0.75 mm (0-0.03 inches). These displacements are subtle but measurable with a high degree of accuracy. Repetitive testing was performed to validate the expected load versus displacement trends and tied to the previously mentioned analytical expressions. Figure 30 displays these results as the measured outer diameter displacement versus load under a wide range of multiple loading scenarios, with the analytical solutions shown as solid lines. Note the measured outer displacement correlates very well with the analytical expression for outer diameter displacement. Given Physical experiment limitations, inner displacement is difficult to measure and therefore not displayed

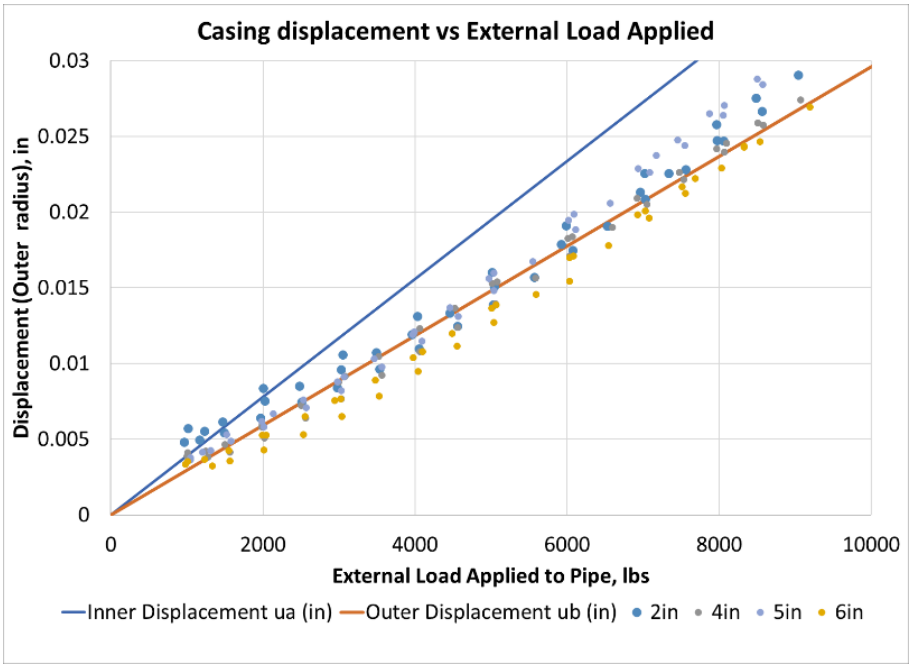

Figure 30: Displacement versus applied load.

The trend, as expected, is linear and elastic. Subsequent loading and unloading cycles confirm that the deformation is elastic (Figure 31). It is important to note that the azimuthal response to the loading is a positive strain perpendicular to loading, and a negative strain in line with loading. These predictable responses can be simplified to linear trends that can directly tie the linear strain response to load. For example, in Figure 31, strain is a linear function of the applied load. For this case strain can be predicted by utilizing a factor of 0.0102 multiplied to the applied load.

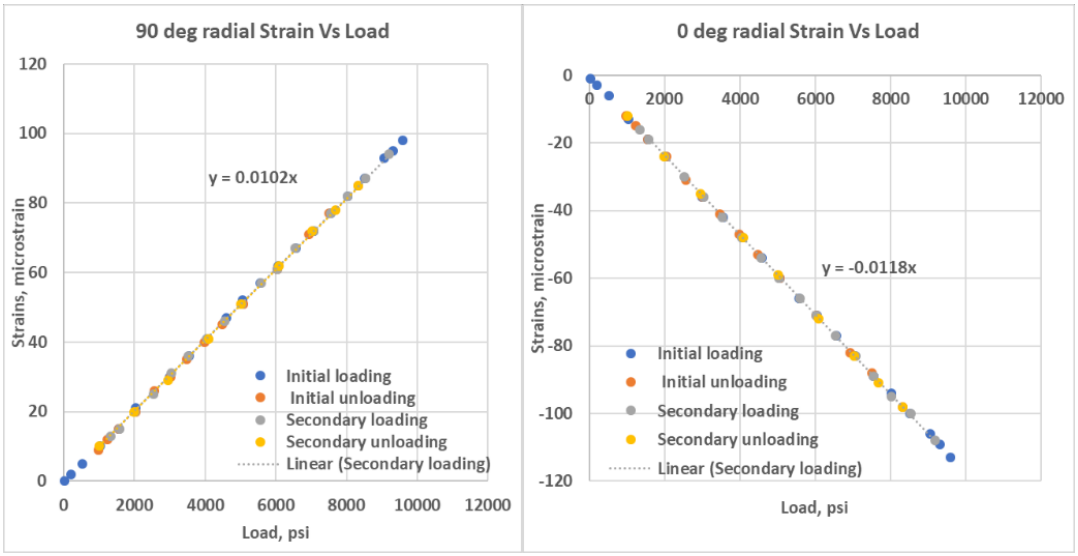

Figure 31: Elastic behavior of casing under loading conditions. Note linear relationship of measured strain vs load applied.

Analytical models based on deformation of thick-walled cylinders show that strain dissipates away from the applied load in pipes and tubulars. This observation was also validated through laboratory experiments. At the direct point of loading, strain gauges should read a maximum tension or compression (depending on the azimuthal measurement), and as strain is measured away from the loading point, its value dissipates until it is not felt in the casing. This provides an extremely useful way to triangulate single or multiple fractures by measuring local maxima. Figure 32 displays this effect in a concise manner where the maximum deflection is expressed as the solid line and the dots are the measured strain response at varying distances away from the load. The strain measured farther away from the loading point shows a degradation of strain with distance.

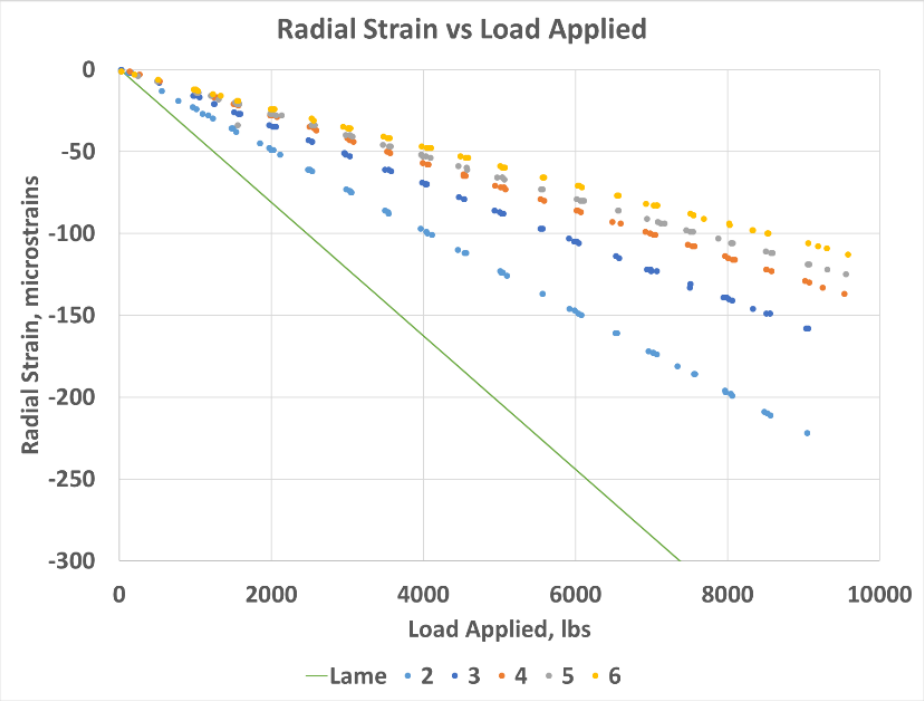

Figure 32: Casing strain measurements as a function of distance (in inches) from applied load.

Figure 33 shows the initial lab measurements coupled with the 3D simulation. One can observe that the strain and displacement measured close to the applied load is larger than the strain measured farther away. This variation along the casing with distance can allow for an approximation of a local minimum, which can diagnose fracture intersection. For example, for a given displacement of 0.1 mm the expected strain 2 inches away is -60 microstrain, and 7 inches away is -30 microstrain. The blue dashed line in Figure 33 displays the expected analytical deformation from existing analytical equations. Correlating the measured values of strain to distance allows us to compute the incremental change in the wellbore volume which is directly related to any changes in the sealed wellbore pressure. Furthermore, anchoring the analytical expressions with experimental measurements allows us to construct a reliable inverse model that can provide estimates of fracture parameters from an observed downhole strain measurement.

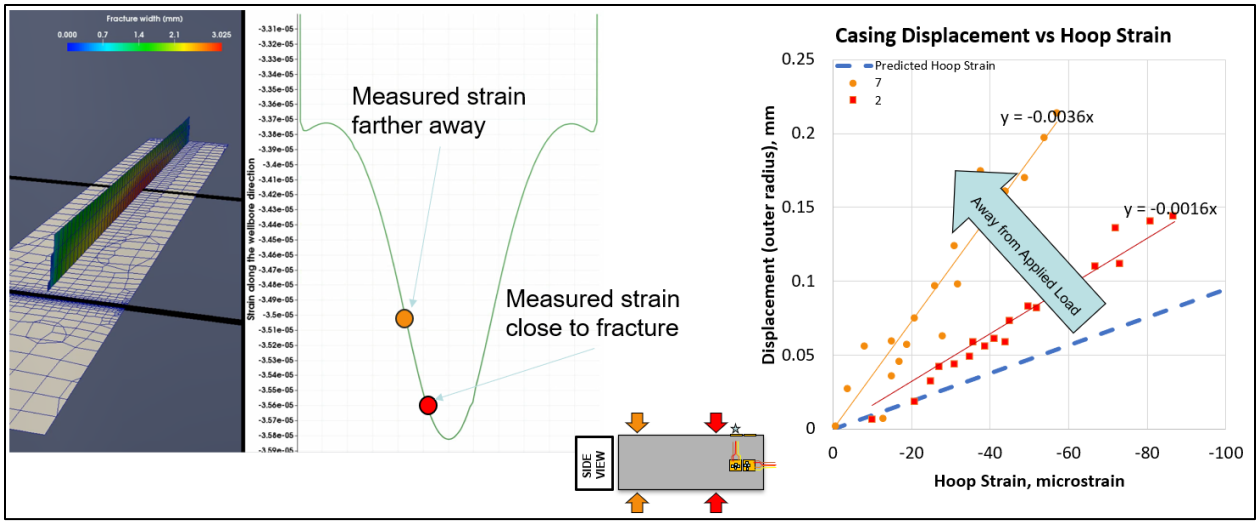

Figure 33: Example of coupling the observed strain and displacement with 3D simulations from MultiFrac-3D

4.3 SEALED WELLBORE PRESSURE MONITORING

Sealed wellbore pressure monitoring (SWPM) is a low cost, non-intrusive technique that allows the operator to evaluate and quantify fracture growth rates and fracture driven interactions during the hydraulic stimulation (Haustveit et al. 2020). The technique measures the exact point when a fracture intersects another wellbore and has been validated by Distributed Acoustic Sensing strain monitoring, microseismic, video-based perforation imaging, and production logging.

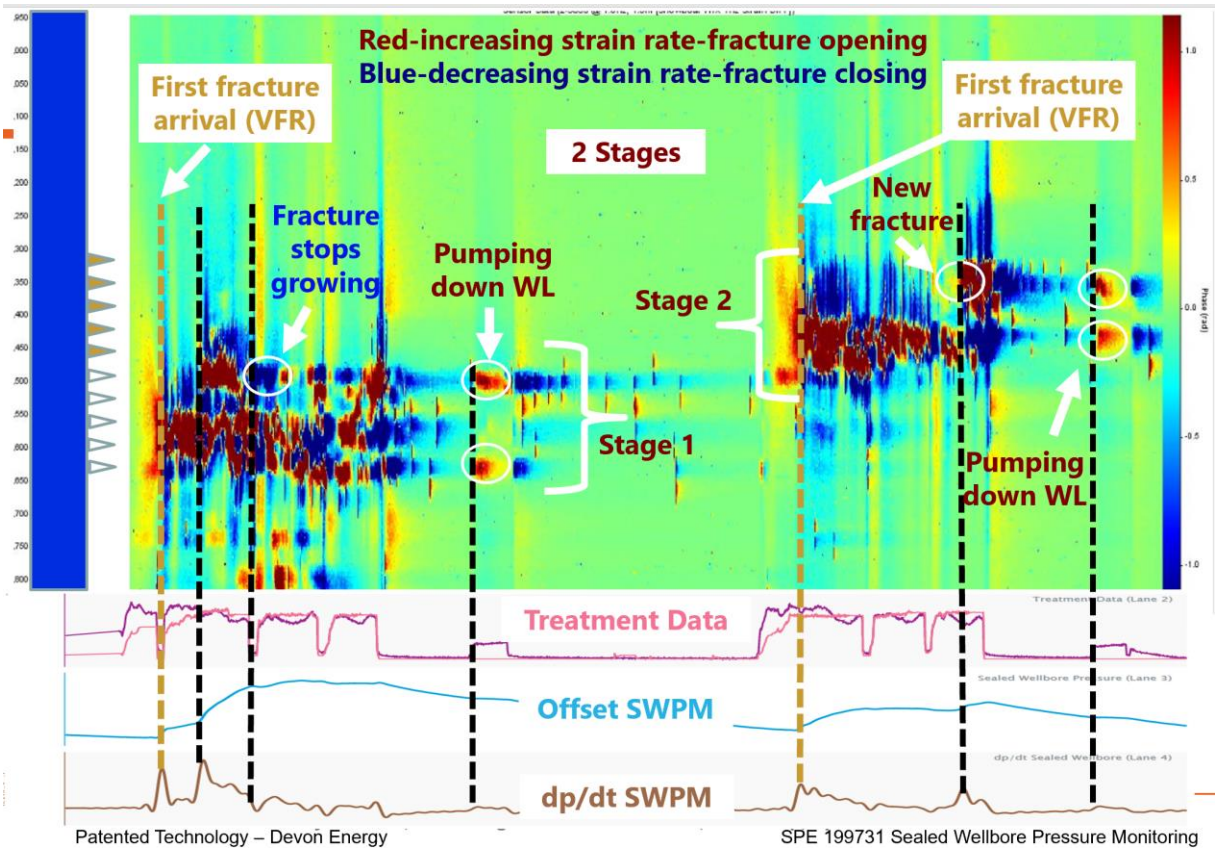

Figure 34: Sealed Wellbore Pressure Monitoring Ties with Cross Well Fiberoptic Strain

Figure 34 displays two fracture stages with a waterfall fiberoptic plotting strain vs time, along with the treatment pressure data and the offset SWPM data at the bottom. The fiberoptic cross well strain arrival is consistent with the pressure inflection on the offset monitor wellbore.

Monitoring the pressure change induced in a sealed wellbore provides an indication of when a fracture arrives and intersects the casing. As the fracture moves past the casing, the increasing compressive stresses are transferred to the casing resulting in a small volume change within the casing, and inducing a positive pressure response at the surface. This behavior is expressed through Equation 1 which combines the analytical wellbore deformation and compressibility of the fluid system.

$$\Delta P_{ID-comp} = \frac{4*L*dP_{OD}*b_0^2(E*b_0^2-E*a_0^2-dP_{OD}*b_0^2}{c_w*D*E^2(b_0^4-2*b_0^2*a_0^2+a_0^4)} \quad \textit{(Eq. 1)}$$

Work has been published on this concept validating the mechanisms of wellbore strain, and the correlation to the sealed wellbore pressure monitoring signature (Elliott, et al. 2022)

By coupling the Lame deformation expressions with fluid compressibility in a sealed wellbore volume, the volume change and displacement required to generate the observed SWPM responses in the field (on the order of 0.01 - 10 psi). Pressure increases in a closed vessel (casing) due to a volume reduction can be estimated with Equation 2.

$$C_t = -\frac{1}{V}\left(\frac{dV}{dP}\right) \rightarrow rearrange \rightarrow dP = \frac{1}{C_t}\left(\frac{dV}{V}\right) \quad \textit{(Eq. 2)}$$

Where, C_t = Fluid compressibility, 1/Pa

V = Volume of sealed wellbore, m^3

dV = Volume change of wellbore due to fracture, m^3

dP = Pressure change due to volume reduction, Pa

Once volume reduction is estimated from the applied loading of the casing through the displacement expression in Equation 1, the change in pressure due to the deformation of the casing is computed with Equation 2. The resulting workflow yields a method to estimate SWPM changes resulting from externally applied loads, with the assumption that external stresses are applied radially on the casing.

As can be seen in Figure 35, when the external pressure is uniformly applied on the external surface of the casing, a coupled deformation and pressure increase is expected. With additional

length of deformation, the expected pressure response increases proportionally. For example, 200 psi net pressure acting over a 10 meter section of the casing would yield a 0.2 psi increase at the surface, while that same net pressure acting over a 100 meter section of casing (more typical stage length) would generate a 2 psi surface pressure response.

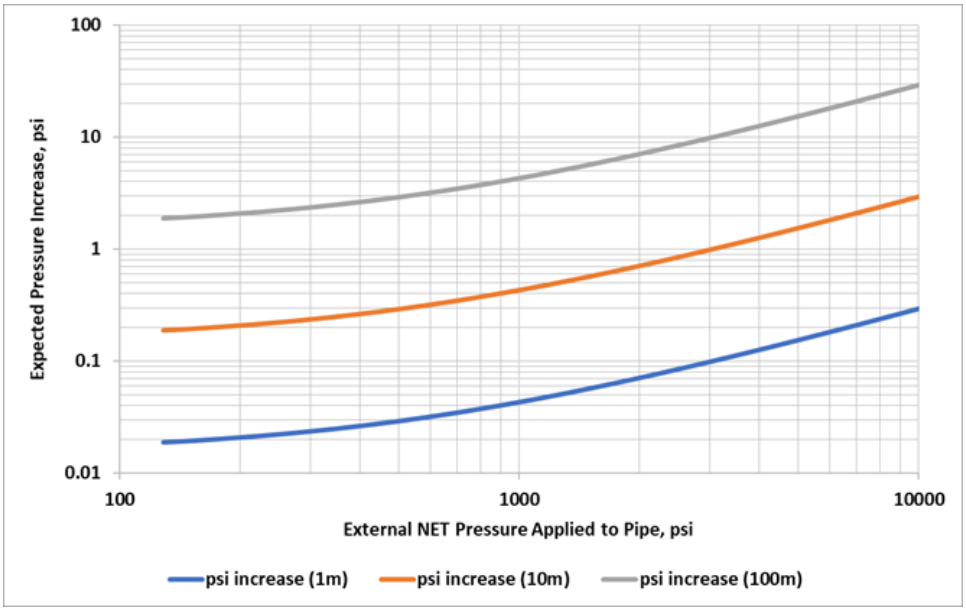

Figure 35: Expected pressure responses vs external net pressure applied to casing.

Figure 36 charts the expected pressure increase relative to the inner radial deflection, and the figure yields insights into how much internal diameter change is necessary to generate typically observed pressure responses. It is important to note that the sealed well responses are typically elastic, that is, no hysteresis is observed, and the deformed state should rebound to initial conditions. For radial deformations larger than ~5%, the casing may suffer permanent damage, and for that reason the plot is projected to a 5mm displacement. The most likely range for magnitudes of deformation on production casing are in the range of 0.1-1 mm. It can also be noted that the potential error in the pressure gauge estimate will be very small given the industry standard high resolution gauges that can measure pressure down to 0.001 psi changes.

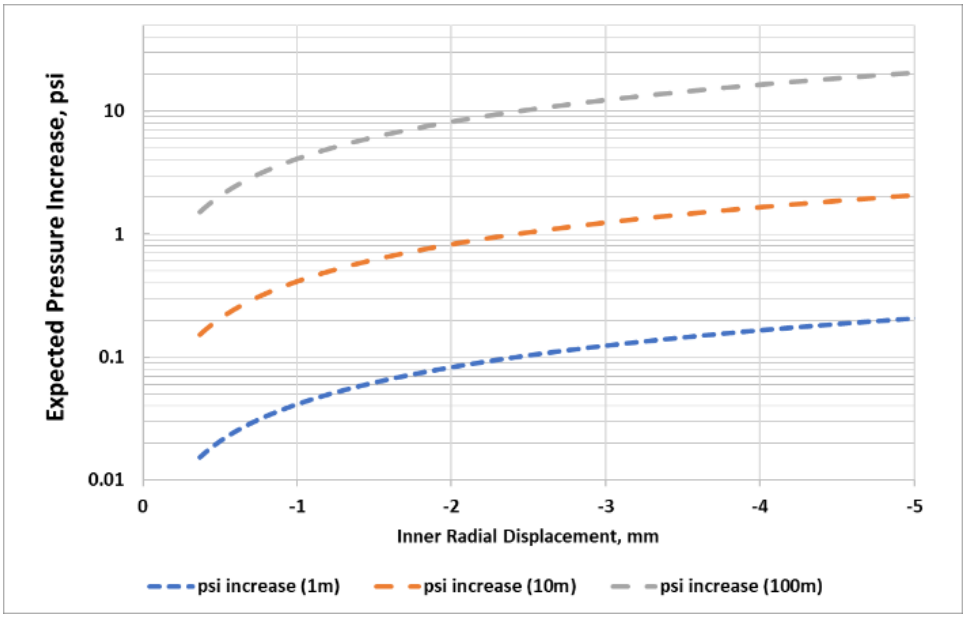

Figure 36: Expected pressure response vs radial displacement.

Consideration should be made for the compressibility of the fluid residing in the wellbore during the monitoring period. Most typically, the fluid left in the wellbore after cement has been displaced during the drilling phase is either fresh water or weighted brine. The effects of brine salinity, temperature, and gases present in the system greatly alter the resulting value of compressibility (Osif 1988). The correlation presented in Equation 3 estimates the compressibility of brines for a wide variety of oilfield conditions.

$$C_w = (7.033 * P + 541.5 * C - 537 * T + 403.3 * 10\text{^}3)^{-1} \quad \text{(Eq. 3)}$$

Where: P = Pressure, psi

C = Salt concentration, g/L

T = Temperature, degF

For the purposes of this work, the compressibility value helps to scale the magnitude of a given pressure response. Assuming similar volume of deformation on the casing, the expected compressibility is increased for higher temperatures, and with higher pressure or higher brine

concentrations, the expected compressibility is smaller. Likewise, the expected sealed wellbore pressure response increases with additional pressure or brine concentration. Figure 37 displays the values of compressibility corresponding with varying salt concentrations at three different wellbore pressure conditions.

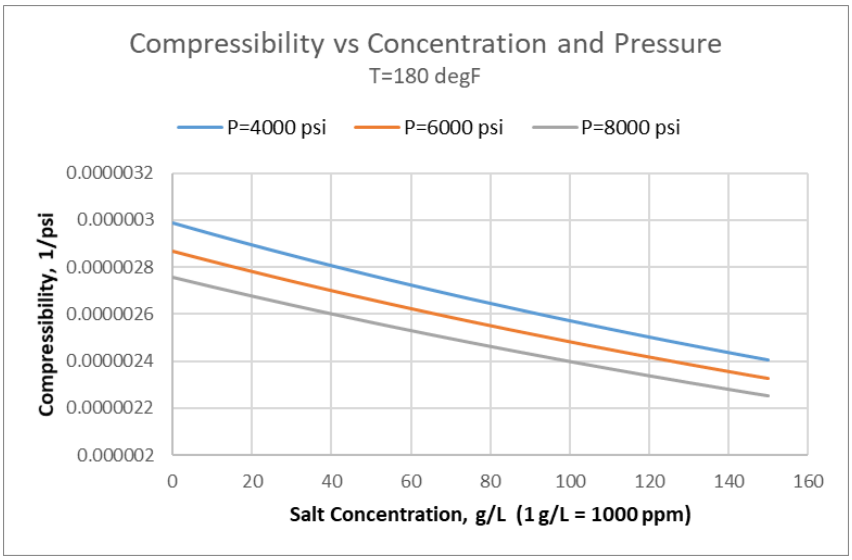

Figure 37: Compressibility as a function of salt concentration and pressure.

Figure 38 shows the current mental model presented in Figure 35 and Figure 36. The limitation of the analytical model is evident in the simplistic idealized deformation of a constant region of pipe, where, in reality, this deformation has been observed to dissipate away from the load. Research later in chapter 5 will display SWPM pressure predictions based on a wellbore strain profile utilizing the full 3D strain profile of a propagating fracture. Coupling the 3D numerical wellbore modeling to this pressure response expectation yields great insight into a wide variety of fracture parameters as discussed in section 5. Capturing the full deformation field across the wellbore due to the displacement of the formation allows a more accurate description of the wellbore deformation, something the analytical models simply cannot characterize appropriately.

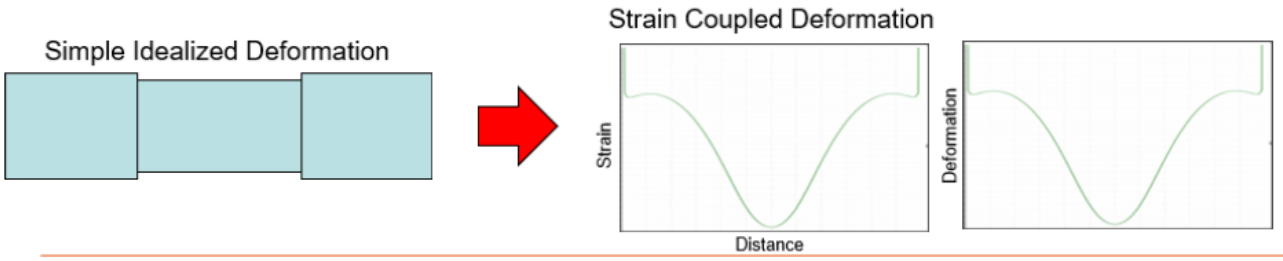

Figure 38: Mental Models for Casing Deformation

4.4 THICK-WALL PRESSURE VESSEL LOADING

There are well known linear displacement equations developed for thin and thick wall pressure vessels. These can be used to gain an initial understanding of the expected wellbore strain and deformations from various loading cases and they can later be used to develop an inverse model that predicts fracture displacement and geometry.

A thick-wall pressure vessel is generally defined as a vessel with a wall thickness greater than $1/10^{th}$ of the vessel radius. Most oilfield tubulars, especially production casing, conform to this definition. For example, 5.5" 23# P-110 casing has an outer radius of 5.5" and an inner radius of 4.67", which the ratio (t/r) is .35, far exceeding the thick wall definition criteria. The linear solution to this thick-walled pressure vessel loading problem was presented by French mathematician Gabriel Lame in 1883. He computes the radial and hoop stresses at any radial location. The derivation requires standard

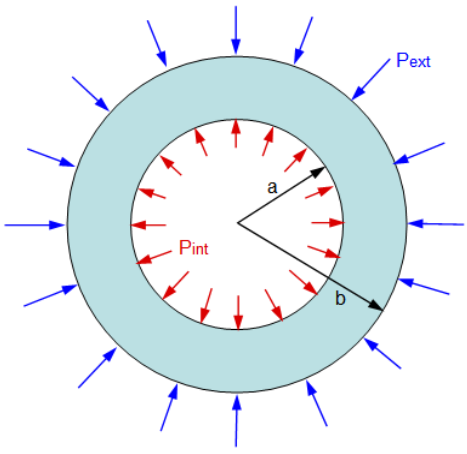

Figure 39: Thick-walled cylinder under constant external and internal pressure loading

applications of force equilibrium, linear strain-displacement relations, and isotropic Hookean constitutive relations. If we assume the wellbore is a thick wall cylinder and external pressure is uniformly distributed and acting on the outside of the casing we can use the Lame equations to predict the displacement and thus volume change in the wellbore.

The 3D strain relations for radial and circumferential strain for an isotopic Hookean material (one which exhibits linear stress versus strain curves and full reversibility of strain with no hysteresis) are given in Equations 4 and 5

$$\varepsilon_r = \frac{1}{E}[\sigma_r - \gamma(\sigma_\theta + \sigma_z)] + \alpha T \quad \text{(Eq. 4)}$$

$$\varepsilon_\theta = \frac{1}{E}[\sigma_\theta - \gamma(\sigma_r + \sigma_z)] + \alpha T \quad \text{(Eq. 5)}$$

Combining the linear stress-strain relation we can obtain an expression for displacements at the inner and outer surfaces due to externally loading the vessel (Equation 6). These expressions can be utilized to predict the internal diameter change and thus volume change expected for the wellbore.

$$u_a = \frac{a}{E}\left\{\frac{2P_o b^2(\gamma^2 - 1) + P_i[a^2(1 - \gamma - 2\gamma^2) + b^2(1 + \gamma)}{b^2 - a^2} - \gamma E \varepsilon_z\right\} + a(1 + \gamma)\alpha T \quad (Eq. 6)$$

Additional expressions for wellbore integrity assessment considering casing-cement-formation interaction are provided by De Simone et al. (2017) and Pereira et al. (2017). Analytical

and numerical solutions of load and stress on casing and cement, coupling the pipe and cement, are presented by Qu et al. (2013).

4.5 NUMERICAL SIMULATION OF WELLBORE STRAIN AND DEFORMATION

A fully integrated compositional 3-D hydraulic fracturing and reservoir simulator has been developed and is used to investigate the coupled deformation and wellbore strain phenomenon (Zheng et al. 2020, Manchanda et al. 2020). First, a gridded wellbore with a suitable thickness for the steel casing is modeled with a highly refined mesh. Due to the level of refinement around the wellbore, the simulation domain often contains millions of cells using advanced meshing algorithms. The smallest level of refinement for the wellbore is 20% of the casing thickness and the formation has nine levels of refinement in close proximity to the monitor wellbore. The smallest mesh size is 512 times smaller in linear dimensions and 134 million times smaller in volume than the largest mesh.

A fully integrated 3-D hydraulic fracturing and reservoir simulator is used for the Numerical modeling of wellbore strain. This simulator solves for the strain tensor, fluid pressure and other variables as noted in (Figure 40) while propagating multiple fractures within the coupled reservoir-fracture-wellbore domain (Zheng et al., 2019; Manchanda et al., 2020; Zheng et al., 2021; Zheng and Sharma, 2021).

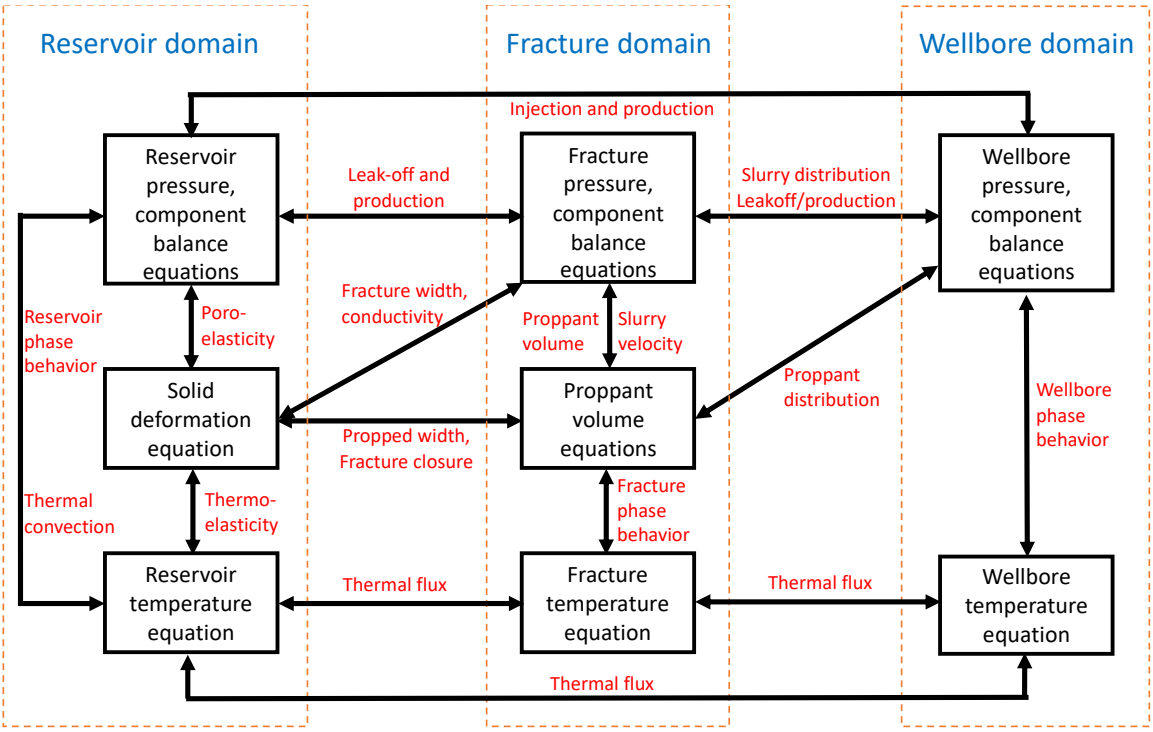

Figure 40: Schematic of the coupled nature of the integrated physics of the numerical simulator

This fully integrated simulator is used to simulate the hydraulic fracture propagation and wellbore interactions. The simulator includes several key physical processes; solid mechanics, flow in porous media, fractures and wellbores, and fluid distribution among different perforation clusters. The solid mechanics is modeled using Eq. (7). Flow in porous media and fractures are modeled using Eq. (8) and Eq. (9). Fluid distribution from the wellbore into different fractures are modeled using Eq. (10).

$$\nabla \cdot [\mu \nabla u + \mu \nabla u^T + \lambda tr(\nabla u) + \sigma_0 + \alpha p I] = 0 \tag{7}$$

$$\frac{\partial p}{\partial t} = \nabla \cdot \left(\frac{kM}{\mu} \nabla p \right) - \alpha M \frac{\partial}{\partial t} (\nabla \cdot u) \tag{8}$$

$$c_f \frac{\partial p_f}{\partial t} + \frac{1}{w} \frac{\partial w}{\partial t} = \nabla \cdot \left(\frac{w^2}{12 \mu_f} \nabla p_f \right) \tag{9}$$

$$p_w - \Delta p_{section} - \Delta p_{perf} = p_f \tag{10}$$

In the above equations, u is the displacement, p, p_f, p_w are the pressures in the porous media, fracture, and wellbore, μ and λ are the Lame constants, σ_0 is the in-situ stress, k is the matrix permeability, μ and μ_f are the viscosities for the reservoir and fracturing fluids, α is the Biot coefficient, M is the Biot modulus, c_f is the fluid compressibility, w is the fracture width, $\Delta p_{section}$ and Δp_{perf} are the wellbore friction pressure drop and perforation pressure drop, V_w is the wellbore volume.

Pressure change in the sealed monitor wellbore is calculated at every timestep using fluid compressibility relationships seen in Eq. (11). For the monitoring wellbore, pressure change in the monitor wellbore is induced by the wellbore volume change as the fracture approaches and crosses and deforms the wellbore. So, the wellbore pressure change dp_w can be calculated from the wellbore volume change V_w.

$$c_f = -\frac{1}{V_w}\frac{dV_w}{dp_w} \tag{11}$$

As the fracture propagates, the strain tensor in the individual wellbore cells can be tracked and displayed relative to time. As can be seen from Figure 41, the resulting strain is negative, indicating compression, due to contraction in the wellbore at that position. Note the order of magnitude of strain is 35 microstrains. As the fracture from the treating well propagates toward the monitor well, the strain changes predictably. The fracture tip tensile opening makes the strain along the wellbore less compressive. The strain continues to become more tensile as the fracture approaches the monitor well, until the fracture intersects the wellbore, after which the strain becomes compressive. In these simulations the wellbore and formation are assume to have perfect cohesion. The inclusion of the cement sheath was investigated but it was observed a minor effect due to the fact the modulus of cement is very close to that of the formation, while the modulus of

the steel is much larger, the effect of the cement was negligible, and numerical optimization was a driving factor.

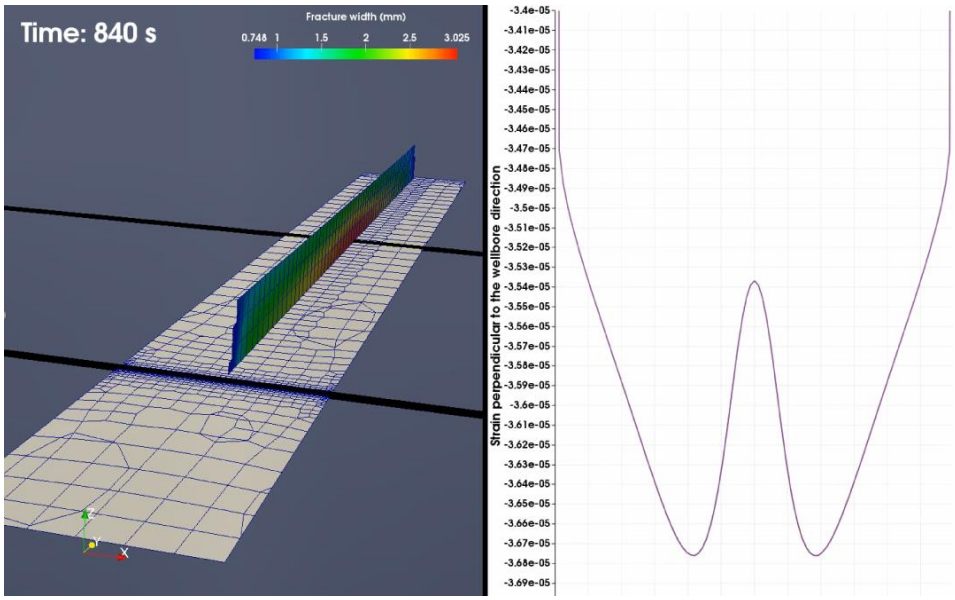

Figure 41: Single fracture example propagating towards the monitor with resulting strain perpendicular to the wellbore (Zheng, 2020)

Investigating the expected strain in the formation (rather than only in the casing) is also extremely helpful. Figure 42 displays a combined strain plot. Per convention, positive strains are tensile, and negative strains are compressive. The strain history displayed by the shaded regions indicates the range of strain responses observed over the extracted line. The span of the color bar represents the variability in strain recoded along the wellbore. In these figures epsilon_0 refers to ε_{11} or ε_{xx} in the direction along the wellbore, epsilon_3 refers to ε_{22} or ε_{yy} perpendicular to the wellbore, and epsilon magnitude is the magnitude of the full tensor for strain. The strain along the wellbore path is a proxy for the strain that would have been observed very close to a cased wellbore or on fiberoptic cross-well strain responses.

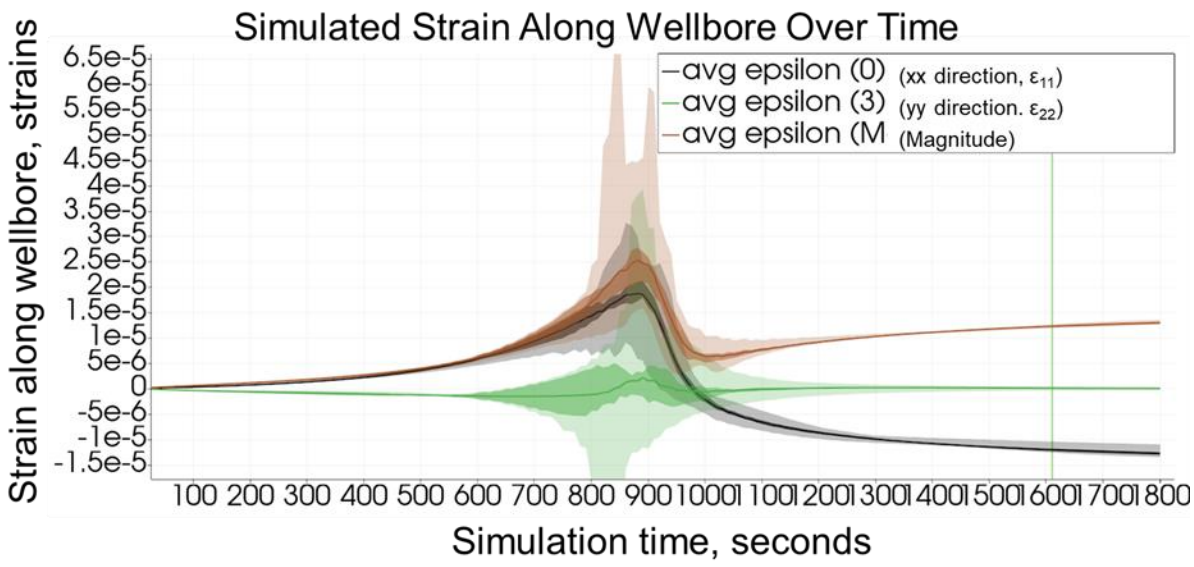

Figure 42: Simulated Strain in the formation along the wellbore path in various orientations

The shift from tension to compression as the fracture intersects and passes the well location is evident in Figure 43. The property displayed is the strain in the x direction along the well. As can be seen on the right, after the tension in the x direction is at a maximum, the strain becomes compressive as the fracture passes and extends past this monitoring location. The magnitude of this observed strain is on the order of 20-25 microstrains, with a peak strain reading at 32 microstrains when the fracture intersects the wellbore.

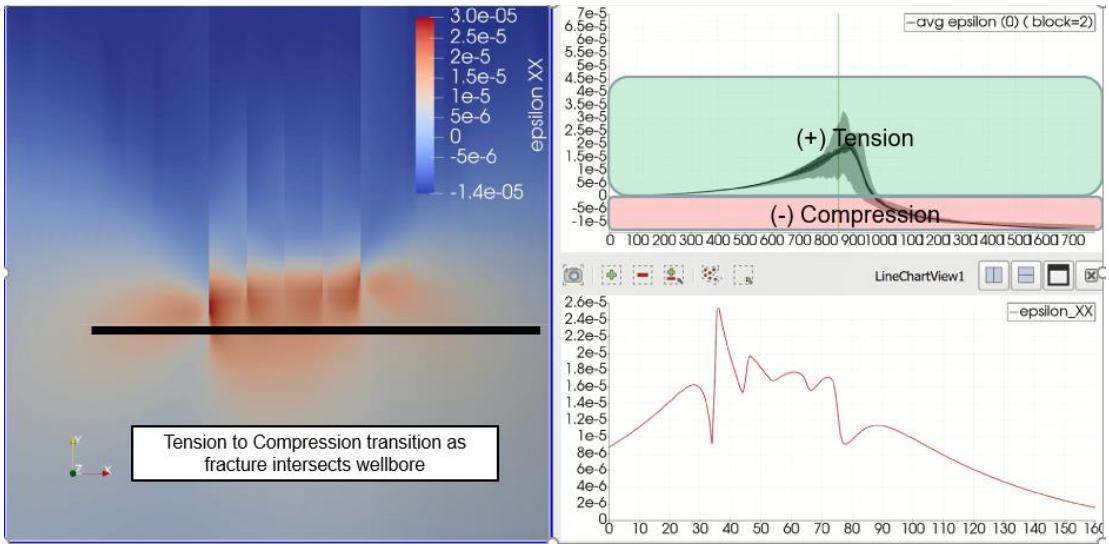

Figure 43: Strain in the XX direction in the reservoir, along the wellbore direction

Displacements are also a key component to understand wellbore strain measurements, since the physical movement in the formation coupled with the fracture interaction is what is actually deforming the casing. Figure 44 shows the simulated formation displacement ahead of the fracture. For this case, negative displacements in the Y direction represent a tension pulling or relaxing the compressive stresses in front of the propagating fracture. The magnitude of this displacement is estimated to be on the order of 0.2 - 0.3mm.

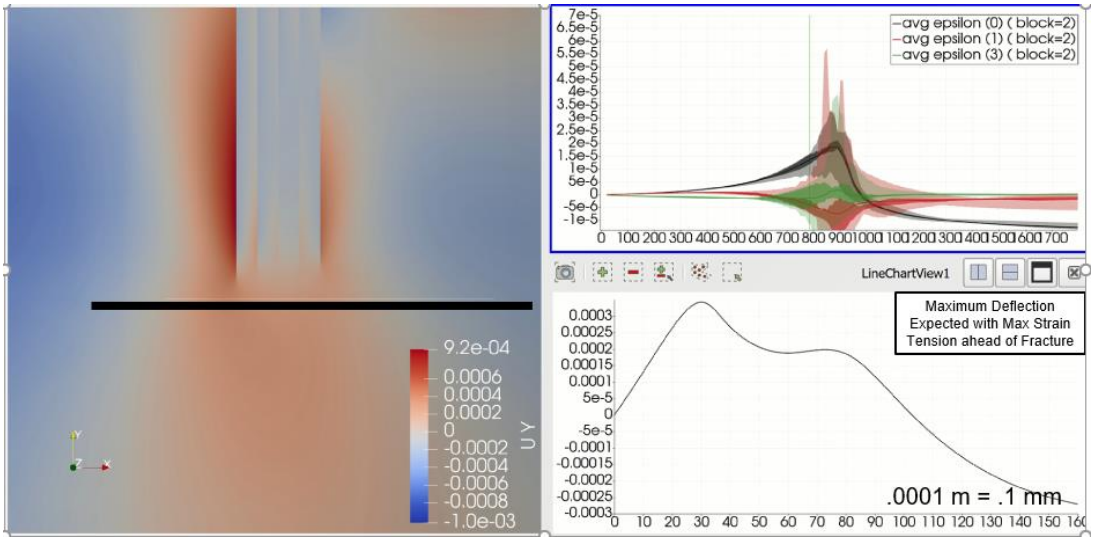

Figure 44: Displacement in the YY direction during fracture propagation

Finally, a useful extension of the modeling capabilities is to develop a waterfall plot, since this is the most common type of plot for cross-well strain measurements using fiberoptic cables. Figure 45 displays the extracted strain in the x direction along the wellbore path. It is common to see the tension front leading the fracture on many cross-well fiber projects (Ugueto et. al. 2023, Haffener et. al. 2022, Brinkley et. al. 2021). Capturing this behavior will allow easier crossover from physically measured wellbore strain to fiberoptic relative strain rate. Ugueto et al. (2023) and Shahri et al. (2021) also display this effect of the fracture tensile tip and resulting strain field, and have validated this observation in various industry simulators.

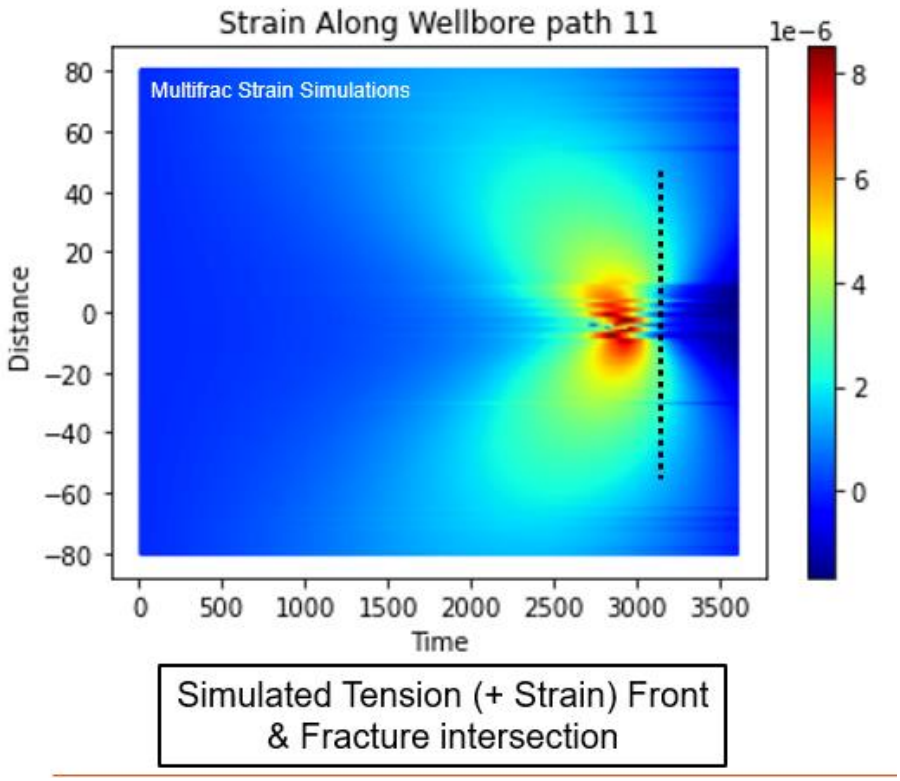

Figure 45: Extracted XX strain in time along the wellbore path, sampled from the MultiFrac-3D files, displayed in the waterfall style typical for fiberoptic monitoring projects.

4.6 COMPUTING EXPECTED SURFACE PRESSURE RESPONSE ON SEALED WELLBORE NUMERICALLY

Wellbore gridding is extremely important in order to capture the miniscule deformations present in the subsurface while monitoring sealed wellbore pressure. These simulations link the fracture propagation, the resulting deformation in the formation induced by the fracture width, the resulting volume change on the casing due to deformation, and the subsequent increase in pressure due to the volume reduction from fracture intersection. For this process to be accurate, a highly refined mesh is required and the monitor wellbore must be explicitly modeled. Figure 46 displays a slice of the grid which displays the formation surrounding the wellbore in blue, and the casing mesh in red. Note there are five layers of refinement through the thickness of the steel cylinder.

This level of refinement is carried through all future simulations as it was found to be the best balance between rigorous meshing and numerical efficiency.

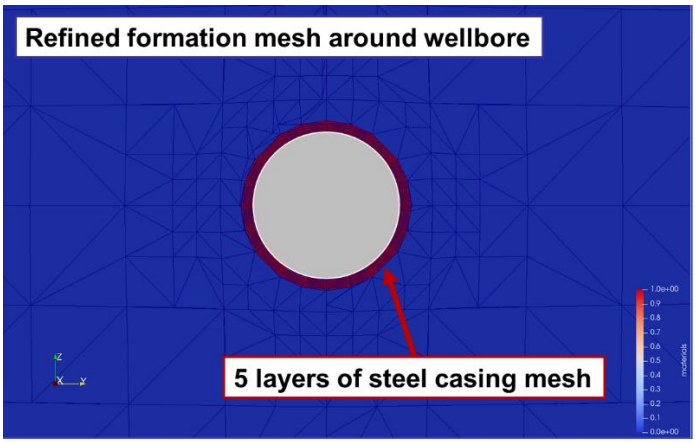

Figure 46: Refined meshing around the wellbore. Blue is formation, red is the steel casing. Note the many layers of refinement in the casing to capture the subtle deformations accurately.

Figure 47 displays the near wellbore region, with an excavation of the mesh since additional refinement is very detailed near the wellbore and gets more coarse with additional distance from the monitor well. The monitor wellbore can be seen in red at the center of the meshing.

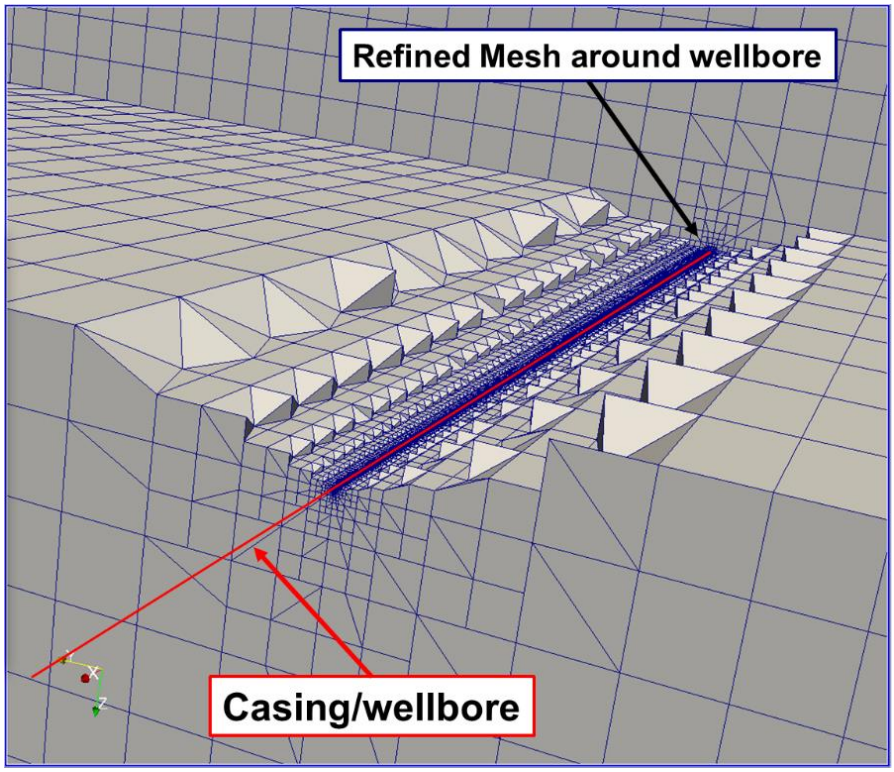

Figure 47: 3D visualization of the wellbore and formation meshing displays a breakaway view at each level of refinement.

4.7 PARAMETRIC STUDY OF COMPLETION, FORMATION AND WELLBORE VARIABLES

A standard case was generated for a pair of wells 200 m apart on plane (Figure 48). The parametric study focuses on several variables that have a first order impact on the resulting pressure response. The parameters investigated for this study were lateral length, leak-off coefficients, pump rates, Young's Modulus, and wellbore fluid compressibility.

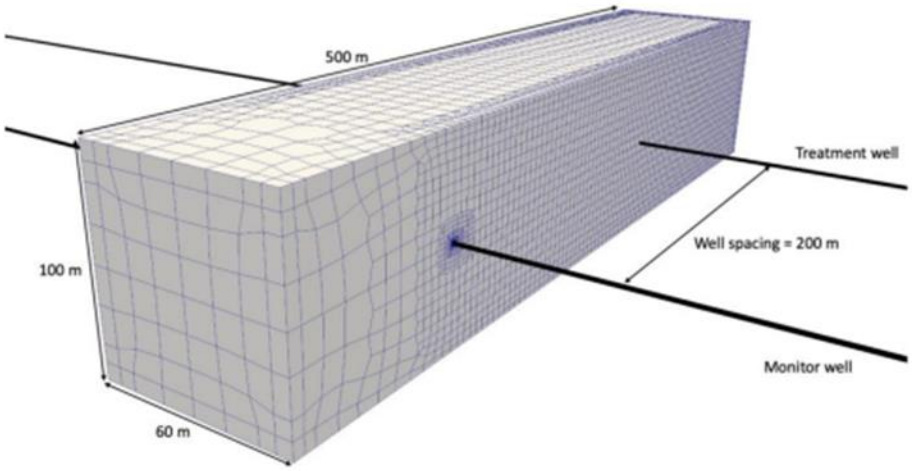

Figure 48: Wellbore setup for parametric sensitivity

The effect of lateral length can be seen in Figure 49, where three different lengths of lateral were simulated. The pumping time is 900 seconds with a 900 second leakoff time, yielding 1,800 seconds of simulation time. From Figure 49, the fracture intersects the wellbore at approximately 500 seconds. Sometime before that, the wellbore senses a low magnitude strain due to the tensile front ahead of the fracture. During fracture intersection and the remainder of pumping (500 to 900 seconds), the sealed wellbore response continues to increase as more strain is induced on the wellbore. The volumes for the 4.5" casing test for 5,000 ft, 10,000 ft, and 15,000 ft laterals were 298.5, 398.5, and 497.6 bbls respectively. Each case has a vertical TVD of 10,000 ft. The smallest casing volume yields the largest pressure response given the exact same fracture intersection and wellbore deformation. The change in the magnitude of the expected pressure response from a 5,000 ft lateral to a 10,000 ft lateral is reduced by approximately 25%.

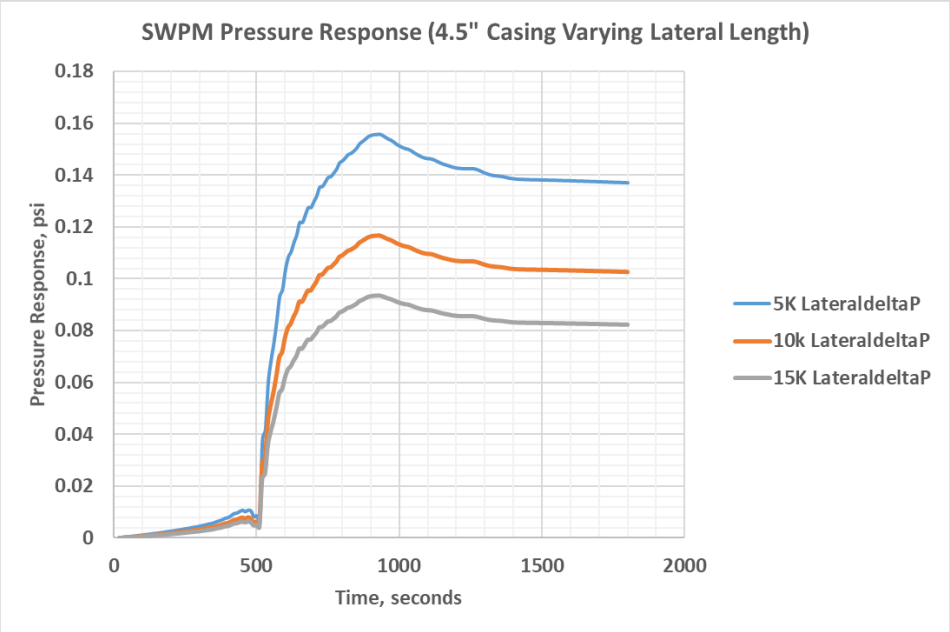

Figure 49: Simulated SWPM response vs varying casing lateral Length

Surface pressure is a major operational variable for sealed wellbore projects. Different operations require holding surface pressure of varying magnitudes; historically the values have some basic recommendation, but no firm technical basis. To date, backpressure on the sealed wellbore has ranged from 0 to 3,000 psi with the most common being 1,500 psi. This has largely been driven by trial and error, holding backpressure was originally designed to mitigate the impact of any gas in the system, but there is an opportunity to optimize the amount of backpressure in order to improve response quality. Analytical modeling suggests that increased backpressure inside the wellbore will yield slightly larger SWPM responses, and thus potentially yield some additional value by enhancing the sensitivity of the measurements.

The impact of leakoff on the simulated sealed wellbore response, is displayed in Figure 50. Multiple leakoff coefficient values were investigated to understand the impact to fracture growth

rate and relaxation. The pumping time for these cases was 3600 seconds, and all other reservoir and fracture parameters were the same. The lower leakoff value (1e-6 m/$s^{\frac{1}{2}}$) is displayed in blue and indicates an earlier fracture arrival, larger magnitude signature and a reduced pressure decline rate after fracturing. Due to the lower leakoff value, there is more fluid volume to generate a fracture, and thus the fracture growth rate is faster, and there is a larger net pressure, and more total deformation/displacement. Upon relaxation, the leakoff is slower, thus the strain reduction on the casing is lower, and the resulting pressure decline is reduced. The higher leakoff case (CL= 1e-5 m/$s^{\frac{1}{2}}$) shows a delayed arrival, a lower magnitude response, and more aggressive pressure falloff signature. This concept is key to the coupled nature of these new simulations; the formation and fracture properties not only alter the fracture growth and geometry, but also alter the resulting strain on and volumetric compression and relaxation of the casing.

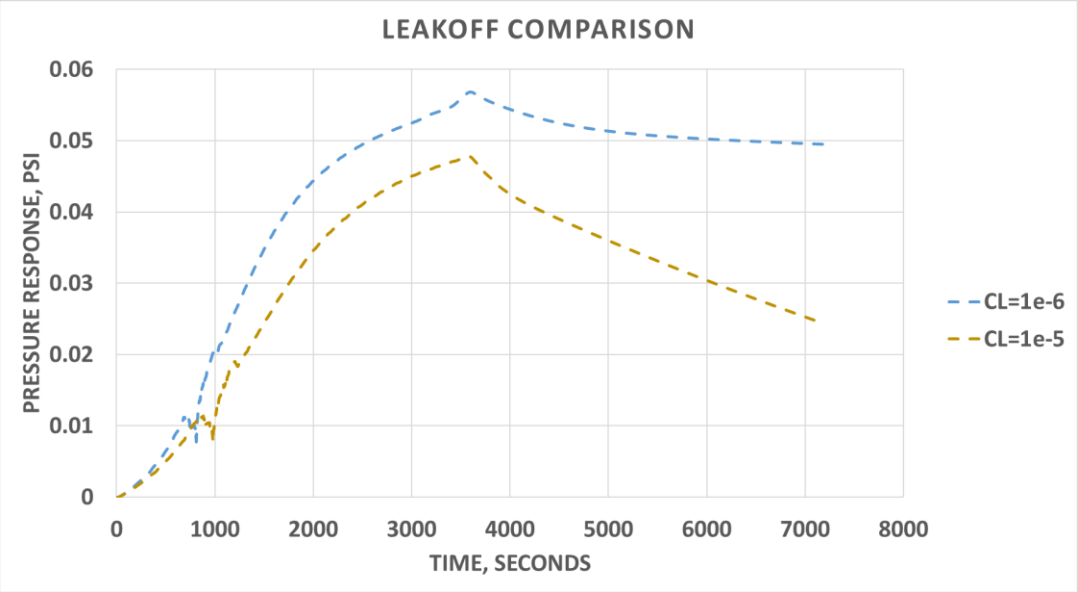

Figure 50: Leakoff comparison for a case of 3600 pumping seconds, with two leak-off coefficients (1e-6, and 1e-5 m/$s^{\frac{1}{2}}$)

Pump rate in a fracture is related to not only the fracture growth rate, but also net pressure, and width of the propagating fracture. This sensitivity clearly shows the results of varying pump

rate over a wide range of typical modern completion design rates on a per cluster basis. Figure 51 displays the effect of pump rate where the fastest pump rate induces the earliest inflection and intersection on the monitor wellbore, while the slower rate is the latest inflection. Additionally, since the pump rate relates to the pressure, width, and total displacement of a fracture, we note the variability in magnitude of the response. This insight shows the importance of quantifying volumes to first response (VFR) and event magnitudes. Furthermore, the slope of the inflection relates to the fracture velocity; the faster the fracture passes the monitor well, the greater the slope of the pressure change. This variability in slope of the arrival is evident in the field data, and it suggests that the arrival time, combined with the slope of the inflection, can be a useful diagnostic to estimate a distributed rate to the leading fracture.

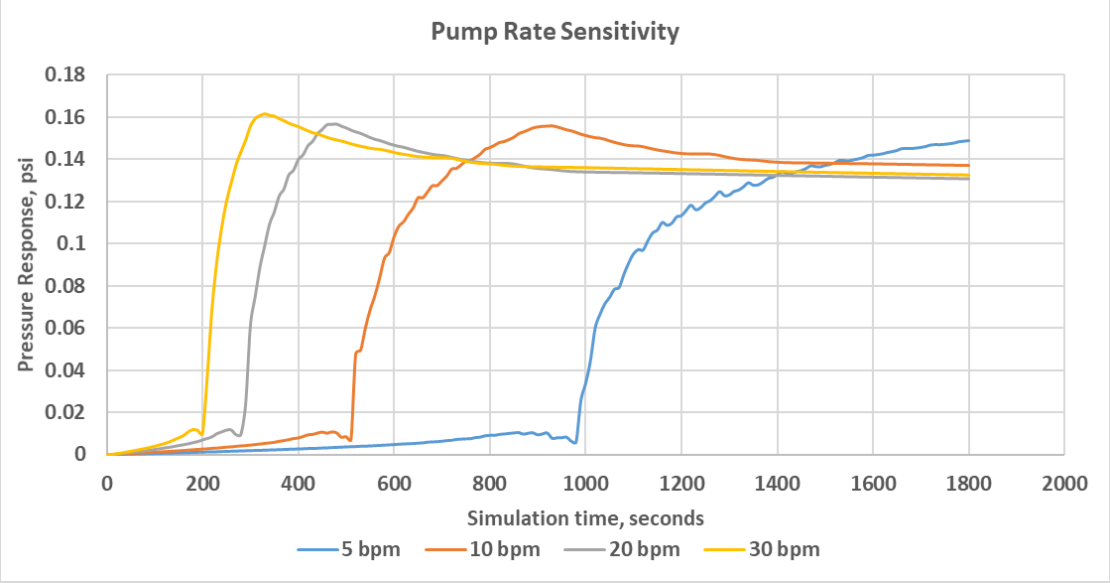

Figure 51: Sensitivity on pump rate to SWPM response

The stiffness of the rock in which a fracture is propagating clearly alters the fracture width and distribution of fluid and pressure. Characteristically higher Young's Modulus rock yields

thinner fractures with small apertures and earlier arrivals, while low modulus rock tends to have wider fractures and later arrivals. This insight can be seen in Figure 52, which displays the effect of a system's Young's Modulus on the sealed wellbore pressure response. Additionally, with wider fractures, more total displacement is expected, and thus additional strain imposed on this coupled wellbore system. The lowest modulus rock is expected to yield larger magnitudes in pressure response, while the highest modulus rock (less displacement) will yield the lowest response. These simulations were performed on heterogeneous formation layers, with actual data it would be expected Young's Modulus, and Poisson's ratio could be varying as well as bedding layers could be shifting, and those effects could be taken into account on the SWPM response and growth rate.

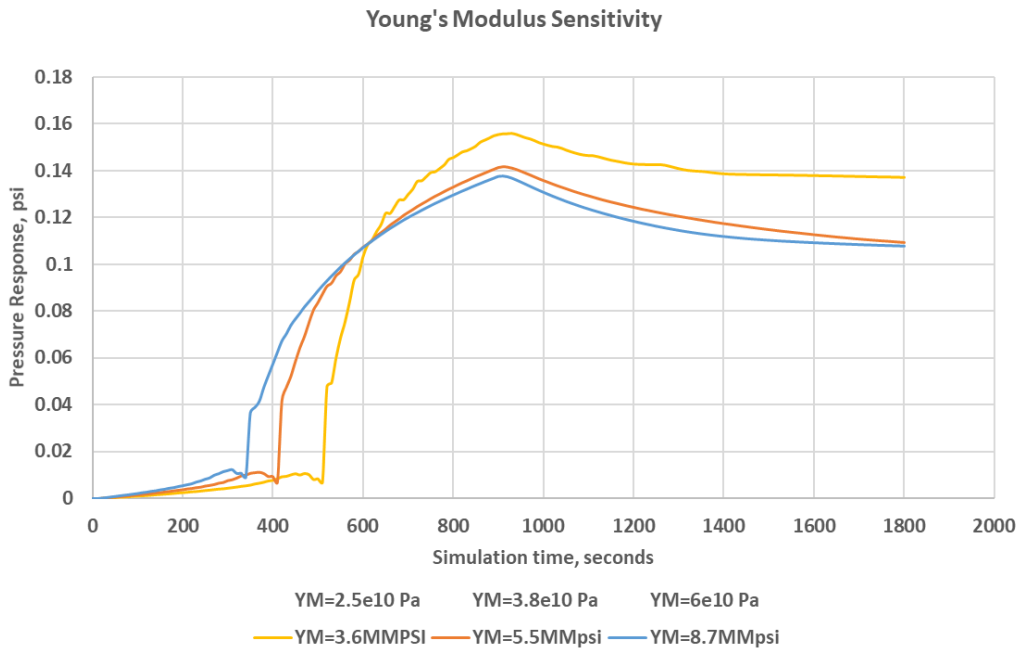

Figure 52: Sensitivity to Young's Modulus

Compressibility, as typically affected by the water salinity in the wellbore, is also seen to alter the expected pressure responses. Utilizing the correlation presented in Equation 6, we can

estimate the expected wellbore fluid compressibility under a wide variety of conditions. Figure 53 displays the pressure response given various wellbore fluids with different salinities at 180 deg F. The plot displays fresh water (0 ppm) up to 100,000 ppm brine fluid. While the magnitudes are small for this example, the variation in pressure response can be 20% due to assumed compressibility.

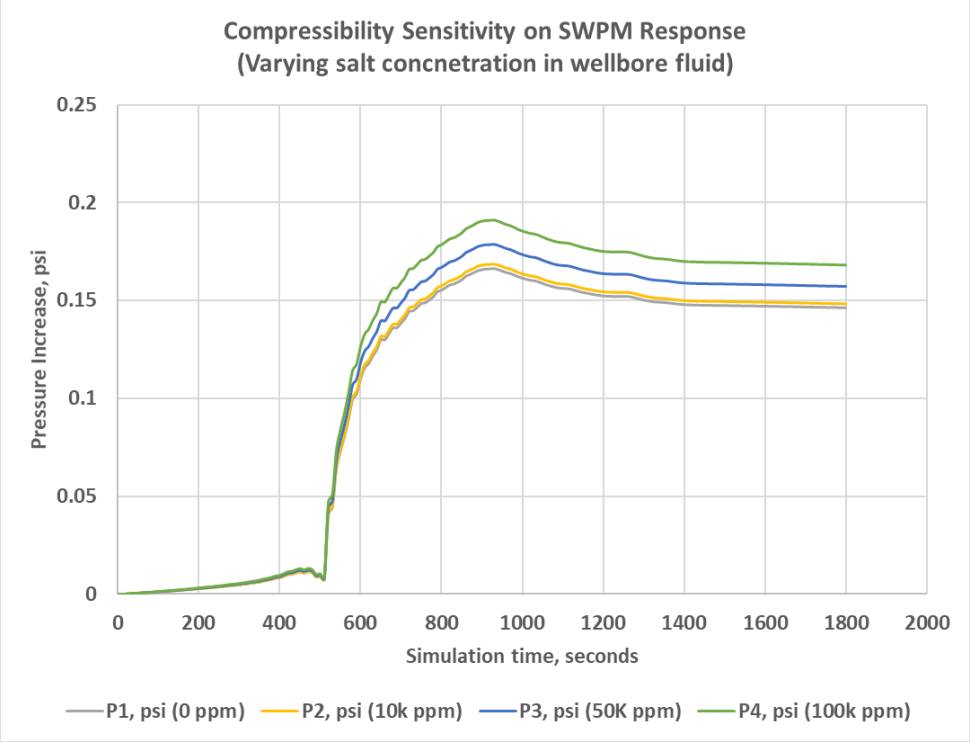

Figure 53: Compressibility sensitivity for brines at 0ppm, 10kppm, 50kppm, and 100k ppm

Often in complex field development with multi-bench landings, fractures can pass near or around other wells but not intersect them. A fracture passing under wellbore is an interesting phenomenon as the presence of a fracture still induces a distinct volumetric change in the system, even near (but not intersecting) a monitor well. Figure 54 displays the simulation domain with a waterfall plot of strain and the expected difference in sealed well responses. The case where a fracture passes by a monitor is shown to induce strain and a very low magnitude SWPM response,

with an absence of a distinct inflection, indicating a fracture arrival. This is also observed in industry case studies from a fiber optic strain catalogue Ugueto et al. 2023, and from cross well fiber strain observations, Shahri et al. 2021.

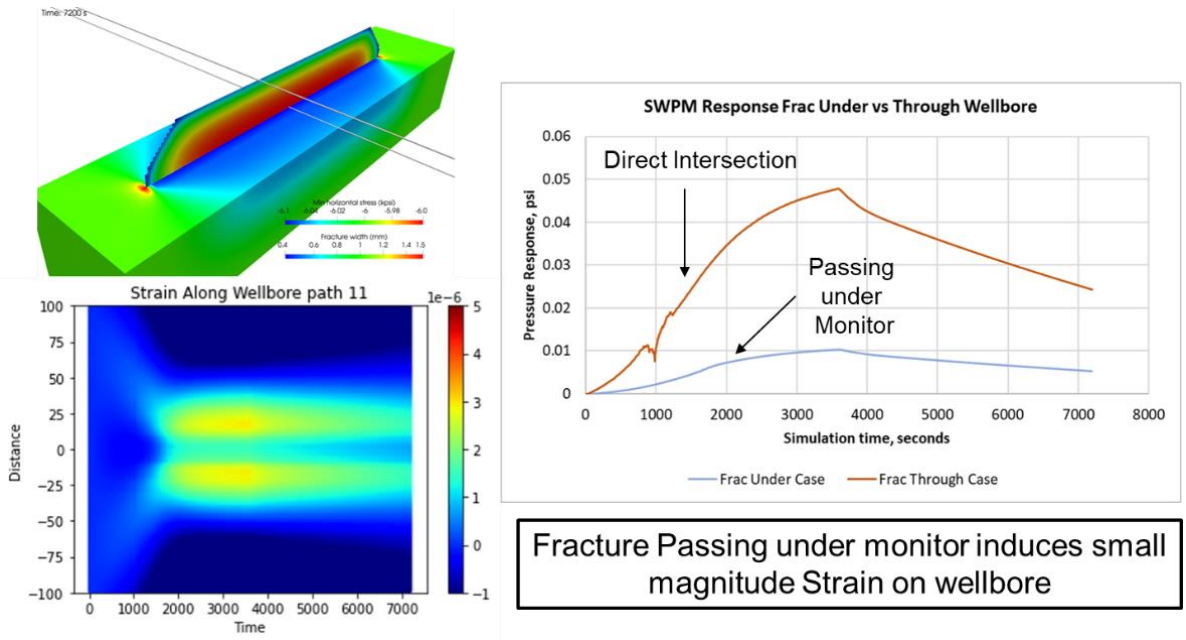

Figure 54: Display of fracture passing under monitor well. Top left is simulation domain with active and monitor wellbores. Lower left is a waterfall plot of observed stain in the monitor wellbore. Right displays the change in pressure.

4.8 FIELD DATA ANALYSIS AND INTERPRETATION

The field data for the study in this section originated from a large diagnostic project in the Meramec formation in the Anadarko Basin. The Meramec is commonly characterized as a tight oil play composed of a siliciclastic system with a range of argillaceous to calcareous siltstone, where the primary driver for reservoir quality is percentage of calcite cement within individual facies (Price, 2017).

The key data elements of the project were fiber-optic cross-well strain, internal and external pressure gauges, microseismic monitoring, tracers, and downhole cameras. Fracturing operations

were conducted around the monitoring wellbores with various pre-planned perforating and stage designs. For this study, the focus will be on history matching the SWPM and the cross-well strain signatures for several key stages. Figure 55 displays a gun barrel view of the laterals of interest and the wellbore distances relative to the monitor wellbore. The 7H monitor well is labeled in red.

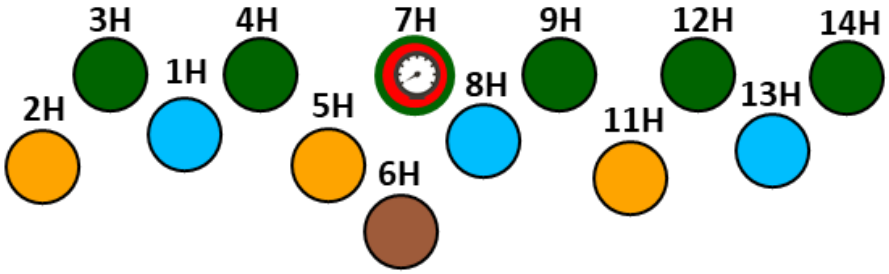

Summary of Well Positions	6H	5H	8H	4H	9H
Average Horizontal Distance from 7H	-14'	-380'	354'	-782'	623'
Average Vertical Distance from 7H	573'	228'	114'	-4'	23'
Average Total Distance from 7H	573'	443'	372'	782'	623'

Figure 55 Gun barrel diagram of project area, with table denoting relative vertical and horizontal distances from the monitor well. Note the 7H is the instrumented well with fiber optics and internal pressure gauges.

Formation characteristics for this case study are reported in Table 7.

Table 7: Summary of Reservoir Properties for Field Case

BASE CASE RESERVOIR PROPERTIES				
FORMATION				
	SI VALUE	**UNIT**	**FIELD VALUE**	**UNIT**
Porosity	0.05		0.05	
cf	2.00E-10	1/Pa		
perm	2.00E-18	m^2	0.00203	md
P0	3.86E+07	Pa	5600.00	psi
Stotal	4.14E+07	Pa	6000.00	psi
biot	0.70			
Tres	394.00	degK	250	degF
density	2.65E+03	g/	2.65	g/cm^3
YM	3.80E+10	Pa	5.51	MMpsi
PR	0.21			
leakoff	1.00E-06			
CASING				
Porosity	0.0010		0.001	
cf	2.00E-10	1/Pa		
perm	2.00E-30	m^2	2.03E-18	md
P0	3.86E+07	Pa	5600.00	psi
density	7788.7	kg/m^3	7.7887	g/cm^3
YM	2.10E+11	Pa	30.46	psi
PR	0.27			

Single Fracture diagnostic test stage

A single fracture diagnostic stage was pumped with a reduced rate and volume to emulate and measure how a single fracture propagates in the subsurface. The fracture propagates from the 5H wellbore and intersects the 7H monitor wellbore. As can be seen in Figure 56, the single cluster stage is on the left side of the plot with an average treating rate of 30 BPM for a designed treatment volume of 1,800 bbls and 80,000 lbs of sand. The arrival based on the SWPM inflection occurs approximately 30 minutes into the treatment (roughly half of the planned pump time for the diagnostic stage).

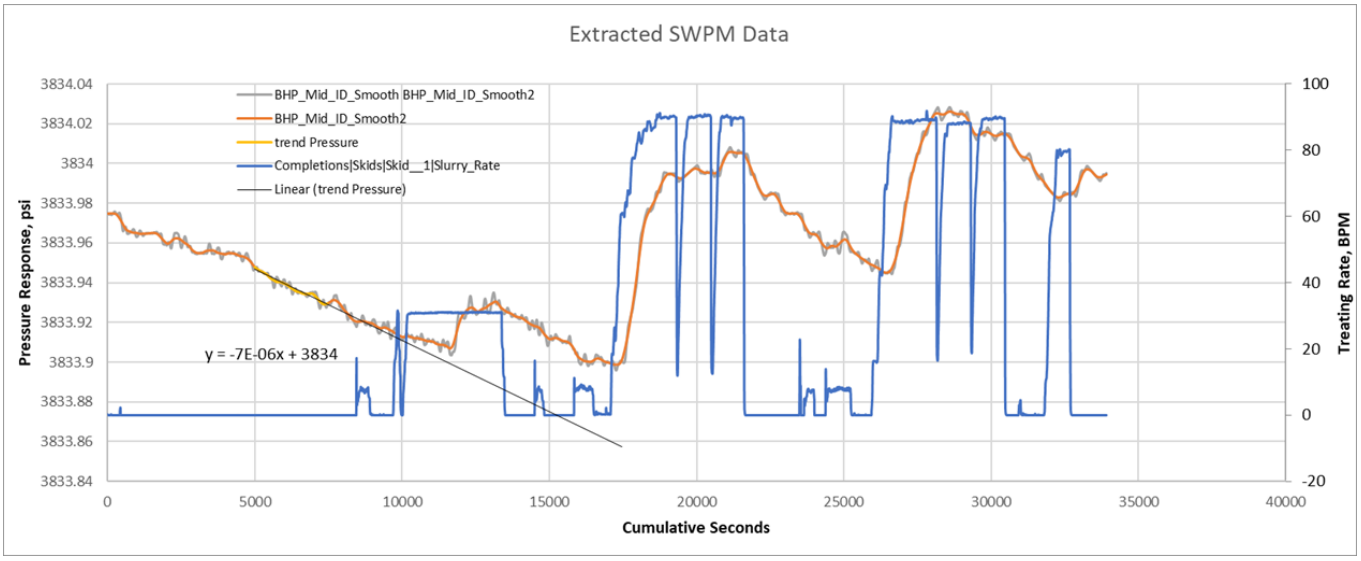

Figure 56: Treatment rate data (blue) and SWPM data (orange)

The corresponding strain response for the single fracture arrival can be seen in Figure 57, which depicts a fiberoptic strain waterfall plot. In Figure 57, the coloring on the strain plot represents the measured slow strain rate, where red denotes tension or extension strain and where blue denotes a compression along the fiber cable. The strain response along the measured depth of the monitor well versus time is displayed. The fracture arrival can be immediately identified by the characteristic compression-tension-compression signature (blue-red-blue), and the tension front leading the fracture tip can be seen clearly. This is typically observed as a plume or tensile response before the fracture arrives (Ugueto et al. 2019). After pumping stops, there is a clear reversal of polarity in the strain signature, with a corresponding reduction in the SWPM pressure curve, indicating a relaxing of the fracture with a reduction of net pressure and the start of fracture closure due to leakoff.

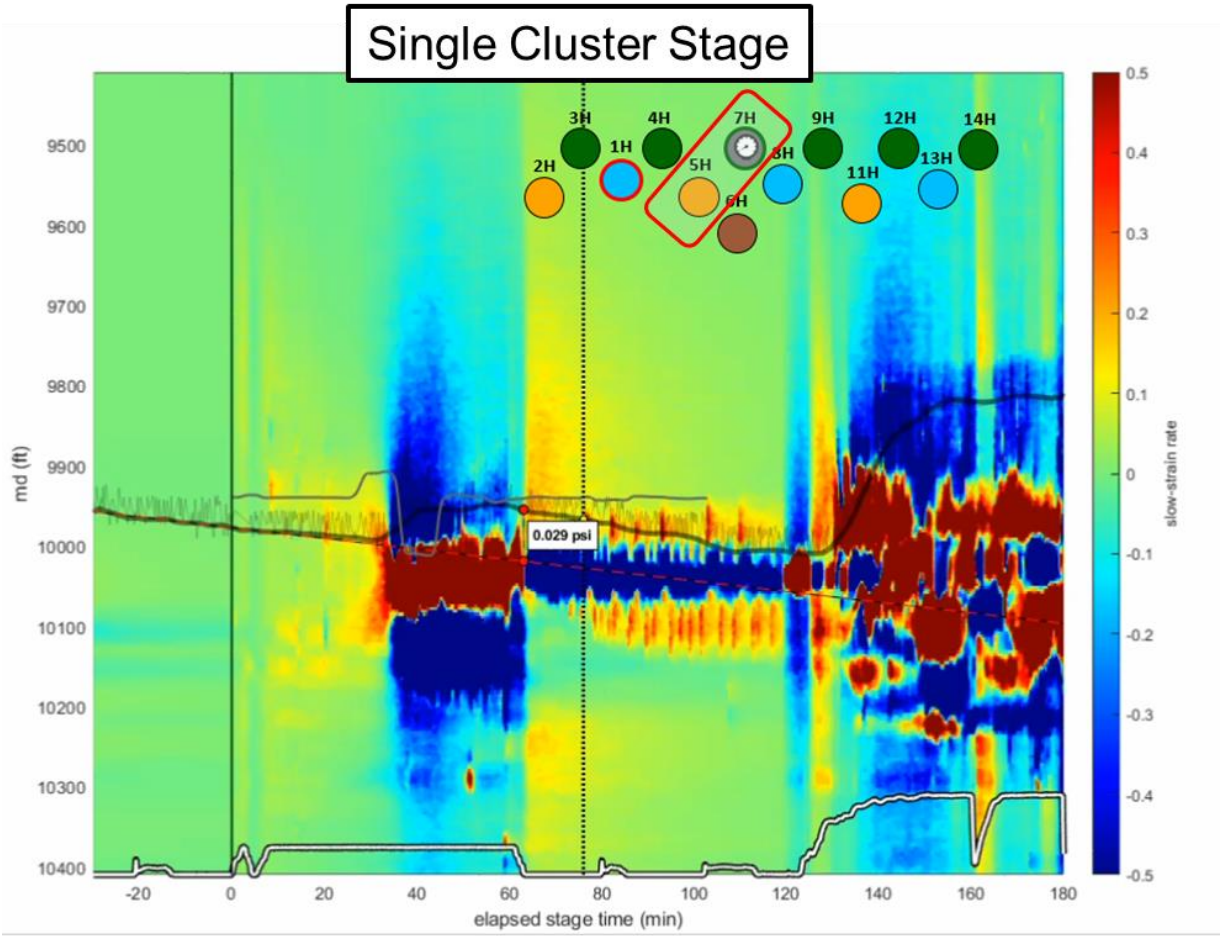

Figure 57: Single cluster fiber-cross-well-strain response with SWPM superimposed.

Building this single fracture case in the simulator, the wellbore orientation mimics the true wellbore positions relative to each other, and the monitor wellbore has a highly refined mesh around it, with the casing being simulated as a hollow steel cylinder (Figure 58). As the fracture propagates toward the monitor well, deformations at every time step are recorded, and a total volume change is computed. From this volume change the expected pressure response is computed using the compressibility relationship (Equation 6).

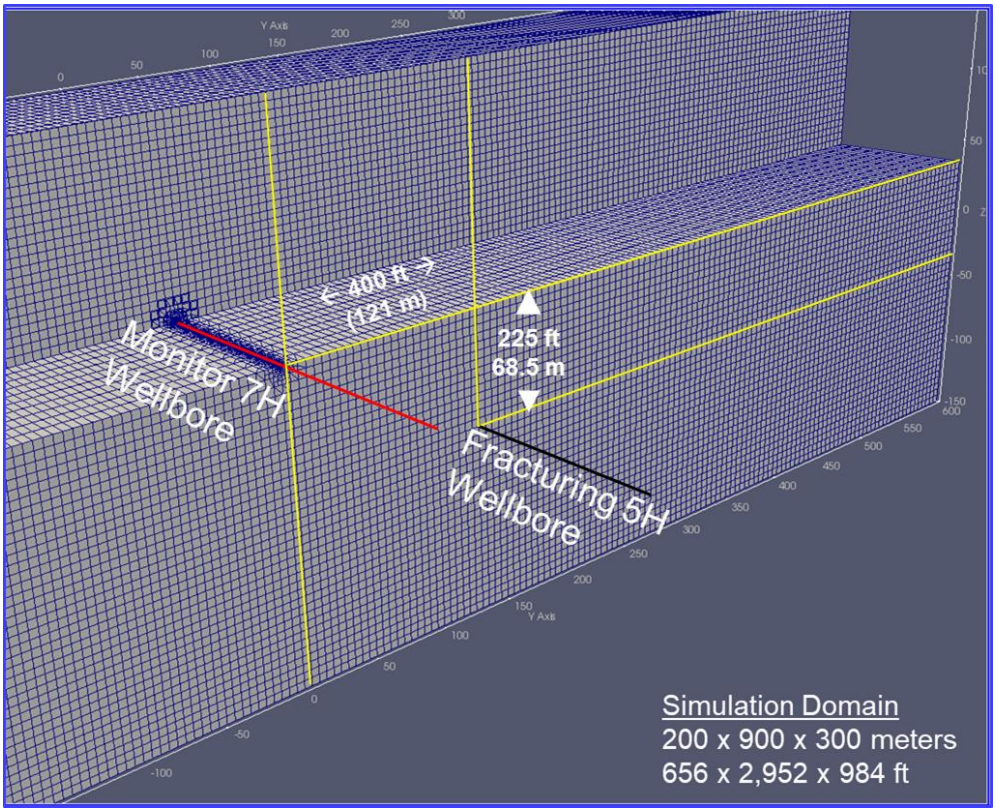

Figure 58: Simulation domain for history match case. Fracturing from the 5H wellbore toward the 7H monitor wellbore. Wells are spaced approximately 400 ft laterally, and 225 ft vertically.

One of the challenges in the field history match is to honor the fracture arrival using both time and volume-based methods. While the fracture arrival can be slowed down by altering the system permeability or leak-off parameters, this greatly alters the post-frac falloff signature, which is the strain reduction observed when the pumps are shut down. Care was taken to consider these systems together, as tightly coupled, and an iterative process was employed to generate the best field history match. The process and results of this match can be seen in Figure 59. One key aspect to note here is the majority of the pressure response occurs when the fracture tip is passing the wellbore, then the subtle rollover occurs when the rate of strain is reduced and the fracture tip is sufficiently past the monitor wellbore. This yields an interpretation that during propagation and when the slope of the pressure response is greatest, the fracture tips are nearest the monitor well

and maximum strain is induced on the wellbore. Once the fracture passes the monitor well, the total rate of strain induced on the wellbore is reduced, and the strain magnitude is much lower. This strain history effect is observed in the simulations through Figure 42 - Figure 44, and present in the field data, through Figure 56 and Figure 59.

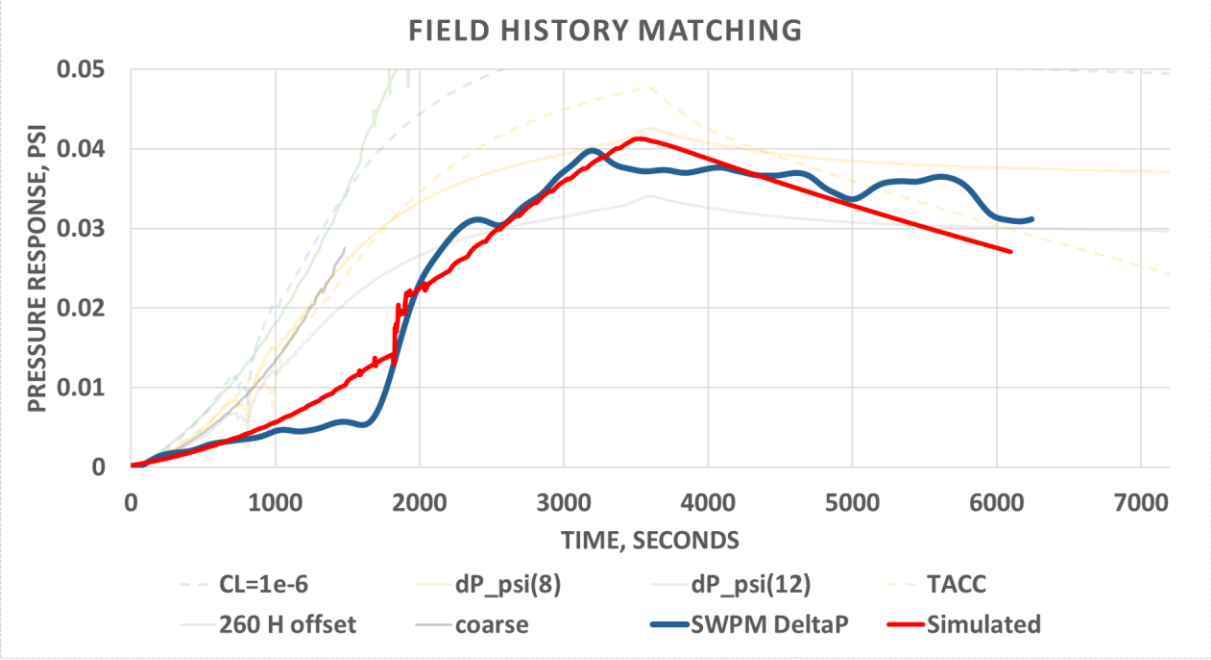

Figure 59: Field data and the history match with simulations (during and after pumping).

Figure 59 was the initial figure published in SPE 209120 by Elliott et al. (2022), but it has since been improved with further refinements in the meshing and geomechanical parameters. The updated figure and final history match is seen in Figure 60 below, with a greatly reduced error.

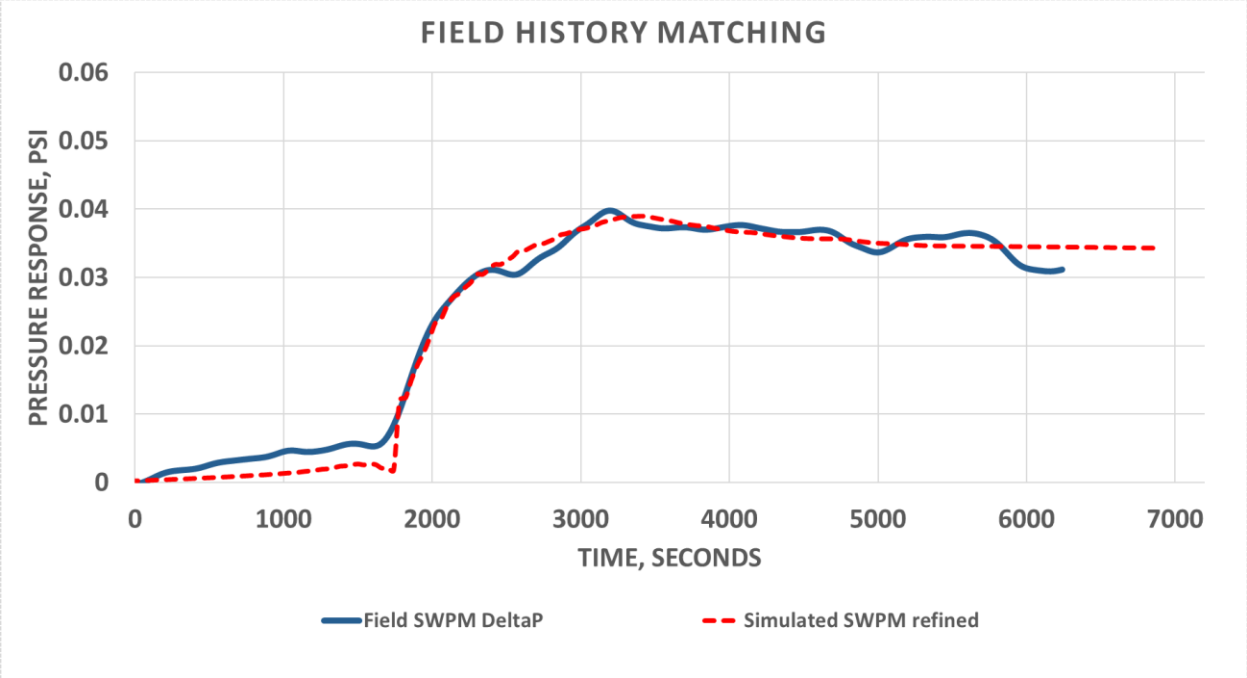

Figure 60: Refined History Match, updated from SPE 209120

Multiple Cluster Stage Discussion

A multi-cluster stage for the 5H well in this sequence, designed as a 5 cluster with 5,500 bbl and 325 klbs proppant is investigated next. Figure 61, displays the previously matched single cluster stage next to the current multi-cluster stage. The time of arrival, and volume to the arrival are greatly accelerated in this case relative to the single cluster stage, and there is also a significant increase in the SWPM signal magnitude (0.201 psi compared to 0.029 psi). The order of magnitude is much more representative of a typical treatment stage response on the sealed well (>80% of the stages reported responses between 0.1 and 0.3 psi). The prevailing thinking for this increased magnitude is the additional propagation of multiple fractures and significantly larger total deformation of the monitor wellbore, over a larger span along the well. This effect could be caused by a variety of factors: increased total number of fracture intersections, increased net pressures, higher pumping rates, faster fracture velocities, larger frac height, and/or more intra-

fracture strain during the stage. Multi-cluster simulations will be a focus on future model capabilities and simulation history matching efforts.

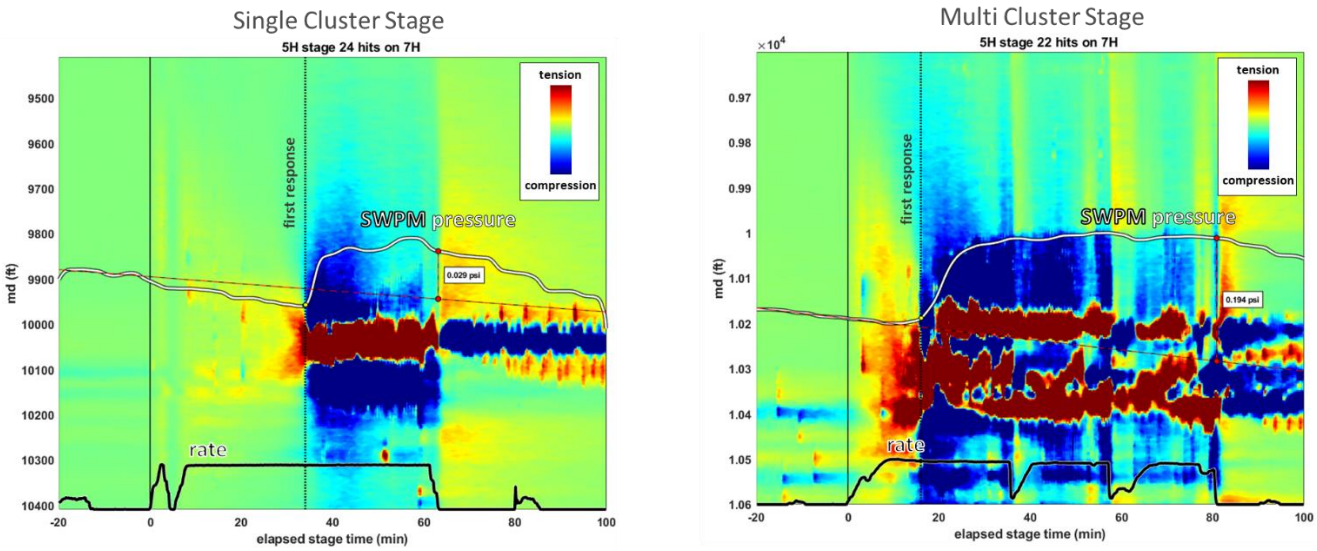

Figure 61: Comparison of single cluster and multi-cluster arrival signatures.

Project Strain and SWPM Relationships

Data interpretation of this project yielded observations of multiple correlative relationships. Figure 62 shows a strong positive relationship between the sealed wellbore pressure response magnitude and the recorded fiber cross well strain span, the summed strain, and the normalized strain/volume pumped. This observation encourages a continued discussion of sealed wellbore response magnitude relative to total volumetric displacement, as additional length (as measured by fiber fracture span) yields additional volumetric displacement, and result in larger SWPM responses. In fact, the two stages with the largest SWPM response were trials of extended 300 ft stages, while most of the base case stages were designed for 150ft stage lengths. The extended stages show distinctly larger influence on the fiber span, summed strain, and SWPM magnitude. The summed strain as it is measured on the cross-well fiber also indicates that total

fiber strain correlates well with the magnitude of the SWPM signature. These insights give further utility to integrated diagnostic projects with fiber and SWPM.

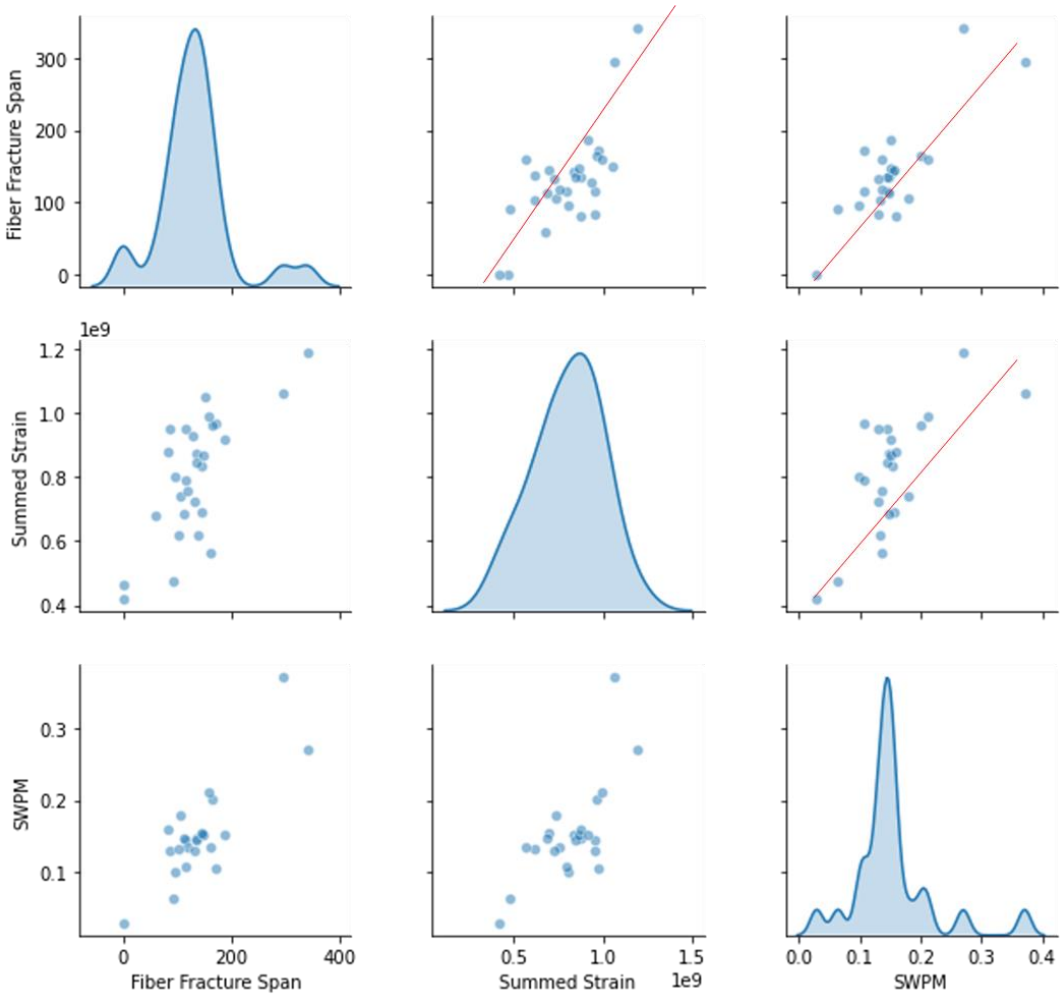

Figure 62: Cross well strain relationship with SWPM response.

By combining the physical measurement of casing deformation and the resulting strain and displacement with the integrated 3D numerical modeling effort, greater insights to the expected downhole behavior of casing were resolved. The laboratory experiments clearly show expected ranges of deformation under applied loading, while the numerical modeling computes the total

deformation and volume reduction of the casing during hydraulic fracture intersection. Field data was interpreted to match a diagnostic single cluster fracture propagation case, and the sealed wellbore pressure history match was successful, both in magnitude and arrival time. This capability unlocks new methods for interpreting diagnostic data like SWPM and fiber optic cross-well strain.

- Laboratory strain measurements on the casing indicate measured circumferential strain is on the order of 0-300 microstrains for deformations of 0-0.75 mm (0-0.03 inches)
- Analytical modeling supports the volumetric deformation theory as the key driver for SWPM responses and pressure can be estimated by simply utilizing compressibility relationships
- Numerical modeling gives greater insight to the complex 3D problem of fracture interaction with wellbores and provides a way to quantitatively invert the data to obtain fracture geometry parameters.

Field history matches of the SWPM response are achievable and yield additional insights to utilize the pressure and strain responses as a diagnostic tool for hydraulic fractures

Chapter 5 Integrating Simple Fracture Models with Wellbore Pressure Measurements for Fracture Diagnostics

5.1 VFR AND GROWTH RATES OF HYDRAULIC FRACTURES

Volume to first response (VFR) is the volume required to be pumped (in the well that is being fractured) until a pressure or strain response is observed at a monitoring well location. This strain response was presented in the previous chapter. VFR can be reliably simulated because the fracture deforming the casing yields a pressure change in the observation well that can be measured easily. The fracture length is known at the time of fracture arrival, therefore, the total volume pumped at that point in time can be projected back and forward in time using known analytical equations.

The growth rate of hydraulic fractures can be described by utilizing the concepts presented in the PKN models Perkins and Kern (1961); Nordgren (1972). Here length of the fracture can be projected as a function of rock properties, fluid viscosity, and injection rate. A general form of fracture length as a function of time can be seen in Equation 1; this is the general form and does not account for leakoff from the fracture face. Later Nordgren (1972) added Carter leakoff to yield Equation 2.

$$L(t) = .524\left(\frac{q^3 E'}{\mu h_f^4}\right)^{\frac{1}{5}} * \ t^{4/5} \tag{1}$$

Accounting for leakoff this equation becomes

$$L(t) = \frac{Q_l}{2\pi C_L H} * t^{1/2} \tag{2}$$

Shaperio et al. (2006) describe growth rate of a hydraulic diffusivity of microseismic events and the resulting shape of the event vs time curve as it relates to diffusivity. A square root of time relationship to the triggering front of hydraulic fracture growth has been displayed extensively

through works from Fischer et al (2008), Shapiro and Dinkse (2009), Jia et al (2019), and for sealed wellbore measurements through Brinkley et. al. (2021), Haffener e.t al. (2022). This equation represents the spatio-temporal distribution of events giving fracture growth as a distance vs time relationship, which follows a similar behavior as the PKN equations above. Shaperio shows this relationship as equation 3. It is important to note that both the PKN leakoff and hydraulic diffusivity show a square root of time relationship.

$$r = \sqrt{4\pi Dt} \sim L(t) = f(\sqrt{t}) \tag{3}$$

$$A_t = \frac{\pi * distance^2}{TFR} \quad and\ thus: r_t = \sqrt{\frac{A_t}{\pi} * t} \tag{4}$$

Here A_t represents the additional surface area of a circular fracture per unit time.

Additional extensions of the growth rate concept can be deployed with making an assumption of area increase per unit volume. Equation 4 represents a radial assumption where height and length increase can attribute to the area increase over time. This assumption would be more appropriate in formations where fracture height is on the order of fracture length. In other cases additional assumptions should be made for constant height fractures, or elliptical shaped fractures. In that case a constant height fracture or elliptical fracture growth rates can be seen in Figure 63 Furthermore the growth rate can be solved explicitly by setting it equal to the PKN length growth prediction (equation 2) and solving for growth rate in terms of the fracturing parameters in the PKN expression. One can resolve that varying geometry assumptions can be seen in these equations displayed in Figure 63, and identify a shape factor where for the radial assumption the factor is (1/4π), the elliptical solution is (1/16π), and rectangular is (1/4π^2).

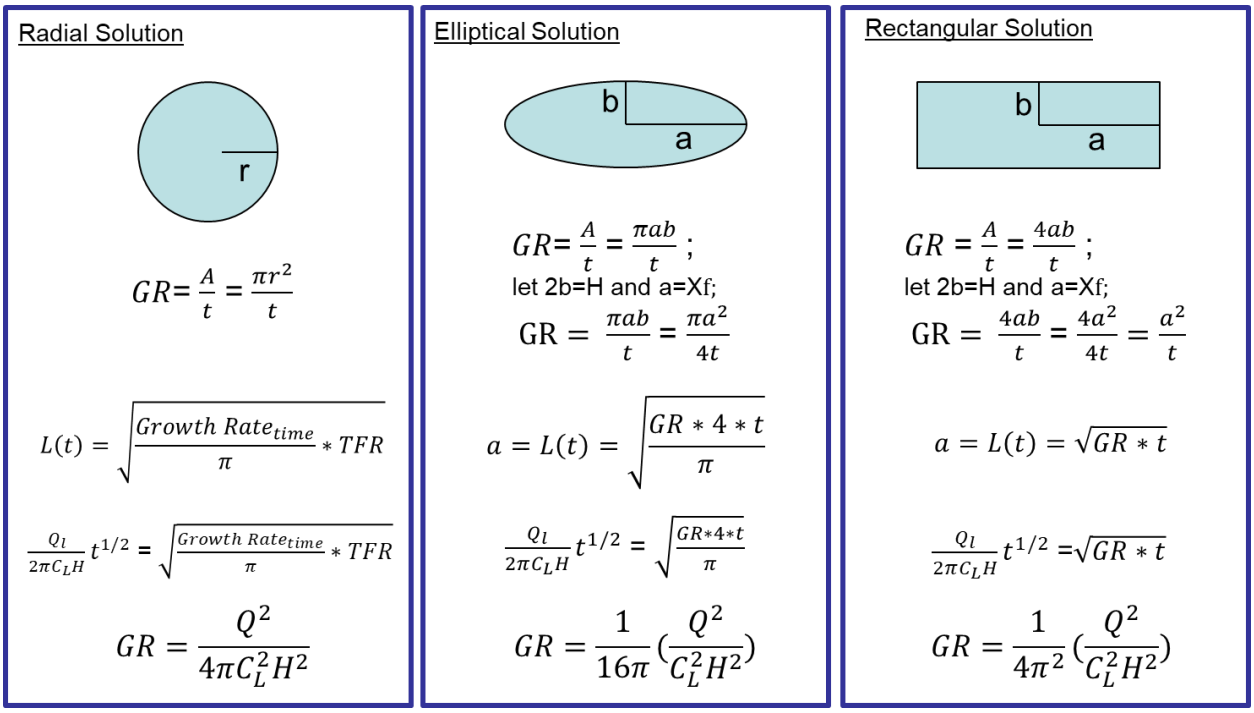

Figure 63: Growth Rate Solutions for various geometry shape assumptions

Under the condition of a constant pump rate, length can be calculated as a function of the square root of volume, following the expression of length as a function of the square root of time. We can further simply the other variable terms in these equations to develop a simple growth-rate based relationship, as can be seen in a time basis (equation 5) and a volume basis (equation 6).

$$L(t) = \sqrt{\frac{Growth\ Rate_{time}}{\pi} * TFR} \tag{5}$$

$$L(v) = \sqrt{\frac{Growth\ Rate_{volume}}{\pi} * VFR} \tag{6}$$

The expression for length as a function of volume is incredibly useful for field cases as various growth rates are observed in actual field datasets. As can be seen in Figure 64, field-based data sets match this behavior well and have been documented extensively. This figure shows the relationship between micro seismic event front as a function of distance and volume pumped in the stage. The maximum distance a fracture can be at any volume is anchored by this observed

square root of time relationship. Brinkley et. al. (2021) also displays the square root of time relationship to half length using the assumption that the leading edge of the hydraulic fracture can be extrapolated between multiple wellbore measurement points in time and space.

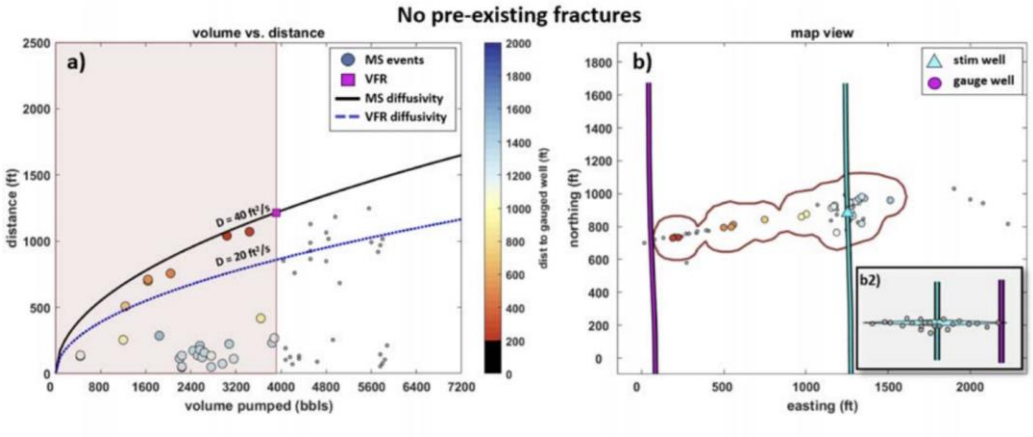

Figure 64: Example diffusive growth rate of the fracture from Haustveit, Elliott et al. (2020)

Figure 65 displays an example of this projected growth of two wellbores, with one being 660 ft from the stimulation well and the other being 880 ft. The first blue star indicates an arrival after pumping for 30 minutes, and the second blue star denotes a second arrival on the more distant wellbore after pumping for one hour. Fitting a PKN style growth rate curve (Equation 2) to these datapoints allows for an extrapolation of the observation and determination of the fracture size at any point in time. Furthermore, understanding this growth pattern and the knowledge that it follows a simple square root of volume pumped, allows the use of this equation to predict realistic fracture geometry, as well as eliminate any outlying responses that do not fit the general trend of fracture growth. For example, any point or arrival that occurs at a great distance too early in the stage would easily be able to be eliminated as a true fracture interaction.

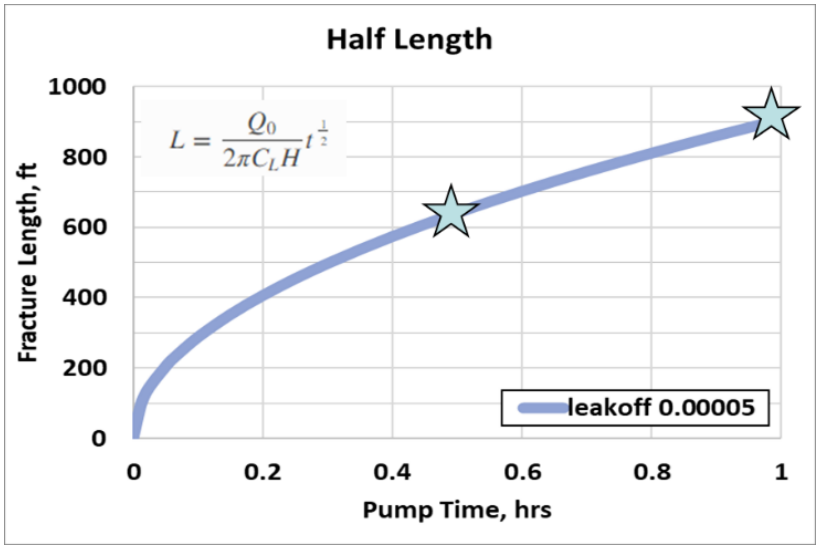

Figure 65: Growth rate schematic of fracture length over time

To further display the utility of the simplistic growth rate based fracture length approximations, several simulations were developed to history match the growth profile. Figure 66 shows the growth rate projected from Equation 6 compared to results form a commercial numerical fracture simulator (Gohfer). As can be seen from the figure, there is close alignment to not only the growth profile but also the final resulting fracture lengths. It is important to note that the growth profile follows the ascribed square root of volume profile, and various stages simulated fall within the distribution of P10/P90 growth rates for this case. This case provides suitable evidence that a measured growth rate form the field can be used as a fracture diagnostic and history matched accordingly.

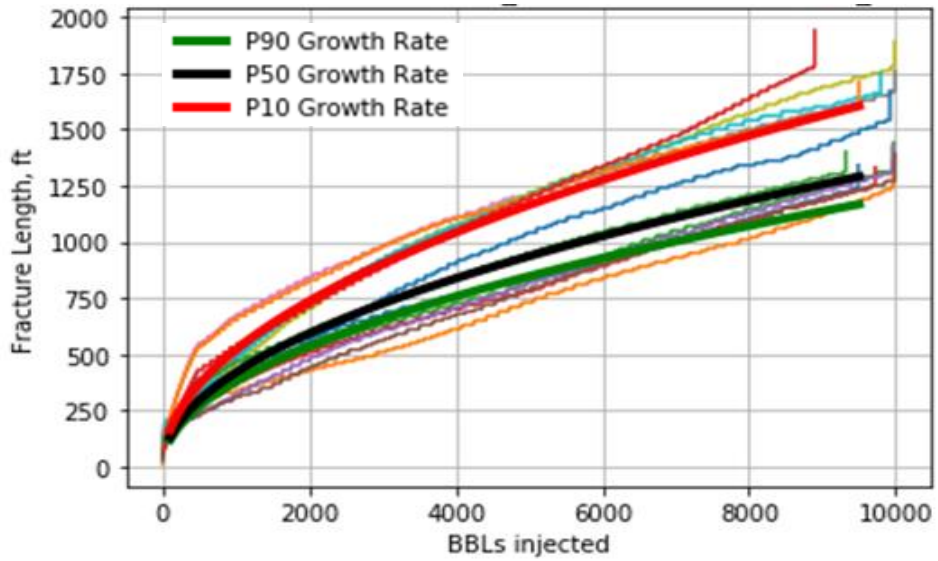

Figure 66: Growth Rate profile comparing numerical simulation via commercial fracturing simulator vs the growth rate extrapolation shown in equation 6

5.2 PARENT WELL DEPLETION EXTRAPOLATION

An additional technique that can be derived from a wellbore pressure response is a depletion region extrapolation. With a few simple assumptions, the fracture geometry can be estimated in time and space given the observance of a fracture driven interaction on a parent well. The distance between two wells and fracture azimuth is generally known, so under the assumption that a new fracture from an infill well propagates in virgin rock, and then eventually enters the depletion region, this intersection distance can be resolved through the methods displayed in this section.

Seth et al. (2020) presented work showing fracture acceleration in depleted rock and variable growth rates in un-depleted virgin reservoir versus reservoir regions with pressure depletion. This concept is displayed in Figure 67, which displays fracture length versus time and the corresponding reservoir geometry at the bottom. The left side demonstrates the effect of well spacing on the fracture arrival and acceleration. As can be seen, the fracture is propagating at a

constant growth rate in the un-depleted formation (red), and as the fracture enters the depletion region at various well spacings, the growth rate increases. The closer the propagating fracture is to the depletion region, the earlier the inflection in growth rate occurs. On the right side of Figure 67, the depletion magnitude and parent well depletion size is varied. With increased depletion size, there are earlier inflections in growth rates. This combination of observations allows for a distance and volume-based extrapolation of the edges of the depleted region. It should be noted that this method has been deployed in low permeability unconventional reservoirs where not much depletion is expected beyond the fracture tips and most drainage of the reservoir occurs between the primary well fractures, thus allowing a depletion boundary to be estimated using this method.

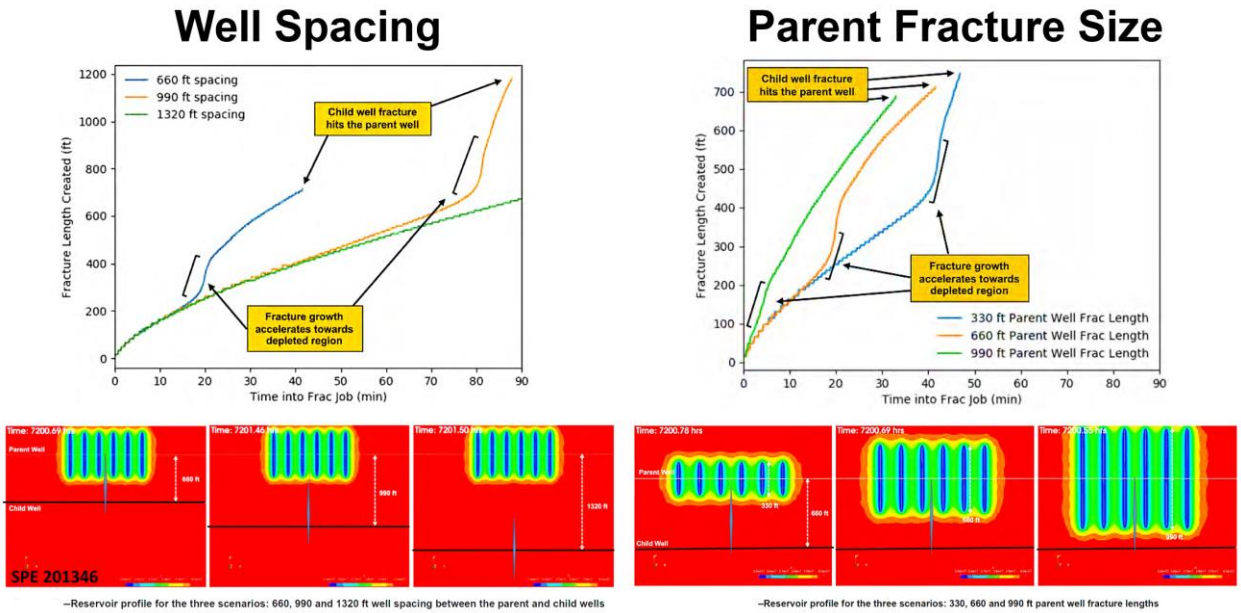

Figure 67: Fracture acceleration in depletion regions (modified from SPE 201346)

Once the response had been measured and the VFR computed, it is now possible to determine the depletion distance. Since fracture length has been shown to follow the square root of volume relationship, Equation 6 can be used to estimate the fracture length at the time the fracture intersects the depletion region (Figure 68).

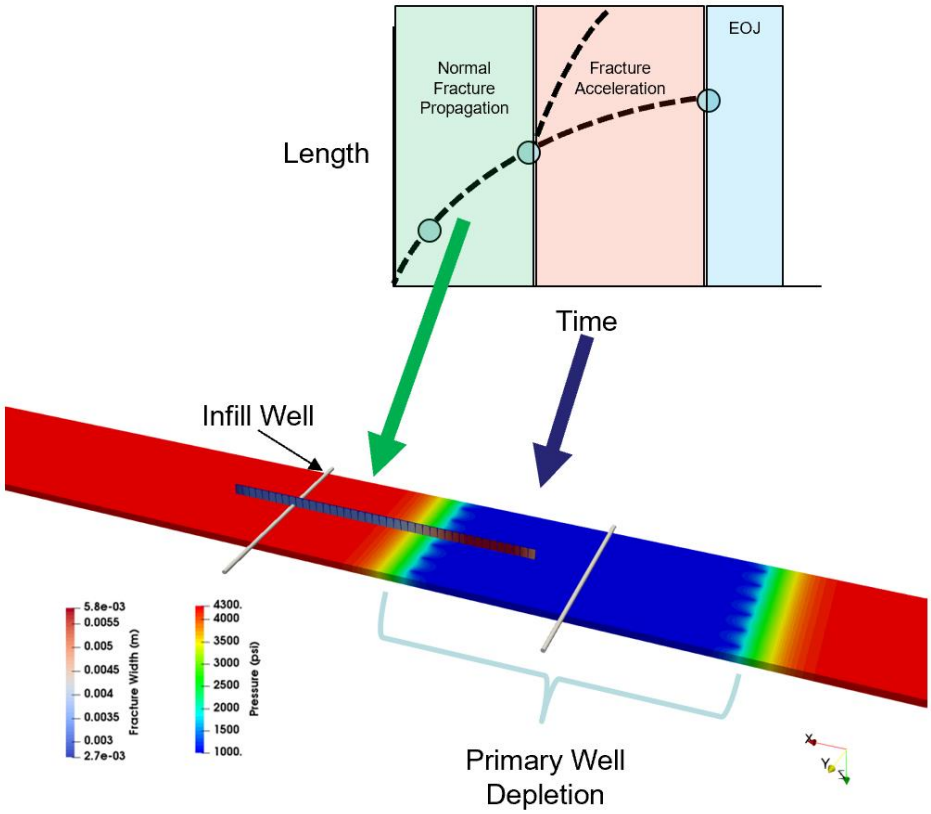

Figure 68: Example of fracture intersecting depletion region, showing asymmetry and acceleration

An example can be seen in Figure 69, with a on azimuth distance of 1,000 ft and a growth rate of 300 ft^2/bbl, with a FDI event observed at 3,775 bbls, one can determine the distance the new fracture grew using Equation 6. The value resolved for these parameters shows a fracture length of 600 ft, inverting the on azimuth well spacing (1,000ft) allows for an estimate of depletion region of 400 ft. A later volume to first response of 6,705 bbls would yield a new fracture distance of 800 ft and a depletion distance of 200 ft. This simple, yet robust method is deployed in a diagnostic dashboard that allows these parameters to be computed rapidly with great utility for interpreting fracture driven interactions.

$$L(v) = \sqrt{\frac{Growth\ Rate_{volume}}{\pi} * VFR} \quad (6)$$

$$600\ ft = \sqrt{\frac{300\ ft^2/bbl}{\pi} * 3775\ bbls} \quad (6a)$$

$$800\ ft = \sqrt{\frac{300\ ft^2/bbl}{\pi} * 6705\ bbls} \quad (6b)$$

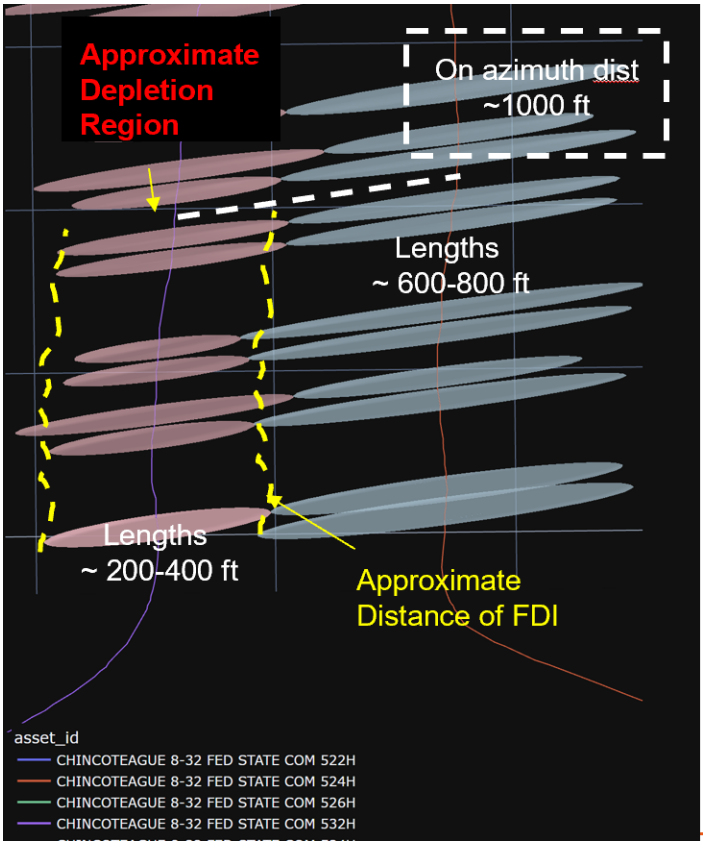

Figure 69: Approximating depletion region using FDI signatures while stimulating infill wells

5.3 UTILIZING MONTE-CARLO SIMULATION FOR CLUSTER EFFICIENCY

A known fracture arrival that has induced a response on a monitoring well is typically considered the dominant fracture or the first to arrive. In a multi-cluster stimulation, there are likely multiple other fractures propagating between the active well and monitor well that have simply not arrived yet. Utilizing thousands of computations (Monte Carlo simulation) on a volume balance for given

arrival times and volumes allows one to compute a distribution of potential secondary fracture geometries and cluster efficiencies.

5.4 SURFACE INVERSION SOLUTIONS

As has been previously published by Manchanda et al. (2019) and Elliott et al. (2018), there are established inversion methods utilizing analytical models to approximate fracture geometry from pressure measurements during fracturing. These models can be extended to couple with the wellbore deformation problem and provide an additional method to gain value from wellbore strain measurements.

A graphical way to represent these solutions is to represent them as a surface plot as shown in Figure 70, then solve for the minimum error using an objective function. The final images produce a local minimum or inverted frac geometry for a unique length, height, and net pressure.

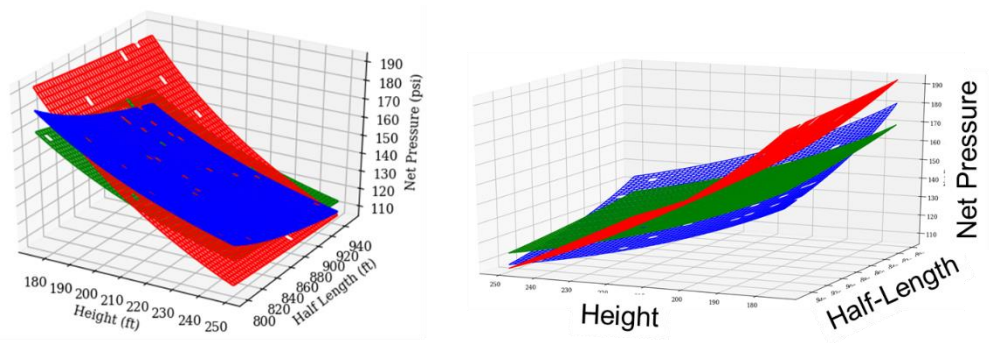

Figure 70: Surface solutions for the analytical model, resolving the possible combinations for height, length, and net pressure.

5.5 WELLBORE AZIMUTHAL STRAIN[3]

This section presents a novel fracture diagnostic method to determine the geometry of multiple propagating fractures. The method relies on the measurement of the Azimuthally Resolved Wellbore Strain Tensor as a function of time at multiple locations in an observation well.

A pad-scale fracturing simulator is used to simulate dynamic fracture propagation in a treatment well. The geometry of the monitoring wellbore is represented with a very fine (millimeter scale) computation mesh to capture the impact of the propagating fractures on the monitoring wellbore. The axial and radial strain at different locations along the wellbore is computed as a function of time as the fractures approach the observation wellbore. These measurements together with the wellbore pressure response are interpreted to obtain the height, length, and width of the fractures as well as the cluster efficiency of the stage.

The emergence of peaks in the strain and pressure monitoring data clearly detects the arrival of each fracture. As the fracture approaches the monitoring well, the tensile strain measured within the wellbore in the axial direction increases, the compressive strain in the radial direction increases, and the sealed wellbore pressure increases. As the fracture intersects the wellbore, the tensile strain in the axial direction decreases, the compressive strain in the radial direction decreases, and the sealed wellbore pressure further increases. When the treatment is complete, both the magnitude of the monitored strain and the pressure decrease. The major axis of the oval wellbore is oriented towards the tip of the propagating fracture. The wellbore ovality, therefore, provides a direct indication of the location of the fracture tip in 3-D.

[3] This section is adapted from paper SPE-209139-MS (Zheng, Shuang, Elliott, Brendan, and Mukul Sharma. "Azimuthally Resolved Wellbore Strain Measurements: A Powerful New Fracture Diagnostics Method." Paper presented at the SPE Hydraulic Fracturing Technology Conference and Exhibition, The Woodlands, Texas, USA, February 2022. *Zheng and Elliott Contributed to this work, Zheng deployed specialized meshing algorithms, and code advancements, while Elliott validated the azimuthal relationship in the laboratory setting and performed numerous simulations of fracture interactions on wellbores with resulting strain, Sharma supervised this research.

This new 3-D fracture diagnostics method allows us to (a) infer the location of the fracture front, (b) estimate the geometry (length, height, width), and (c) determine the cluster efficiency by monitoring the strain tensor as a function of time along an observation well. The validation of our simulator for estimating wellbore strain and pressure has been presented by comparing the simulated results with experiments and field data in Elliott et al. (2022). This research shows how changes in the measured strain and the wellbore ellipticity can be used as a powerful fracture diagnostic tool during both pumping and shut-in periods. Sensitivity studies on the completion design and number of fractures are also conducted to show how the measurements are affected by the number of propagating fractures and the fracture geometry.

Model Description

A fully integrated 3-D hydraulic fracturing and reservoir simulator is used to capture azimuth strain in this section. This is the same simulator described in Chapter 4 in Figure 40 and Equations 7-11. This simulator solves for the strain tensor, fluid flow, pressure and deformation on casing, and other variables as noted by (Elliott et al. 2022; Zheng et al. 2019; Manchanda et al. 2020; Zheng et al. 2021; Zheng and Sharma, 2021).

Case Setup

The computation mesh and case setup for the Base Case are shown in Figure 71. In the Base Case, the treatment well and the monitor well are horizontal wells with the same true vertical depth. The well spacing is $120\ m$. One single hydraulic fracture is initiated from the center of the treatment wellbore, and it propagates towards the monitor wellbore. The hydraulic fracture approaches, intersects, and finally crosses the monitor wellbore (Figure 71). One hour of injection

followed by one hour shut-in is simulated for the Base Case. The computation mesh has a dimension of $200 \times 900 \times 200\, m^3$. The number of grids in the background mesh in three directions are 20, 180, and 40, respectively. The fine mesh for the monitor wellbore is also visible around the black line representing the monitor well.

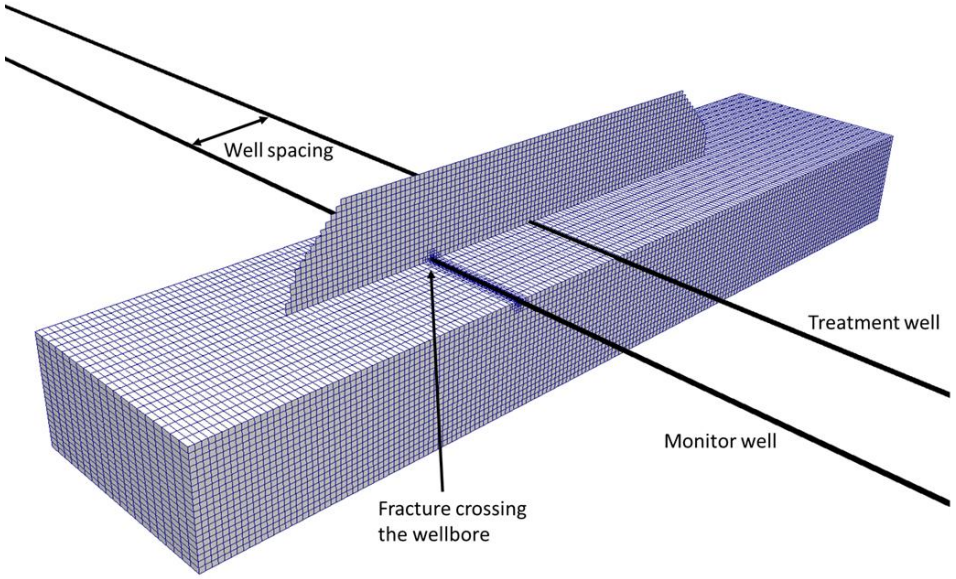

Figure 71. The computation mesh and case setup. The bottom half of the reservoir mesh and the top half of the fracture mesh are shown in this figure.

The offset well is used to monitor the fracture growth from the treating well. The strain and pressure response within the inner side of the monitoring wellbore are measured to enable observation of the fracture growth from the treatment wellbore. The wellbore strain response can be measured by the method proposed by Russell and Sharma (2021). The wellbore pressure change can be measured a pressure gauge at the surface of the sealed wellbore (Haustveit et al. 2020).

A very fine 3-D mesh is required to preserve the wellbore geometry and material properties (steel, cement, and rock) in order to accurately capture the small deformation of the casing. Figure 72 shows the mesh for the monitor well wellbore in a zoomed in view of Figure 71, including a

vertical slice of the computation mesh across the wellbore. In the two figures, the red elements show the steel material while the blue elements show the rock and cement material. The background mesh is refined eight times by a 2:1 refinement around the observation wellbore to a millimeter scale. Five layers of meshes are used to represent the wellbore steel, and the thickness agrees with the difference between the wellbore outer diameter (OD) and inner diameter (ID). The impact of the propagating fractures on the deformation of the monitoring wellbore is thus captured accurately. The axial and radial strain at different locations along the wellbore is computed as a function of time as the fractures approach the observation wellbore. These measurements are interpreted to obtain the height, length and width of the fractures and the cluster efficiency, as well as wellbore pressure response.

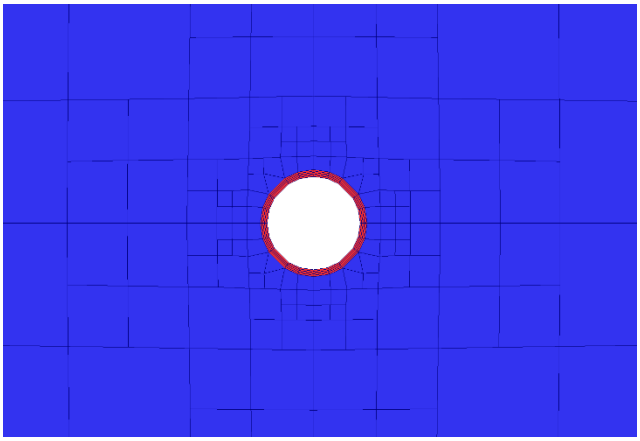

Figure 72. A vertical slice crossing the wellbore. Cells in red represents the casing (steel material). Cells in blue represents the rock and cement.

The computation mesh for the base case has over 2 million cells (grid blocks). The two hour (one hour injection and one hour shut-in) simulation was run using 6 Skylake (Intel Xeon Platinum 8160) nodes with 288 cores on the Stampede2 system of Texas Advanced Computing Center (TACC) at the University of Texas at Austin. The Base Case took a few hours of CPU time to complete.

In the proposed method, the strain tensor is measured at varying locations in the observation wellbore. The top, bottom, front, and back locations are defined for a horizontal wellbore in Figure 73 based on the location of the measured points on the wellbore and the location of the approaching fracture. In fact, using the developed tool, the strain at any location around the wellbore can be measured. Figure 73 also illustrates that the fluid pressure within the monitor wellbore acts as a traction force from the inner side of the wellbore, which balances the in-situ stress outside the monitor well. The definition of the four locations are represented for ease of analysis in the paper. The input parameters in the Base Case are listed in Table 8.

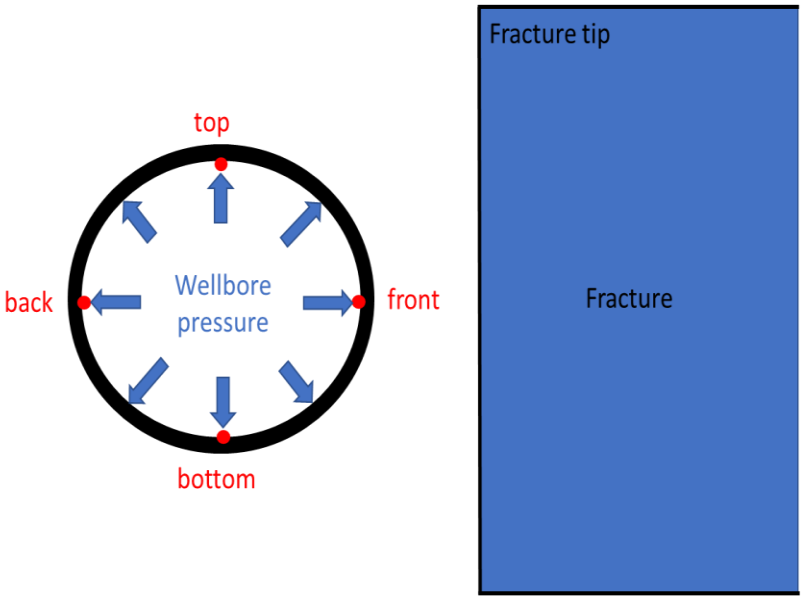

Figure 73. Definition of the top, bottom, front and back location on the inner surface of the observation wellbore.

Table 8. Input parameters for the Base Case

Property	Value	Unit
Fracture height	160	m
Casing inner diameter	0.121362	m
Casing outer diameter	0.1397	m
Rock Young's modulus	38	GPa
Casing Young's modulus	400	GPa
Rock Poisson's ratio	0.21	-
Casing Poisson's ratio	0.27	-
Casing internal pressure	41.37	MPa
Minimum horizontal stress	41.37	MPa
Pore pressure	38.61	MPa
Critical stress intensity factor	5	$MPa \cdot m^{0.5}$

Mesh size for fracture	5	m
Mesh size for wellbore	0.0018338	m
Number of casing mesh layers	5	-
Injection rate	0.0795	m^3/s
Fracturing fluid viscosity	0.005	$Pa \cdot s$
Leakoff coefficient	1×10^{-6}	$m/s^{0.5}$
Number of perforations per cluster	6	-
Perforation diameter	0.0127	m
Treating well volume	55	m^3
Treating well diameter	0.1397	m
Monitoring well volume	52.89	m^3
Matrix porosity	0.05	-
Matrix permeability	2×10^{-18}	m^2
SRV permeability	2×10^{-16}	m^2
SRV length from fracture	5	m

A Base Case simulation using the parameters in the table above is presented and discussed first to establish a typical response signature and will then be expanded upon later. Next, results for two different completion scenarios (fracture propagation towards a horizontal wellbore and fracture propagation towards a vertical observation wellbore) will be presented. Then a multiple fracture propagation case will be discussed. Finally, a sensitivity study on the effects of fracture width and fracture height on the measured strain response will be presented.

Base Case Results

In the Base Case, one hour of injection and one hour of shut-in are simulated. The fracture initiates and propagates from the treating well to the monitor well. One wing of the fracture gradually approaches, hits, and crosses the observation wellbore.

The fracture geometry at injection times of $600\ s$, $900\ s$, $1200\ s$, $1500\ s$, $1800\ s$, and $3600\ s$ are shown in Figure 74. The bottom half of the computation domain and the top half of the fractures are shown. The color scale on the fracture surface shows the fracture width distribution, and the color scalar on the reservoir mesh shows the normal strain along the wellbore

direction (x direction in the figures) inside the reservoir. During the simulation, the fracture propagates to a location that is close to the monitor wellbore after about 10 minutes. After 15 minutes, the fracture intersects the monitor wellbore. Then the fracture tip crosses the monitor wellbore and the fracture width at the monitor wellbore gradually increases as the fracture continues to propagate. The normal strain in the wellbore direction shows compressive deformation (negative magnitude) on the sides of the fractures because of the fracture opening effect and shows tensile deformation (positive magnitude) at the fracture tip.

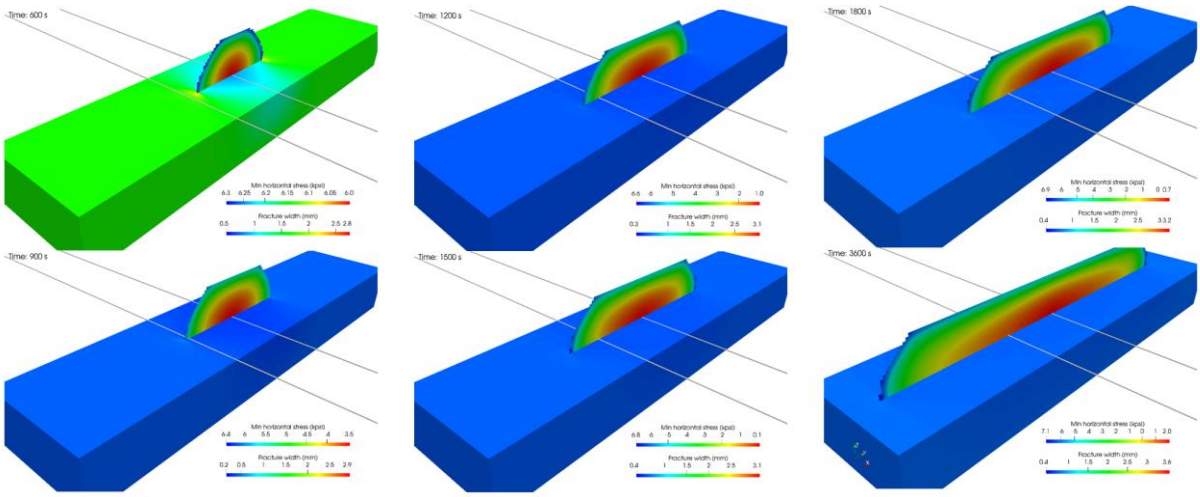

Figure 74: Fracture geometry at various timesteps

The simulator is capable of computing the monitor well strain tensor at different times when fractures propagate towards and past it. Based on the wellbore deformation, the wellbore volume change, and thus the pressure in the monitoring wellbore, can be calculated. In the study, the emergence of peaks and valleys in the strain and pressure monitoring data clearly show the arrival of different fractures. As the fracture approaches the monitoring well, the tensile strain measured within the wellbore in the axial direction increases, and the compressive strain in the radial direction increases. The sealed wellbore pressure increases. As the fracture intersects the wellbore, the tensile strain in the axial direction decreases, and the compressive strain in the radial

direction decreases. The sealed wellbore pressure further increases. When the treatment is complete, both the magnitude of the monitored strain and the pressure decrease due to leakoff and fracture closure.

The normal strains in the x direction (along the wellbore length), y direction (along the wellbore radius), z direction (vertical) at the front location of the wellbore are shown in Figure 75. The results at early times (before the fracture hits the wellbore) and the results at late times (after the fracture hits the wellbore) are plotted separately because there is a distinct difference in the strain magnitude before and after the fracture intersects the wellbore. As shown in Figure 75(a)(c)(e), at zero time (before the treatment well injection starts), there is zero strain along the plotting line at the front location because the initial pressure value in the monitor wellbore is set to be equal to the in-situ stress. As the fractures from the treating well propagate toward the monitor well, the strain magnitude changes. The normal strain along the well length direction (xx) is tensile in the near-fracture region and compressive away from the fracture region. The strain xx magnitude becomes larger as the fracture propagates towards the monitoring wellbore, as shown in Figure 75(a). The normal strain along the well radius direction (yy) is compressive in the near-fracture region and tensile away from the fracture region. The yy strain magnitude becomes larger as the fracture propagates towards the monitoring wellbore as shown in Figure 75(c). The normal strain in the vertical direction (zz) in the near fracture region is initially compressive and becomes tensile as the injection continues. The strain magnitude becomes measurable at around $500\ s$. The approaching tensile region ahead of the fracture tip applies a tensile load on the wellbore and

causes the wellbore to bend slightly towards the hydraulic fracture. This phenomenon will be discussed in detail later in this section.

Figure 75(b)(d)(f) shows the xx, yy, and zz strains after the fracture hits the monitor wellbore and during the shut-in time. It can be observed that within the near-fracture region (5 meters on each side of the fracture), the strain magnitude becomes much larger than it was before the fracture hit the monitor wellbore. The wellbore outside this region has negligible strain values because the fracture tip tensile region has passed the deformed wellbore, and it returns to its original shape. However, because of the direct contact of the wellbore and fracture at distance = 0 in the figures, the strain magnitude around this region becomes much larger than without direct fracture-wellbore contact. One can also observe that the strain magnitude in all directions starts to fall off after shut-in. This can be explained by the fact that during the shut-in period, the fracture width decreases due to leakoff, and the wellbore deformation partially returns to its original shape within the simulated shut-in time.

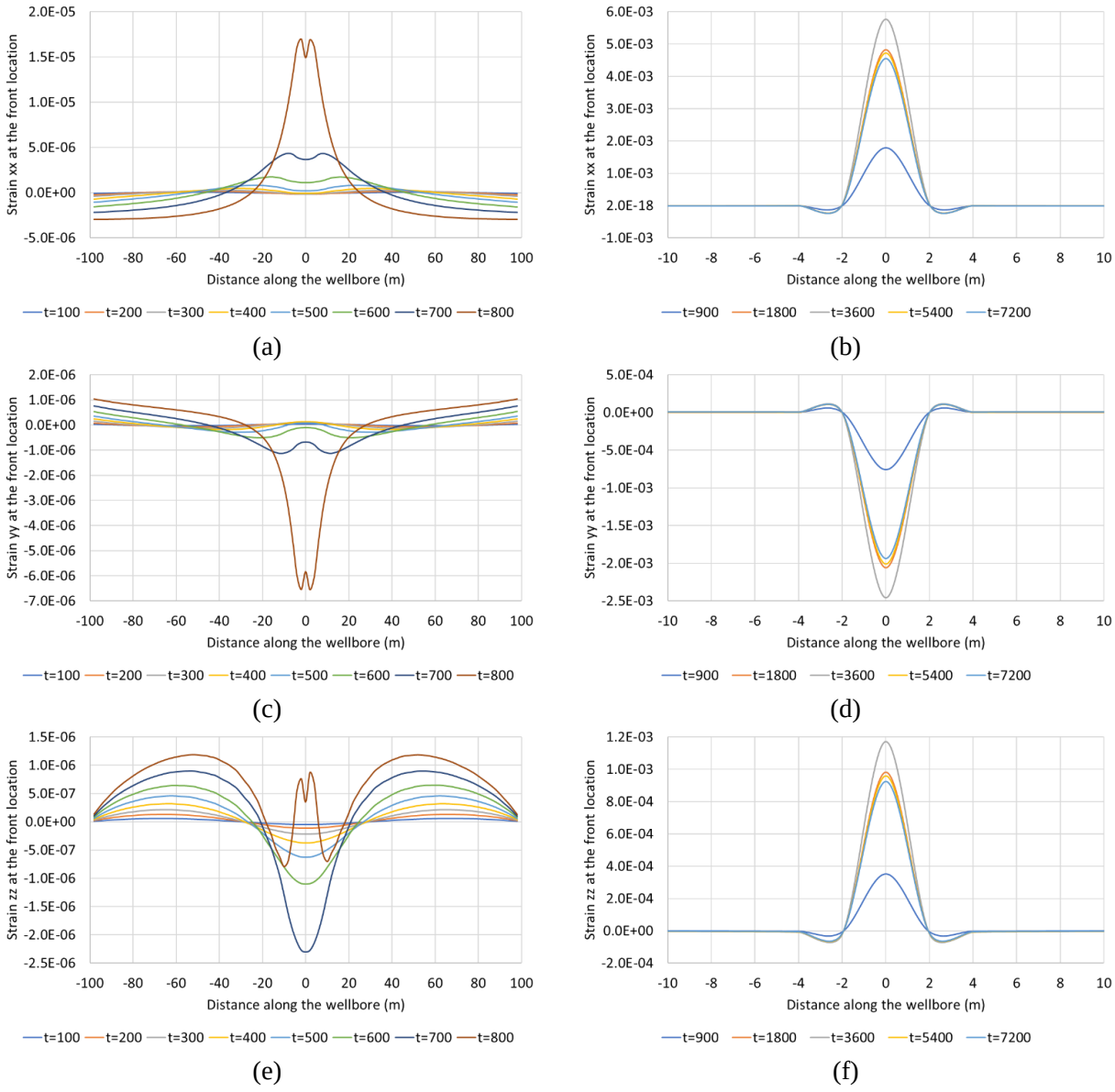

Figure 75: The strain response at the front location extracted at different time steps for the Base Case.

The normal xx, yy, zz strains at the top of the monitor wellbore are shown in Figure 76. In comparing Figure 75 and Figure 76, one can see that the normal strain at both the front and top locations along the wellbore are tensile. The strain yy at the top location follows the pattern of strain zz at the front location, and the strain zz at the top follows the pattern of strain yy at the front location. The casing region right ahead of the fracture tip has an increasing diameter, indicated by the radial compressive stress and longitudinal tensile stress around the casing surface.

Correspondingly, the casing region on the two sides of the fracture tip has a decreasing diameter, indicated by the radial tensile stress and longitudinal compressive stress around the casing surface. The principle of conservation of mass explains this observation.

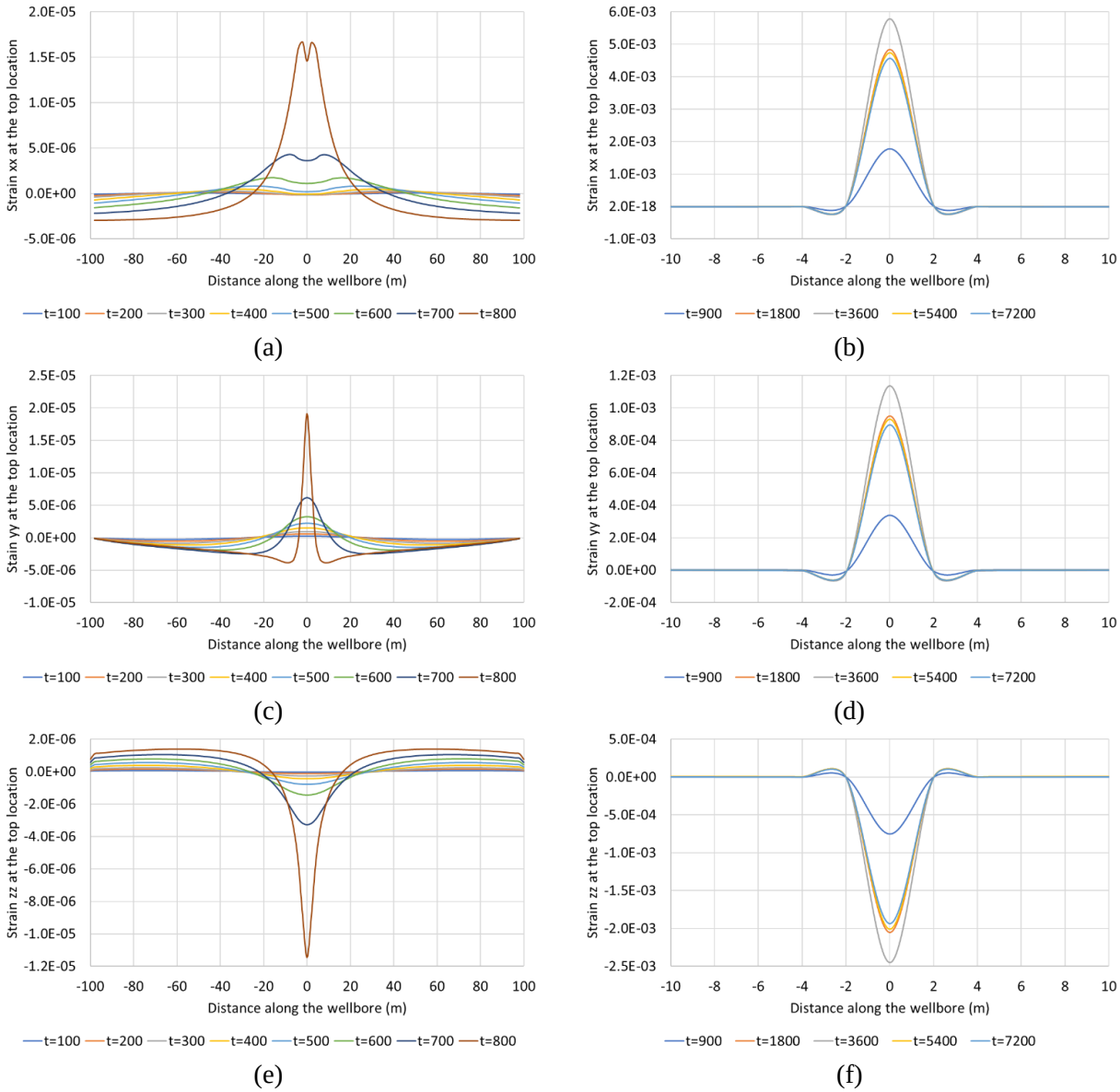

Figure 76: The strain response at the top location extracted at different time step for the Base Case.

The method of utilizing azimuthal strain can be applied to several field problems such as a parent-child well stimulation and fracture driven interactions, wherein hydraulic fractures hitting

the wellbore may cause overstimulation and casing damage. Real time optimization to the treatment schedule can be made whenever an increasing or decreasing magnitude of the strain is observed, to avoid the child well fractures from hitting the parent well fractures or wellbore and over-stimulating the child well. In other field applications such as enhanced geothermal systems, engineers would like to connect the injection well with the production well through hydraulic fractures. With strain monitoring and interpretation, engineers will have the potential to determine and control the connectivity between the injector and producer.

Figure 77 through Figure 80 show the middle section of the casing and three cross sections of the casing at locations 1, 2, 3 labeled in the figures at selected time steps. Location 1 is directly in front of the fracture. Location 2 is $0.25\ m$ from Location 1, and Location 3 is $2\ m$ from Location 1. The color on the casing represents the total magnitude of strain. The coordinates in the y and z directions indicate the (scaled) relative movement of the casing at different times during the stimulation. The center of the casing is located at y = 0 and z = 0 initially. X axis is in red, Y axis is in yellow, and Z axis is in green.

Figure 77 shows the casing shape with three vertical slices after injection for 300 seconds, which is before the fracture arrives at the monitor wellbore. Minimal radial or longitudinal strain observed in the casing shape using the current scaling factor. From the three cross sections, a small horizontal movement towards the hydraulic fracture can be noticed (y axis has some positive value). As the hydraulic fracture is still far away from the monitor wellbore, the strain on the casing is also small.

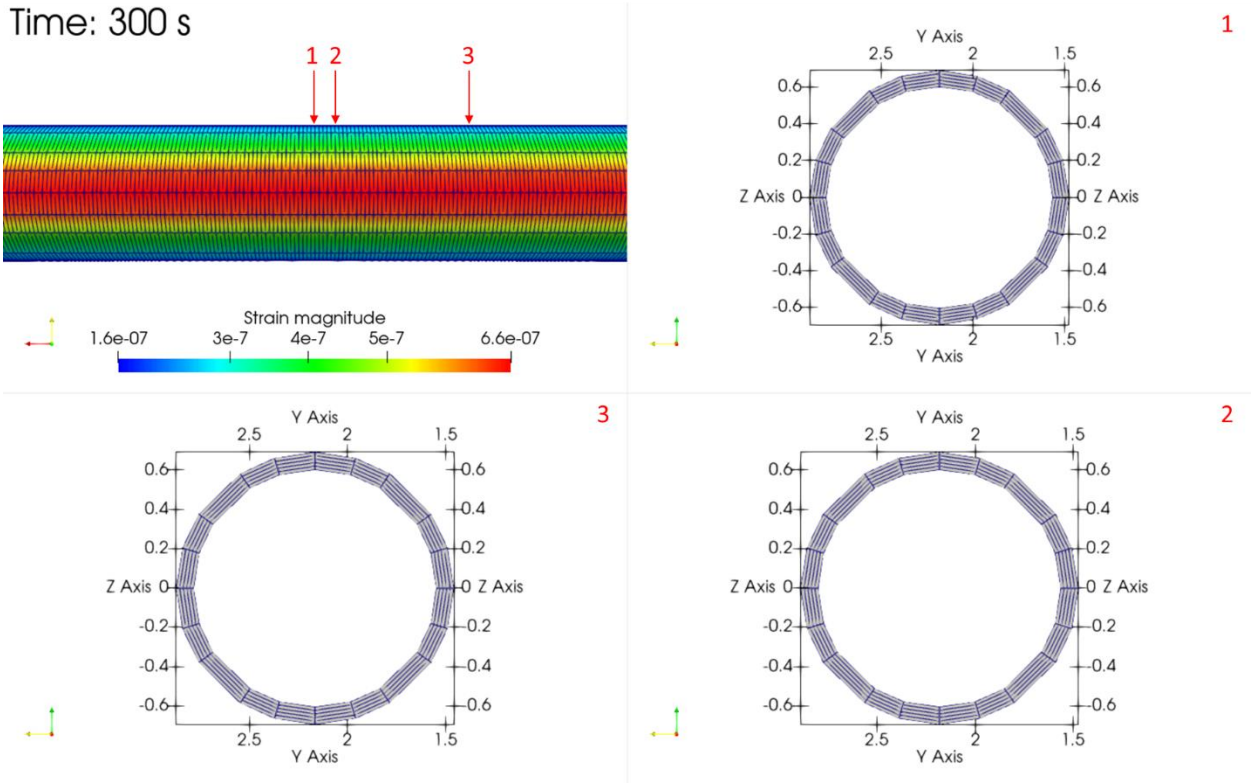

Figure 77. Casing shape after 300 seconds injection (before fracture arrival) for the Base Case. The mesh size has been enlarged 10 times. The deformation has been enlarged 200 times in the top left figure. In the other three figures, the displacement vector is scaled by a factor of 100,000 for visualization purposes.

Figure 78 shows the casing shape with three vertical slices after injection for 792 seconds. At this time, the hydraulic fracture is very close to the monitoring wellbore. Figure 78 shows that the casing bends towards the hydraulic fracture due to the tensile region ahead of the fracture tip. The three cross sections also indicate larger horizontal movement of the casing towards the hydraulic fracture (left side) as well as display the oval cylindrical shape of the casing cross sections. The strain magnitude on the casing is two orders of magnitude larger than in Figure 77. The change in the strain and ovality of the casing is already measurable by downhole measurement tools.

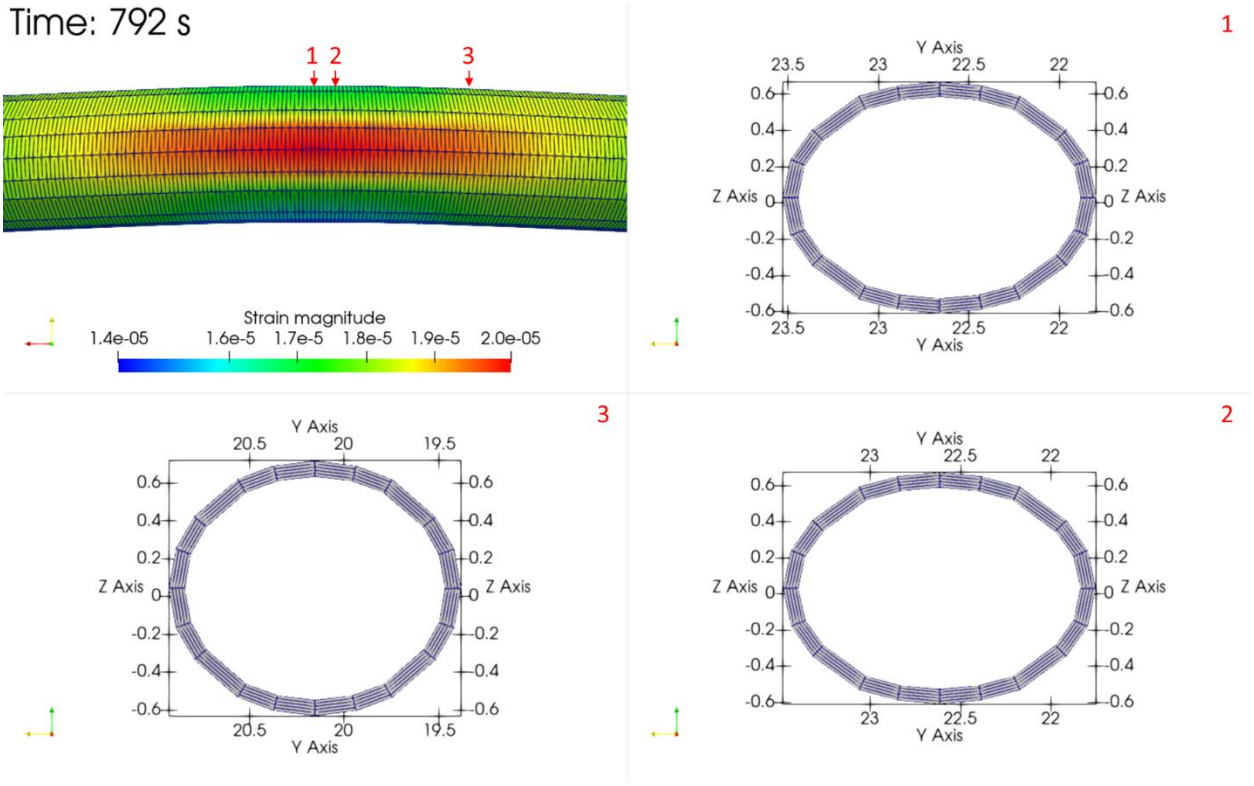

Figure 78. Casing shape after 792 seconds injection (upon fracture arrival) for the Base Case. The mesh size has been enlarged 10 times. The deformation has been enlarged 200 times in the top left figure. In the other three figures, the displacement vector is scaled by a factor of 100,000 for visualization purposes.

Figure 79 shows the casing shape with three vertical slices at the end of injection (3600 seconds). The casing diameter increases in the section ahead of the fracture and decreases on the two sides of the fracture. The deformation at 2 meters away from the hydraulic fracture (Location 3) is very small compared with Location 1 but is still within the measuring range of downhole measurement tools. At the center of the casing, the strain magnitude is three orders of magnitude greater than in Figure 78, as there is direct wellbore-fracture contact after the fracture crosses the wellbore, and the fracture width at the contacting point (Location 1) grows to the largest value at the end of the injection. We also notice the obvious casing ovality change at Locations 1 and 2. Moreover, as the tensile region ahead of the fracture tip passes the monitor wellbore, the casing partially returns to its original location (y = 0 and z = 0).

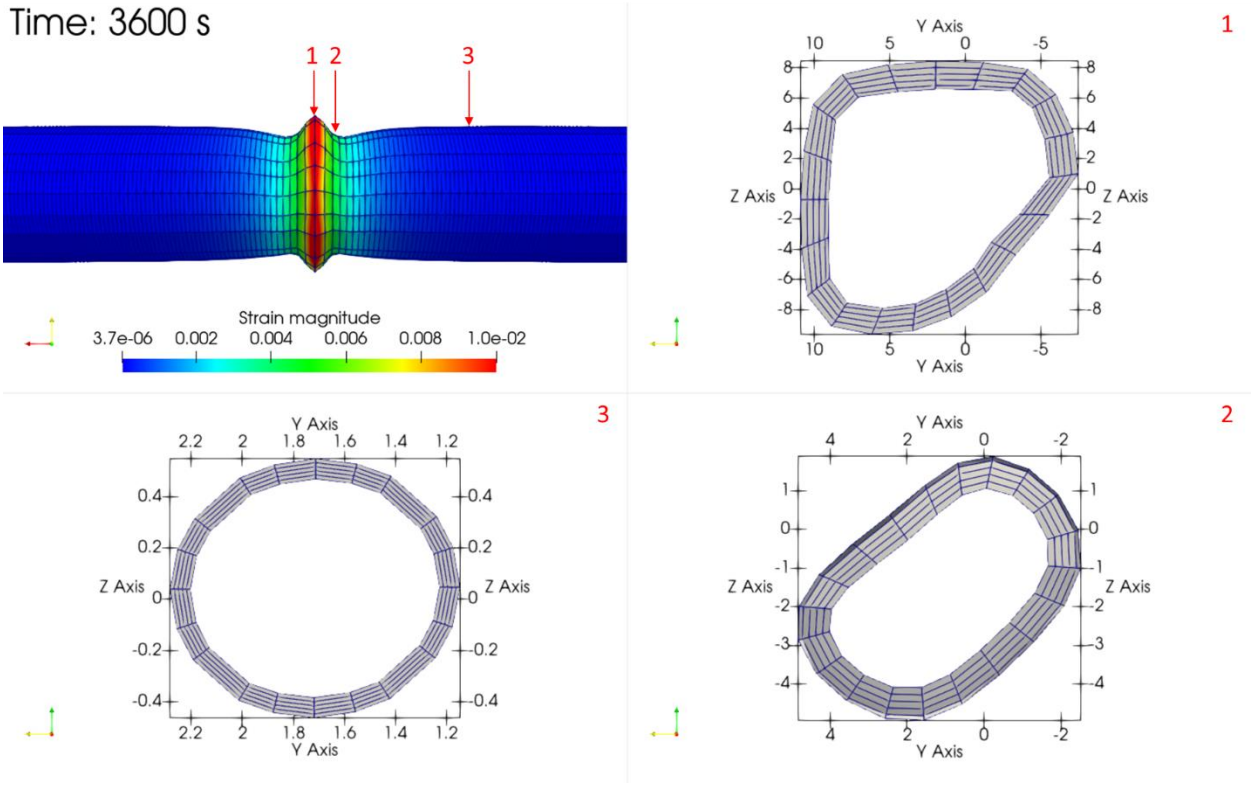

Figure 79. Casing shape at the end of injection (after fracture arrival) for the Base Case. The mesh size has been enlarged 10 times. The deformation has been enlarged 200 times in the top left figure. In the other three figures, the displacement vector is scaled by a factor of 100,000 for visualization purposes.

Figure 80 shows the casing shape with three vertical slices at the end of shut-in (7200 seconds). Relaxation of the strain on the casing is observed, and the wellbore returns to its original location. The ovality of the wellbore diameter also decreases back towards the original circular shape. These are the effects of fluid leakoff and fracture closure.

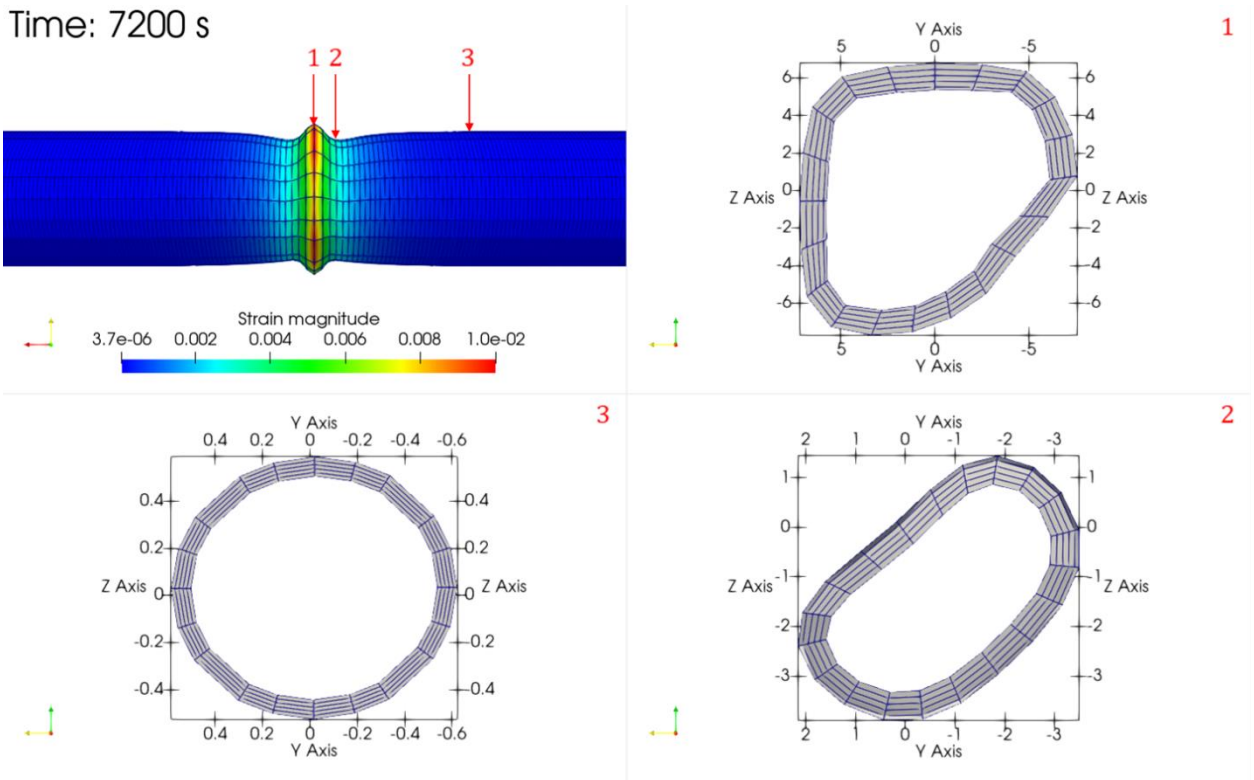

Figure 80. Casing shape at the end of shut-in for the Base Case. The mesh size has been enlarged 10 times. The deformation has been enlarged 200 times in the top left figure. In the other three figures, the displacement vector is scaled by a factor of 100,000 for visualization purposes.

Based on the simulated wellbore deformation, the volume change of the monitor wellbore can be calculated, after which the pressure change in the monitor wellbore can be calculated. The pressure change within the monitor wellbore versus time is plotted in Figure 81. Three periods are shown in the pressure curve. In the initial period during which the fracture is away from the wellbore, the wellbore deformation is small, and a small increase in the wellbore pressure is observed. When the fracture crosses and passes the monitor wellbore, there is a sharp increase in the wellbore pressure, which corresponds to the large wellbore deformation when the fracture is close enough to the monitor wellbore. After the treatment well is shut-in, the wellbore deformation begins to decrease because of the fracturing fluid leakoff and relaxation of the stress acting on the monitor wellbore, and the wellbore pressure decreases gradually. This pressure increase-decrease pattern also matches the pressure data measured in the field as reported by Elliott et al. (2022).

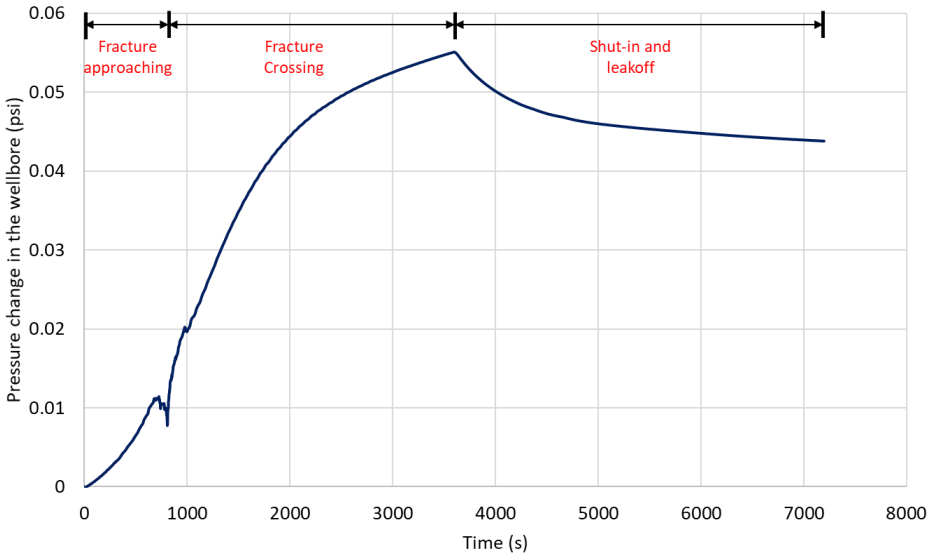

Figure 81. Pressure change within the monitor wellbore versus time at different stages of the treatment for the Base Case.

Fracture Propagating Under the Monitoring Wellbore

There is a certain condition that presents itself in major field developments with stack and staggered wellbore patterns: a fracture may pass underneath a monitor well and still induce subtle deformation. Ugueto et al. (2023) presents this specific case of a fracture passing underneath a monitor well and inducing strain on a fiberoptic cable. To simulate this, the monitor wellbore was placed 100 m above the treatment well. In this case, the top of the fracture tip will be 20 m from the monitor wellbore in the vertical direction, which means the fracture will propagate under the monitoring wellbore. The domain size in the vertical direction is changed to 300 m while all other parameters stay the same as the Base Case.

The fracture geometry at injection times of 600 s, 900 s, 1200 s, 1500 s, 1800 s and 3600 s are shown in Figure 82. It is evident that the treatment wellbore is deeper than the monitor wellbore. The fracture gradually propagates towards the monitor wellbore and passes the monitor wellbore, but it does so without direct contact between the monitor wellbore and the hydraulic fracture.

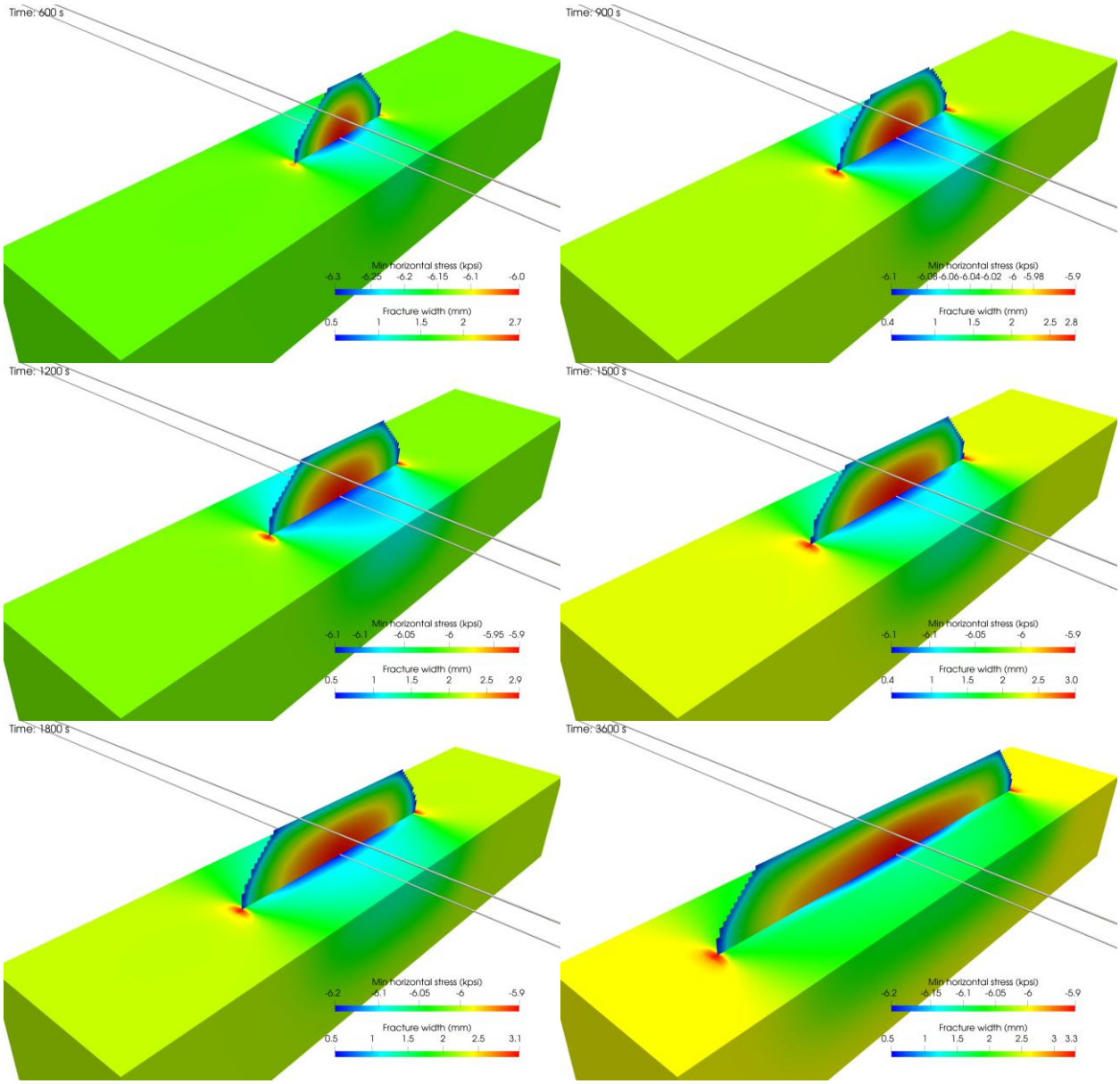

Figure 82: Fracture geometry at different times for the fracture propagation under the monitor wellbore.

The xx, yy, zz strains measured at the bottom point of the casing are shown in Figure 83. It is obvious that the normal strain magnitude in all three directions in this case are much lower than the strain magnitude in the Base Case, even after the fracture has passed the monitoring wellbore. The strain xx right on top of the hydraulic fracture is compressive in the early period and becomes tensile in the late period. The strain xx on the two sides of the fracture is tensile in

the early period and becomes compressive in the late period. The strain yy shows the opposite trend compared to the strain xx. The strain zz right on top of the hydraulic fracture is compressive and becomes more compressive throughout the injection. The strain zz on the two sides of the fracture is tensile and becomes more tensile as the fracture continues to propagate.

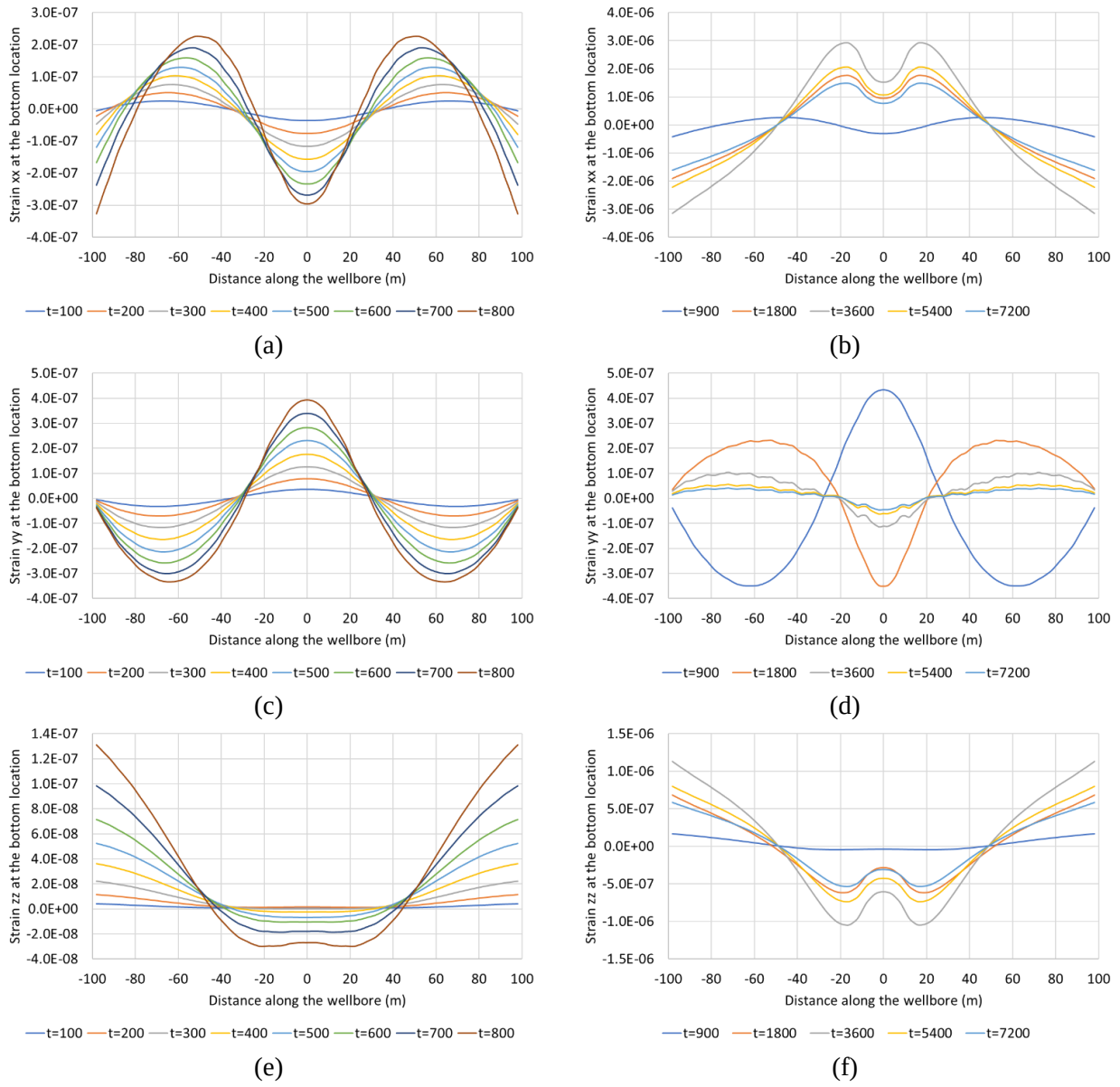

Figure 83: The strain response at the bottom location extracted at different time steps for fracture propagation under monitor wellbore.

The above monitored strain behavior can be explained by the monitor wellbore deforming as the hydraulic fracture propagates past it. Figure 84 and Figure 85 show the horizontal monitor wellbore geometry after 900 and 3600 seconds of injection, respectively. In these two figures, two cross sections of the wellbore at Locations 1 and 2 are also shown, in which Location 1 is right above the propagating fracture and Location 2 is 2 m from Location 1. By comparing the relative movement of the casing shown in the two figures, one can notice that before the fracture nears the wellbore, the monitoring wellbore moves both forward and downward towards the fracture (downward and leftward as shown in Figure 84), due to the tensile region in front of the hydraulic fracture tip. An obvious ovality change towards the propagating fracture is also observed in Figure 84. As the fracture passes the monitor wellbore, the horizontal displacement is reduced, and the vertical displacement increases. This explains the inverse sign in the xx and yy strains and the consistent increase in the compressive zz strain. The shape of the casing changes to "standing" oval, where the top and bottom points of the casing are much further apart than back and front points. We also notice from Figure 85 that the vertical deformation is the largest (more negative z value) in the center of the wellbore and gradually decreases towards the two ends of the wellbore. Figure 86 shows the schematic plot of casing deformation and fracture location after 900 and 3600 seconds injection, which is consistent with the casing ovality changes and fracture tip locations shown in Figure 84 and Figure 85.

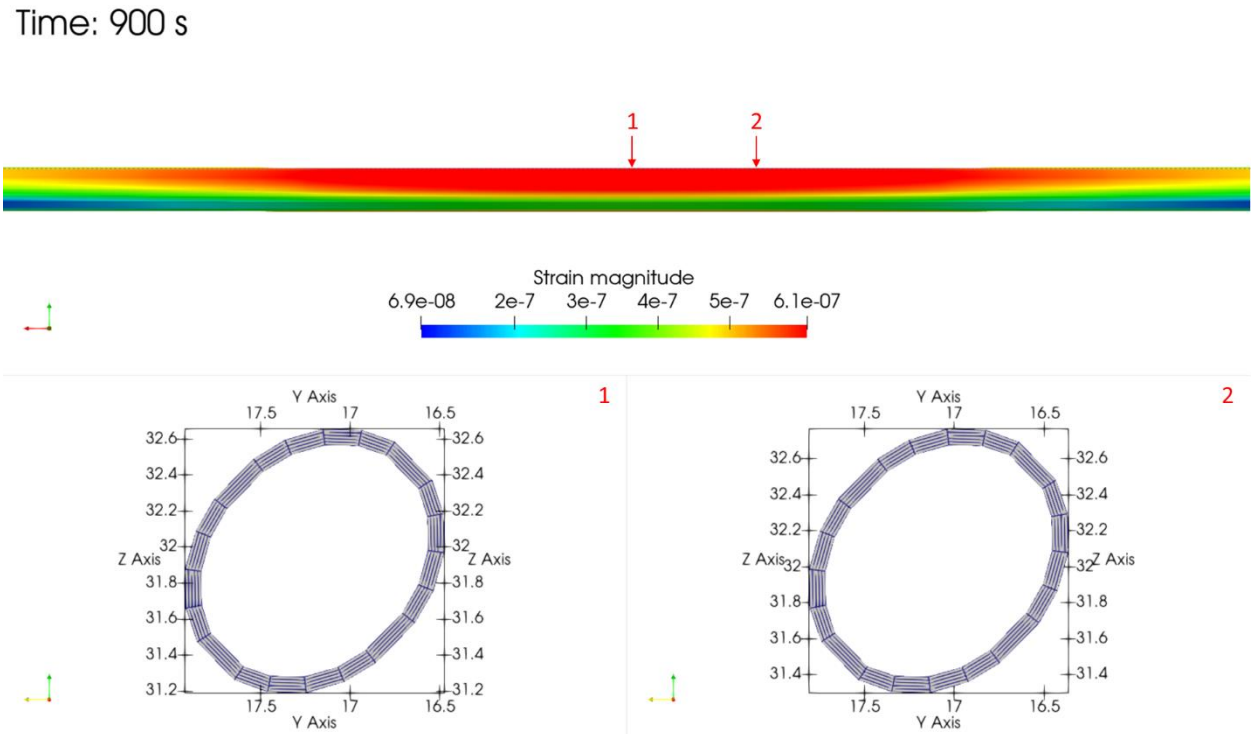

Figure 84. Casing shape after injection for 900 s for the fracture propagation under monitor wellbore. The mesh size has been enlarged 10 times. The deformation has been enlarged 200 times in the top figure. In the other two figures, the displacement vector is scaled by a factor of 1,000,000 for visualization purposes.

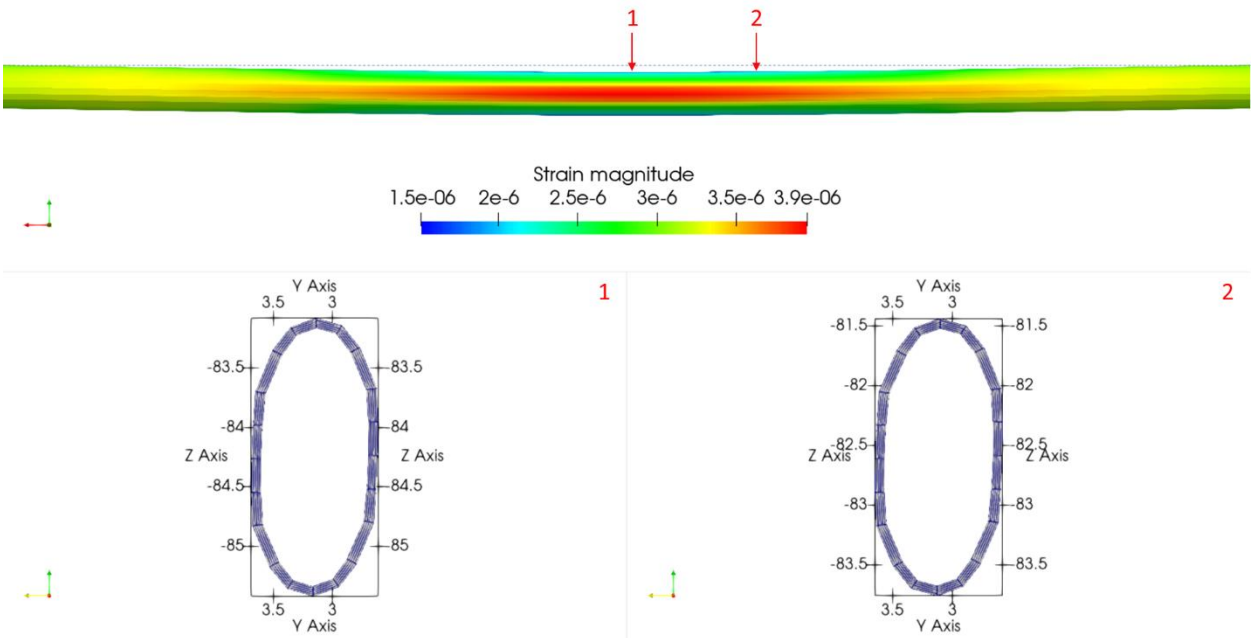

Figure 85. Casing shape at the end of injection (3600 s) for the fracture propagation under monitor wellbore. The mesh size has been enlarged 10 times. The deformation has been enlarged 200 times in the top figure. In the other two figures, the displacement vector is scaled by a factor of 1,000,000 for visualization purposes.

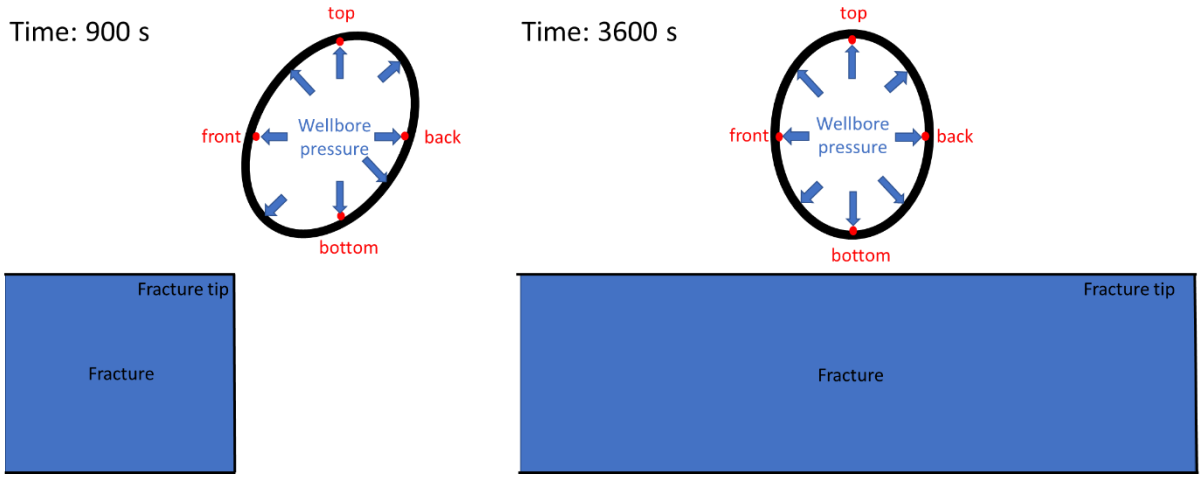

Figure 86. Schematic plot of casing deformation, fracture location after 900 and 3600 seconds injection.

After calculating the wellbore deformation, the pressure change versus time is computed and plotted in Figure 87. We see a consistent pressure increase during the injection phase and a pressure decrease during the shut-in phase. During the injection phase, the pressure changes slowly in the beginning, and the change accelerates as the fracture arrives under the wellbore. The pressure change slows down once the front tip of the fracture passes the monitor wellbore. We notice that the magnitude of pressure change is much smaller than the pressure change in the Base Case. This is because there is no direct contact between the wellbore and fracture; the force applied on the casing is smaller and thus there is a smaller change in the wellbore volume. For the same reason, the pressure falloff during the shut-in period is much faster than the falloff rate in the Base Case.

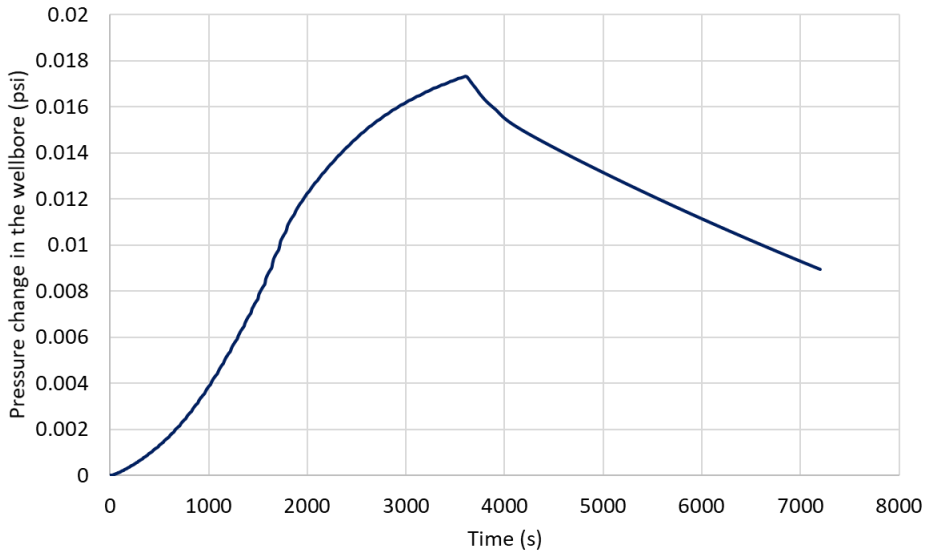

Figure 87. Pressure change within the monitor wellbore versus time at different stages of the treatment for fracture propagation under the monitor wellbore.

Fracture Propagation Past a Vertical Wellbore

In this subsection, we change the horizontal monitor wellbore into a vertical wellbore and decrease the distance between the hydraulic fracture and the vertical wellbore to $50\ m$. All other case settings are kept the same as the Base Case.

The fracture geometry at injection times of $600\ s$, $900\ s$, $1200\ s$, $1500\ s$, $1800\ s$ and $3600\ s$ for the vertical monitor wellbore case are shown in Figure 88. The tensile region ahead of the fracture tip (red region) and the compressive region on the two sides of the fracture (blue region) are clearly observed. As the fracture propagates, the tensile region nears the vertical wellbore at $600\ s$ and reaches the vertical wellbore at $900\ s$. Then the vertical wellbore experiences the increasing compressive stress induced by the hydraulic fracture as the fracture propagates past the vertical wellbore, and the increasing fracture width causes the compressive stress to grow with time.

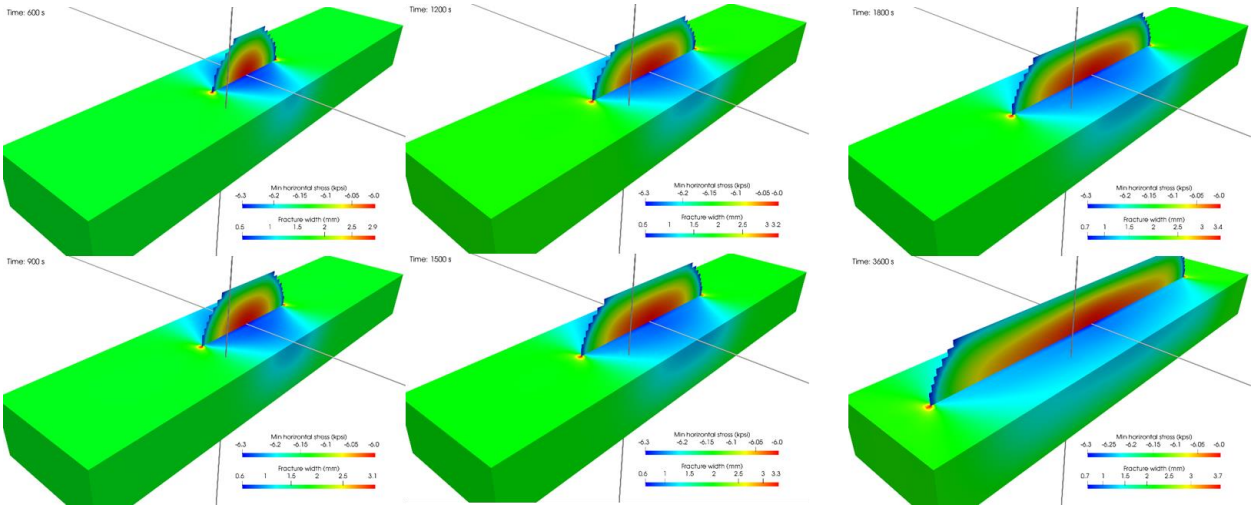

Figure 88: Fracture geometry at different times for the vertical monitor wellbore case.

The xx, yy, zz strains measured on the casing side that faces the hydraulic fracture are shown in Figure 89. In the vertical wellbore case, the xx strain represents the normal strain in the radial direction, the yy strain represents the normal strain in the fracture propagation direction, and the zz strain represents the normal strain in the vertical (wellbore) direction. From Figure 89, the radial strain (xx) along the measured points on the wellbore is tensile as the hydraulic fracture approaches the wellbore because of the tensile region ahead of the fracture tip. After the fracture arrives and passes the vertical wellbore, the vertical section facing the fracture surface (shadowed by the fracture surface) shows compressive radial strain, while the top and bottom vertical sections show an even larger tensile strain. The middle vertical section is affected by the compression induced by the hydraulic fracture, while the top and bottom sections face a larger attraction from the fracture tips at the top and at the bottom of the fracture, respectively. The normal strain in the fracture propagation direction (yy) first shows compression and then shows tension. In the vertical (longitudinal) direction, it shows increasing tensile strain in the region shadowed by the fracture and increasing compressive strain in the top and bottom sections, which is also a direct result of the attraction from the fracture tip followed by squeezing from fracture opening. The strain

magnitude is small compared to the Base Case because of the large distance between the propagating fracture and vertical wellbore, but it is still measurable when the fracture is close to the monitor wellbore.

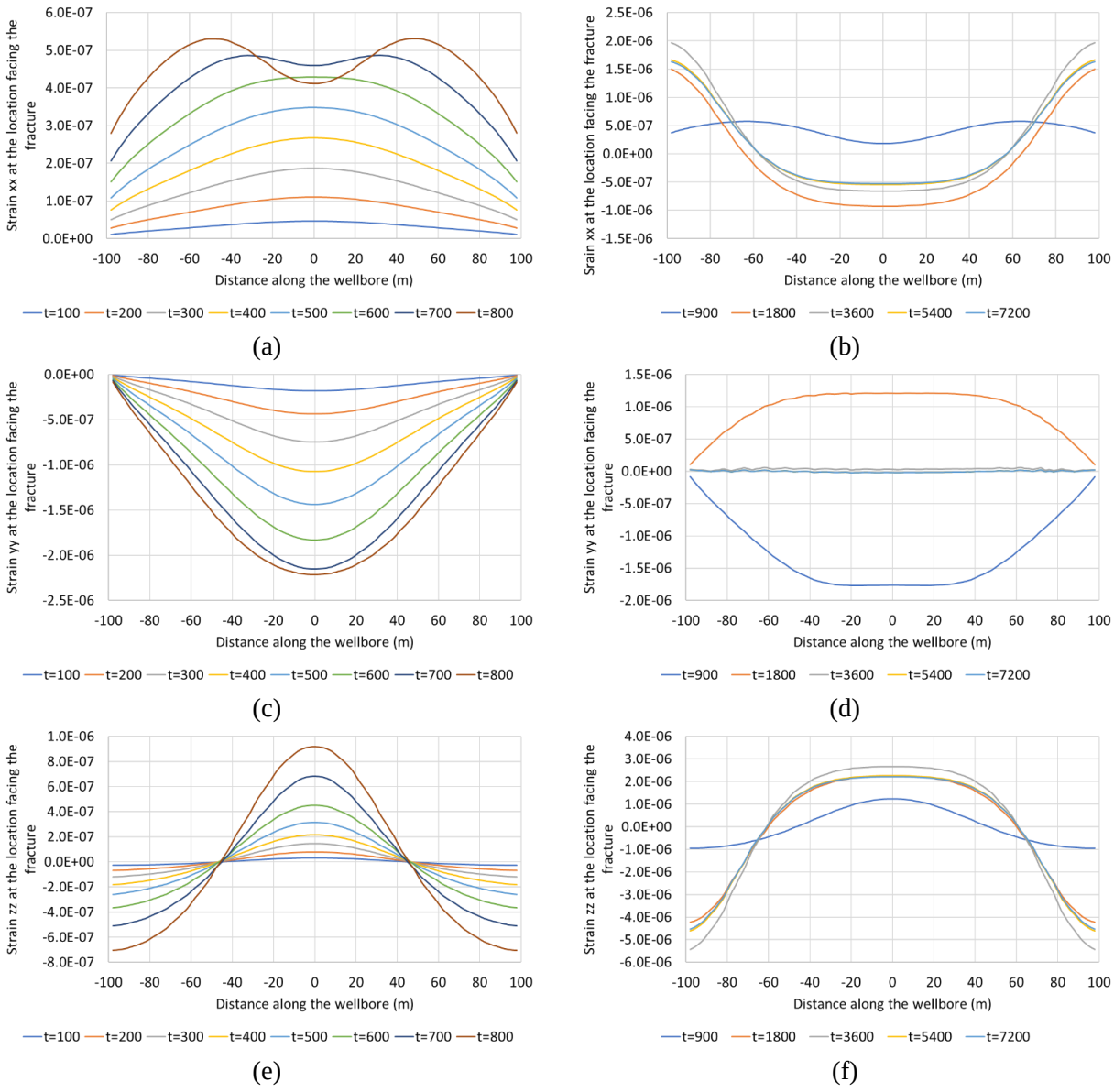

Figure 89: The strain response along the wellbore at the location facing the hydraulic fracture at different time steps for the vertical monitor wellbore.

The pressure change within the monitoring wellbore versus time is plotted in Figure 90 for the vertical wellbore case. The pressure increasing-decreasing pattern is also observed from the

figure. However, a larger pressure magnitude is observed compared to the previous two cases. This can be explained by the large fracture induced stress shadow all along the wellbore length. The strain signals shown in Figure 75 and Figure 76 for the Base Case are more concentrated at the "fracture hit" location whereas the strain signals shown in Figure 89 are more diffuse for the vertical wellbore case. The summation of small deformations along the wellbore gives a larger total wellbore volume change, which makes the pressure magnitude larger than the horizontal monitor wellbore.

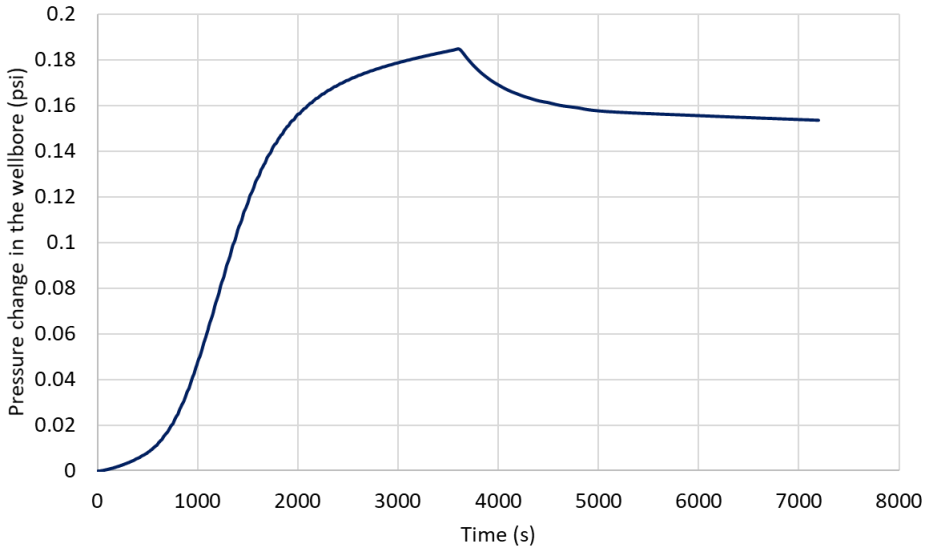

Figure 90. Pressure change within the monitor wellbore versus time at different stages of the treatment for the vertical monitor wellbore.

Multiple Fracture Propagation Case

In this subsection, a five-cluster case is investigated with a cluster spacing of $20\,m$. The well spacing is $150\,m$. The fracture height is $40\,m$. The injection rate is $0.2\,m^3/s$. All other settings are same as the Base Case.

The fracture geometry at injection times of $300\ s$, $400\ s$, $500\ s$, $600\ s$, $900\ s$ and $1800\ s$ for the multiple facture case are shown in Figure 91. From Figure 91, we can see that the two book-end fractures and the fracture in the middle propagate faster than the other two fractures. These three fractures hit the monitor wellbore first followed by the other two fractures. The first three fracture hits happen after injection for $500\ s$, and the last two fracture hits happen after injection for $600\ s$.

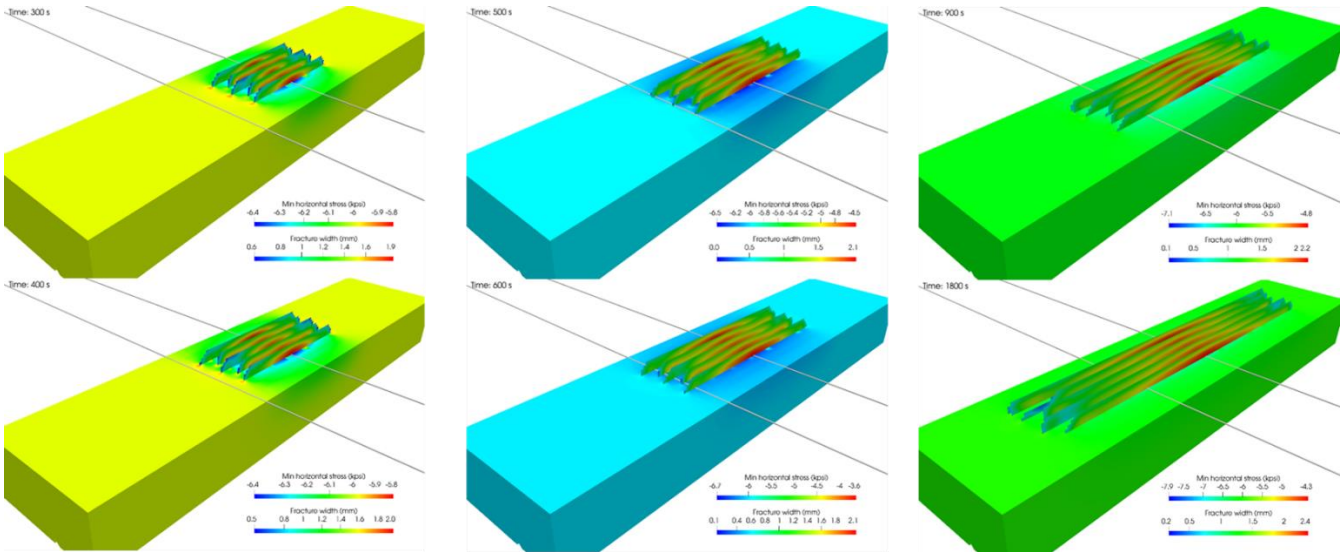

Figure 91: Fracture geometry at different times for the multiple fracture propagation.

The sequence of fracture arrivals is also clearly shown in the extracted strain along the wellbore path at different times displayed in the waterfall style plot (Figure 92). This image is used to emulate the response observed in fiberoptic cable deployments along the wellbore.

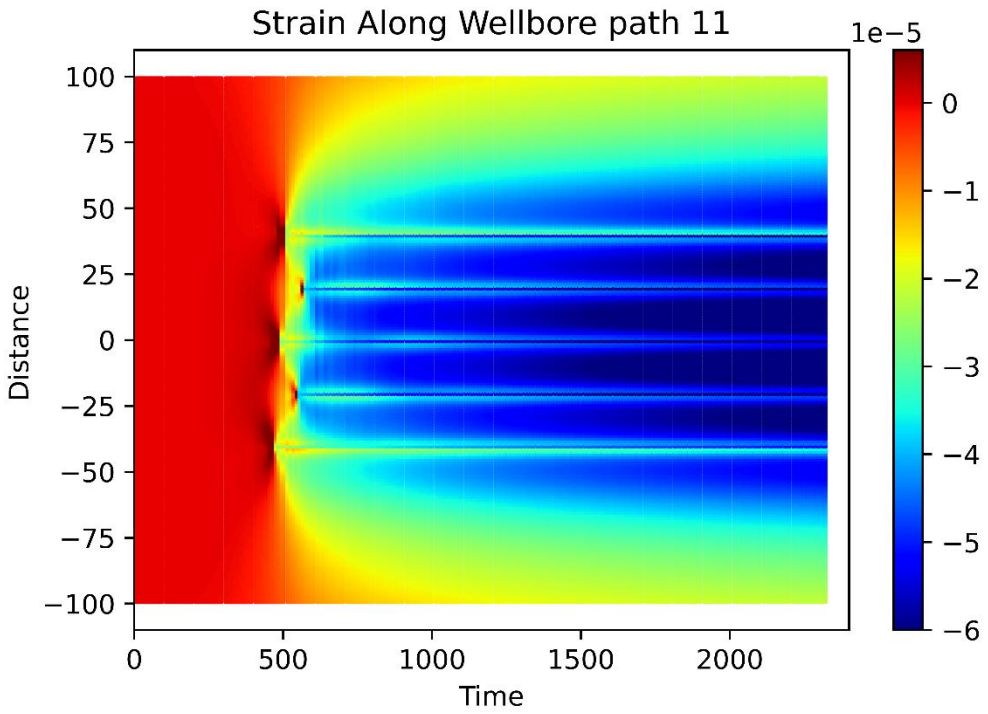

Figure 92. Waterfall plot of extracted strain along the monitor wellbore versus time.

The recorded strain responses at the front location along the wellbore are plotted in Figure 93. Figure 93(a)(c)(e) show the computed strain before the fractures cross the monitoring wellbore. The signal becomes obvious after 300 s injection time, and peaks at -40 m, 0 m, 40 m are all observed on the 400 s curve in the xx, yy, zz plots. These three peaks correspond to the three leading hydraulic fractures shown in Figure 91 and Figure 92. Figure 93(b)(d)(f) shows the recorded strain data at 500 s and 600 s. Three peaks are observed on the 500 s curve, and five peaks are observed on the 600 s curve. The measured strain data clearly indicates the arrival of hydraulic fractures at different locations. In the 500 s curve, the highest peak appears at -40 m followed by peaks at 0 m and 40 m, which implies the largest contact at -40 m, intermediate contact at 0 m, and smallest contact at 40 m. It also implies that the fractures at -20 m and 20 m have not arrived yet. The five high strain peaks in the curve for 600 s demonstrate that all five

fractures hit the monitor wellbore after 600 *s* injection time, which is also depicted in the fracture geometry plot at 600 *s* shown in Figure 91.

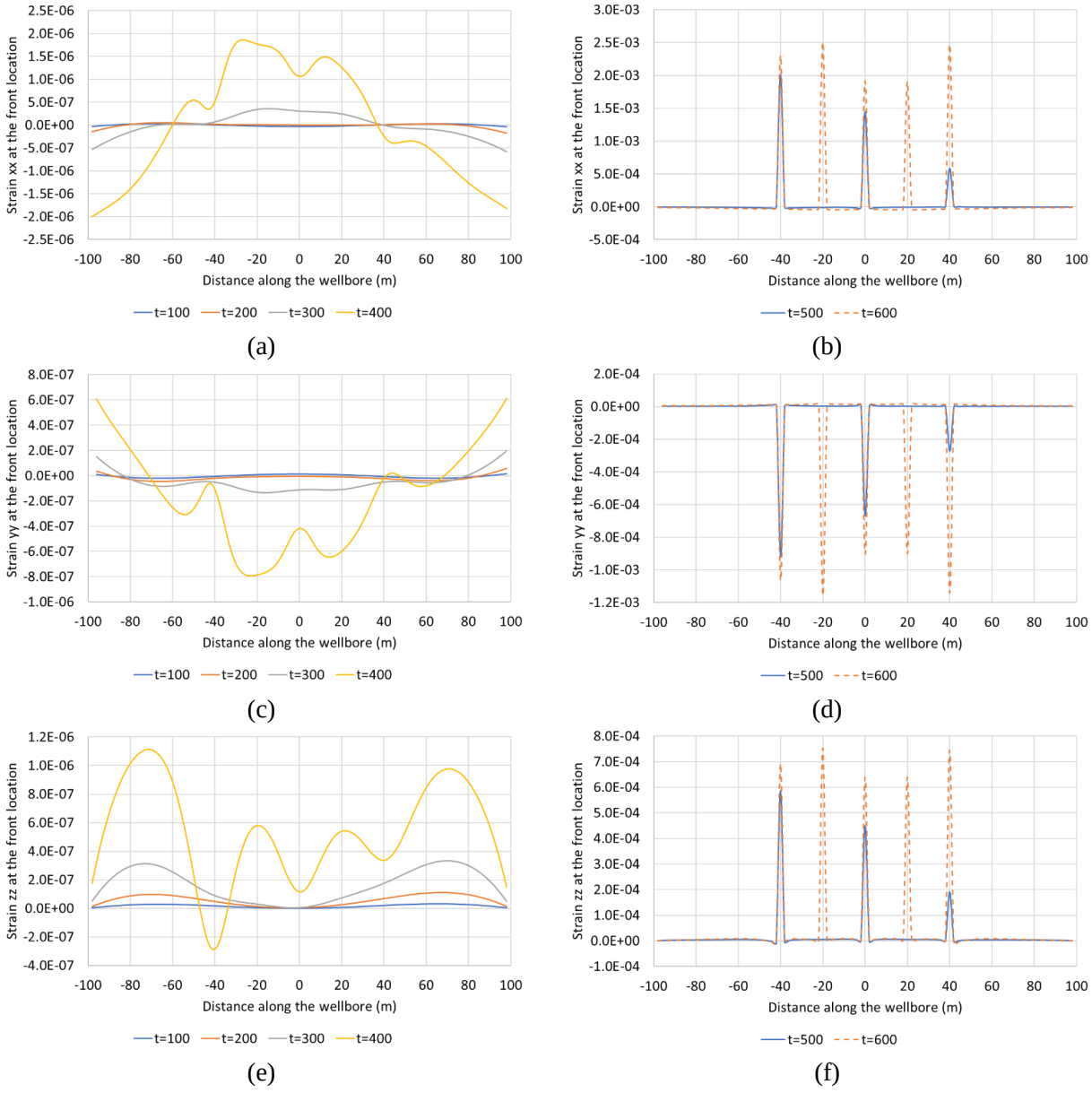

Figure 93: The strain response at the front location extracted at different time steps for the multiple fracture propagation.

The recorded pressure response within the sealed monitor wellbore versus time is plotted in Figure 94. There is an initial slow increase in the monitor wellbore pressure caused by fracture

propagation and wellbore deformation. The pressure curve has a high slope between 400 s and 600 s, at which time the fractures hit the wellbore. After 600 s, all the fractures cross the monitor wellbore and propagate forward (as shown in Figure 91). The increase in the fracture width at the crossing location further increases the pressure value within the wellbore, but the rate of pressure change is not as large as with direct fracture intersections.

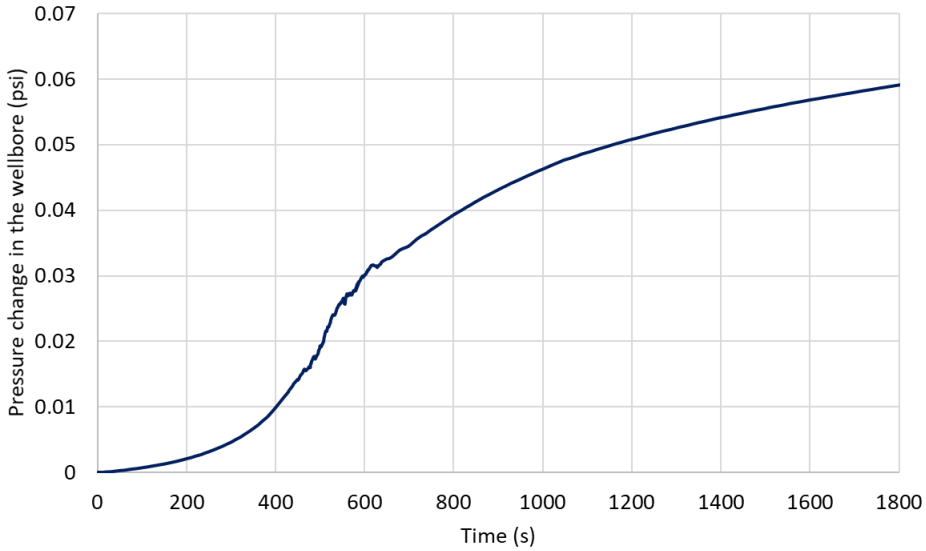

Figure 94. Pressure change within the monitor wellbore versus time at different stages of the treatment for the multiple fracture propagation.

Sensitivity to Fracture Width and Height

The monitored strain is sensitive to fracture width and height. While results are available for any time step, only two snapshots are presented for brevity: the fracture tip is 20 meters away from the monitor wellbore and the fracture tip is 20 meters past the monitor wellbore.

The sensitivity of the measured strain to the fracture width is shown in Figure 95. The fracture height is fixed to be 80 meters, and fracture widths of 0.01, 0.05, 0.1, 0.5, and 1 mm are simulated. Both the results before fracture arrival and after fracture arrival show that larger fracture width results in a larger strain response at the wellbore. It is also found that the measured

strain is proportional to the fracture width, which means that the strain curves will coincide with each other if scaled by the fracture width.

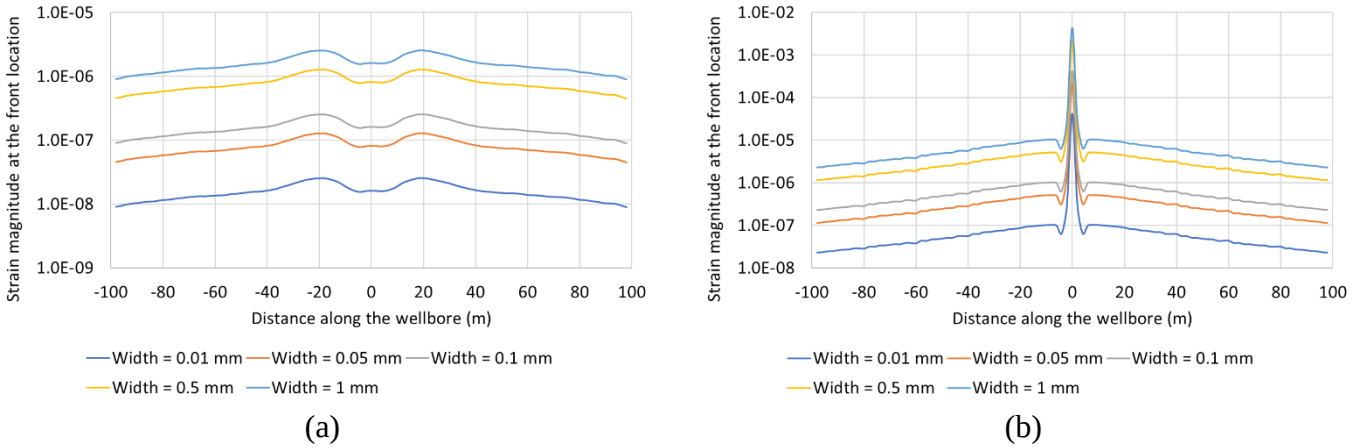

Figure 95. Strain magnitude at the front location of the wellbore for different fracture width. Fracture height is fixed at 80 meters. (a) Fracture tip is 20 meters from the wellbore. (b) Fracture is 20 meters past the wellbore.

The sensitivity of the measured strain to the fracture height is shown in Figure 96. The fracture width is fixed at 0.5 mm, and cases with fracture heights of 40, 80, 120, and 160 m are simulated. It is found that before fracture arrival, a larger fracture height gives a larger strain response along the wellbore. However, the increase in strain magnitude is not proportional to the increase in the fracture height. After some point a further increase in the fracture height does not impact the strain magnitude. After the fracture passes the wellbore, the fracture height has very little impact on the middle of the wellbore (the direct contact region). Larger fracture height invokes a larger strain response on the wellbore sections far away from the hydraulic fracture (greater than 40 m) and a smaller strain response on the wellbore sections closer to the hydraulic fracture (less than 40 m).

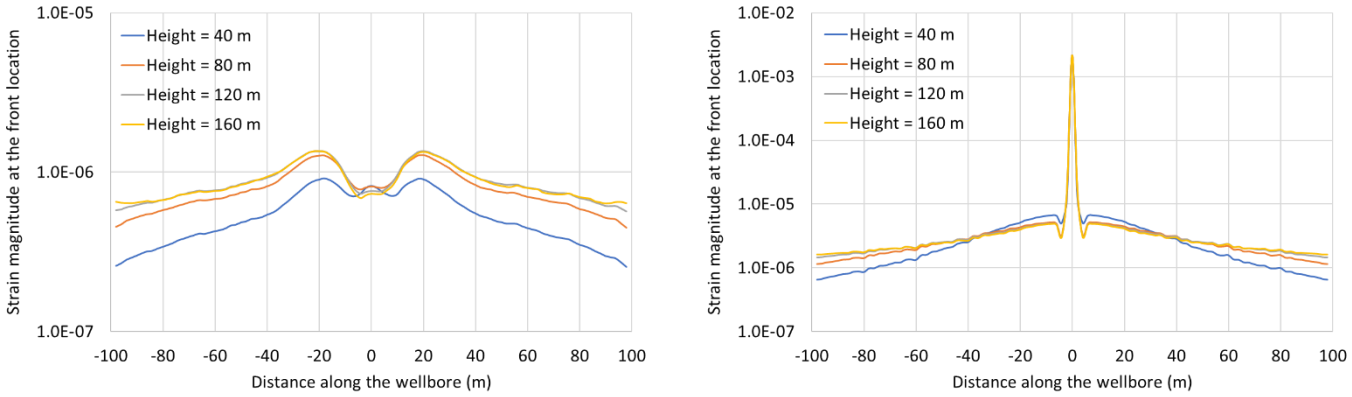

Figure 96. Monitored strain magnitude at the front location of the wellbore for different fracture height. Fracture width is fixed at 0.5 mm. (a) Fracture tip is 20 meters away from the wellbore. (b) Fracture is 20 meters past the wellbore.

Summary of Azimuthal Strain Methods

A novel fracture diagnostic method using azimuthally resolved downhole strain measurements and pressure monitoring in an offset observation well is presented in this chapter. Simulating fracture propagation from the treatment well and finely meshing the monitoring wellbore within the same mesh allows us to compute the strain and pressure change within the monitor wellbore accurately as a function of time. The pattern of the azimuthally resolved casing strain tensor in time and space is closely related to the evolving fracture geometry. The radial and longitudinal strain at different measuring points allows a characterization of changes in wellbore shape and ovality when facing approaching hydraulic fractures. These measurements together with the wellbore pressure response can then be interpreted to obtain the timing of frac-hits, the fracture geometry, and the cluster efficiency. This novel 3-D fracture diagnostic method can help operators better interpret the measured casing strain tensor and the sealed wellbore pressure data. Such a diagnostic method opens the possibility of real-time fracture diagnostics and optimization.

Chapter 6. Implementation of a Dashboard for Near Real -Time Fracture Diagnostics and Data Interpretation

The combination of increased activity in unconventionals, improving gauge technology, and the capability to stream data from the field to the office encourages a platform for real time monitoring and optimization. There are various service providers that provide streaming services to live databases from location, with the most common being pressure sensors. Figure 97 displays a hypothetical workflow for how a real time setup could be achieved and the interrelations from the field to the office. First the live streaming data is tested to ensure data transmission; next, an observation of pressure or strain can be measured and fed to an analytical modeling system that utilizes efficient equations that will be developed from the wellbore strain work discussed previously. The code/platform/dashboard would then interpret the signals utilizing a host of methods to develop a realization of fracture geometry and potentially a recommendation for the user to implement in the active stimulation. The platform would continue to monitor the pressure/diagnostic signals to validate a change in growth or geometry and continue to make near-real time estimates of fracture propagation based on offset well responses. This section reviews the techniques and design of a dashboard for near real time fracture diagnostics.

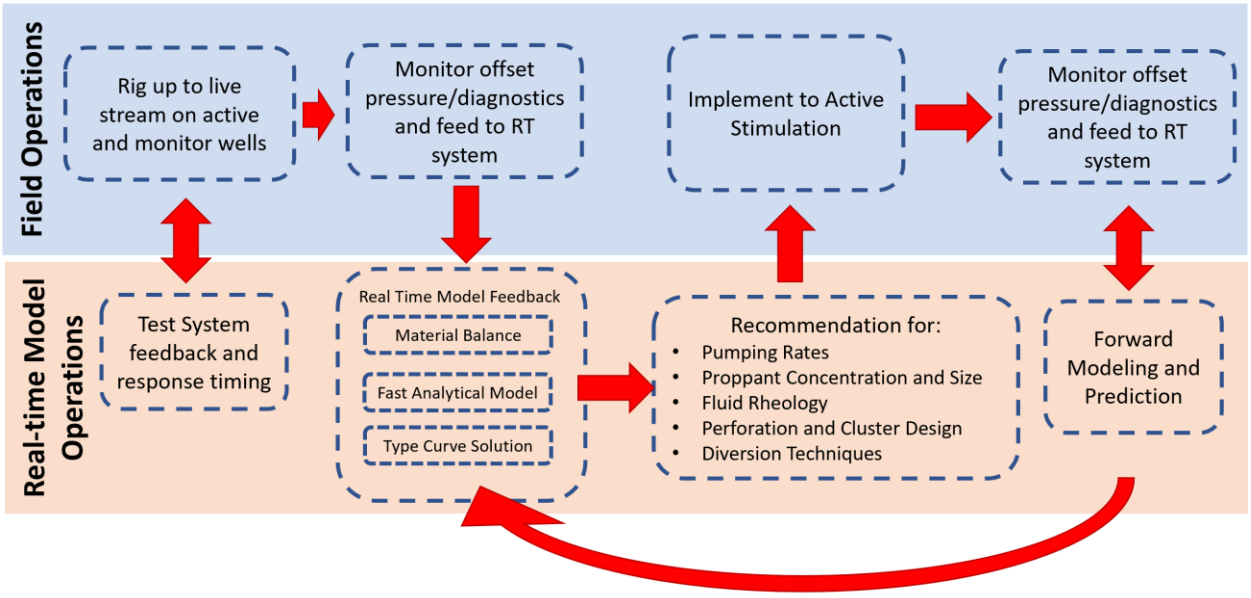

Figure 97: Real time implementation workflow

6.1 DEVELOPMENT OF A FRACTURE DIAGNOSTICS DASHBOARD

Before any discussion of a real time effort can be made, a platform that integrates the wellbore surveys, the individual well stage details, the pumping data, and offset pressure monitoring data must be created. This platform serves the purpose to not only visualize the various wellbore diagnostics and interpretations, but also serves as a method to track, data warehouse, analyze and make decisions on design changes based on the observed responses.

Several key items were identified early in the scoping process from prior experience in the industry. The platform must be visually appealing, interactive, and include a streamlined data input and processing workflow to be a functioning tool for industry use. The platform must also me highly customizable for the user, as workflows in the fracture diagnostic space are changing at a rapid pace. Given these considerations, a Python-based tool was developed utilizing PLOTLY DASH (Plotly Technologies Inc, 2022) and deployed for users via PythonAnywhere web hosting.

Figure 98 displays the platform architecture and how data enters and exits the dashboard. The dashboard itself is agnostic to input sources, and can use static data files, or stream from an API. All of the processing is handled by the code, which first conditions data then displays the surveys and pressure charts. Next the code will automatically compute the fracture driven interaction and associated depletion geometries. Finally, the platform displays summary data and generates any plots and figures that can be used in the current viewer, or in some other third-party system.

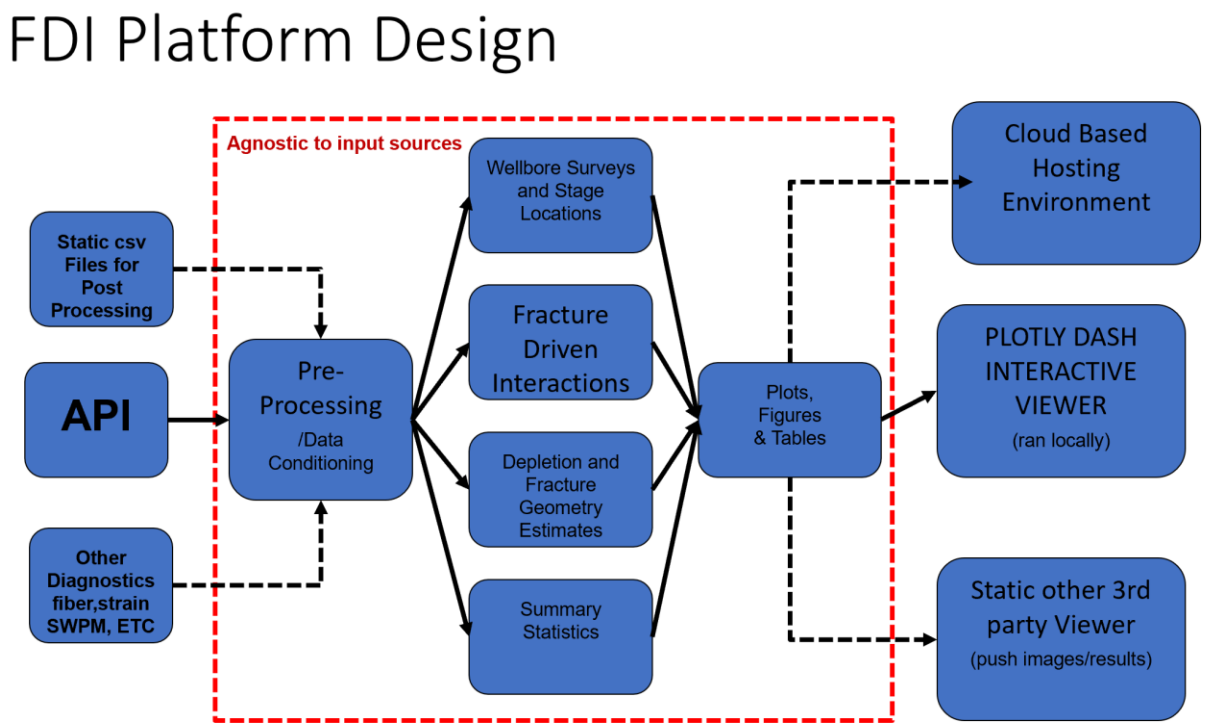

Figure 98: FDI Platform Design Flow Chart

Overall Design and User Workflow

Plotly Dash is the framework used to create the interactive web-based application. Python is used in this work, although Dash can also be used with Julia and R. Matplotlib plotting library was

initially used for the dashboard visuals, but a migration to Plotly graphing library was made because of the robust interactive components. Each graph supports zooming, panning, draggable data selection, and image capture, and the 3-D plots support orbital rotation in addition. Though not employed currently, authentication measures can be included using Dash.

The learning curve for using Dash is minimal for those familiar with programming and proficient in Python, allowing future students to continue and advance the project. For those with web development experience, customizing the layout of the dashboard is extremely easy.

The Dash documentation is extensive and user-friendly. There are both enterprise and open source versions of Dash available, and the open source option and the framework's popularity has led to broad community forums. Dash apps can be deployed on servers that support Flask app deployment, which includes most major cloud providers. Dash OpenSource is used here, and the app is deployed using PythonAnywhere.

6.2 FRONT END DESIGN

The app is composed of three user interfaces: (1) user input form, (2) advanced graphical analytics, and (3) contextualizing graphics.

The user input form accepts tabular data drag-and-dropped by the user or alternatively uploaded via windows explorer navigation (Figure 99). The upload code is quite nimble so as not to be overly restrictive with data formatting. Survey and stage data files are checked for completeness, and any wells that meet all criteria are included as optional dropdown menu items to be selected as the treatment well or as the monitor well. The timeseries data channels of interest are identified by the user from dropdown menus populated with timeseries data file column names. The key timeseries data that is required for the workflow are treatment and monitor well pressure, treatment rate, stage volume, and treatment stage number.

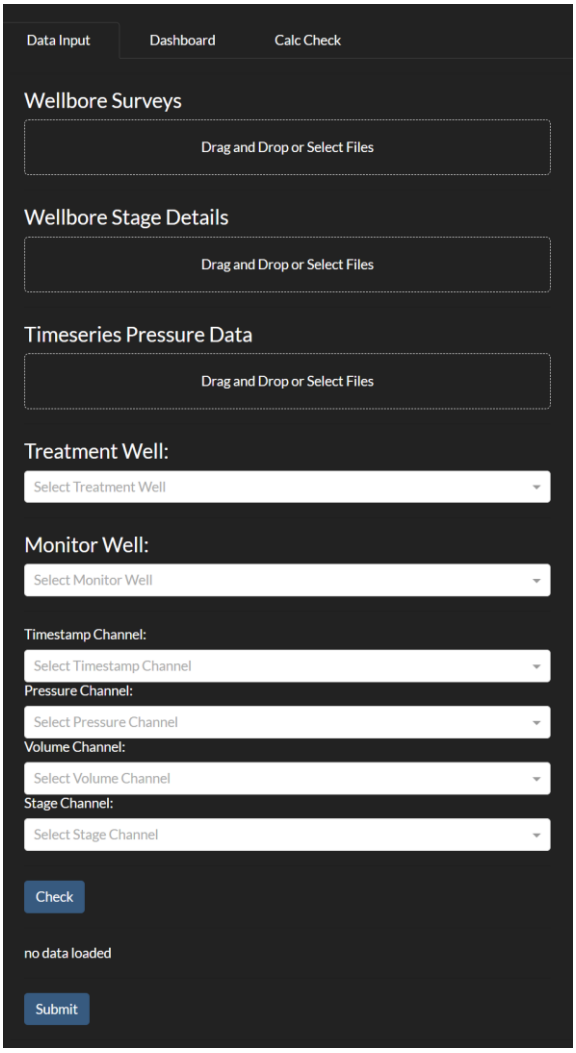

Figure 99: Dashboard Data Input Screen

After uploading the files and selecting each channel, a 3-D plot of all wellbores included in the survey file and a line chart of the timeseries pressure data are populated. These simplified plots allow the user to check that the correct files and channels were uploaded before moving forward with the analysis. Similar (but more informative and complex) charts to these will populate the next tab (Figure 100).

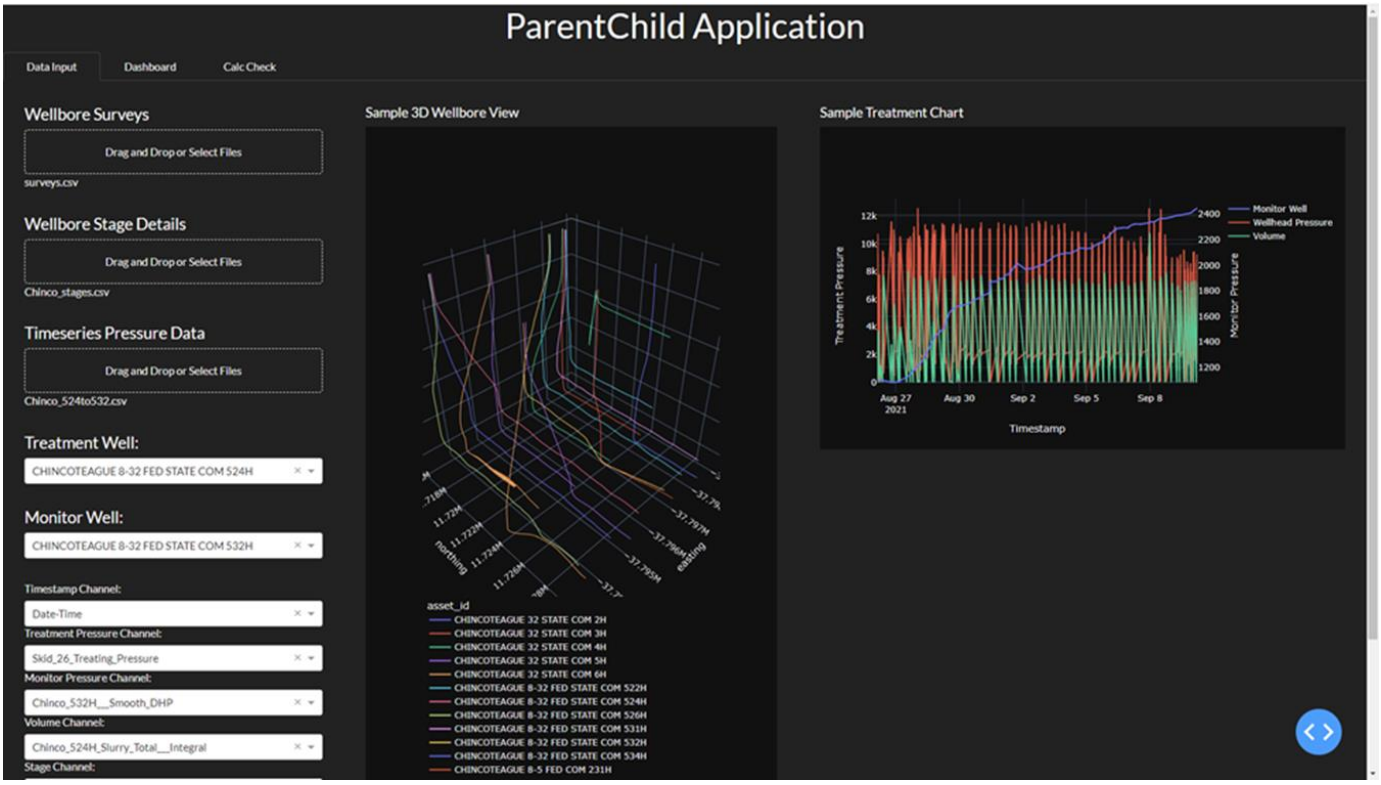

Figure 100: Parent Child Application Data Input Screen

The "Dashboard" tab houses three items which visually display the backend calculation results and enable real time or post-job diagnose and analysis (Figure 101). The first visual is the 3-D wellbore view with fracture area ellipses plotted along the treatment, or child, well and any depletion area ellipses plotted along the corresponding monitor, or parent, well. These calculations will be further discussed in the backend section. The second visual is the stage-by-stage line plot of timeseries data. The chart has all the previously mentioned user interaction options and additionally allows for drop down selection of a single stage to filter the plotted data. Finally, the calculated pressure response magnitude and VFR values for each stage are shown tabularly along with the corresponding response type classification.

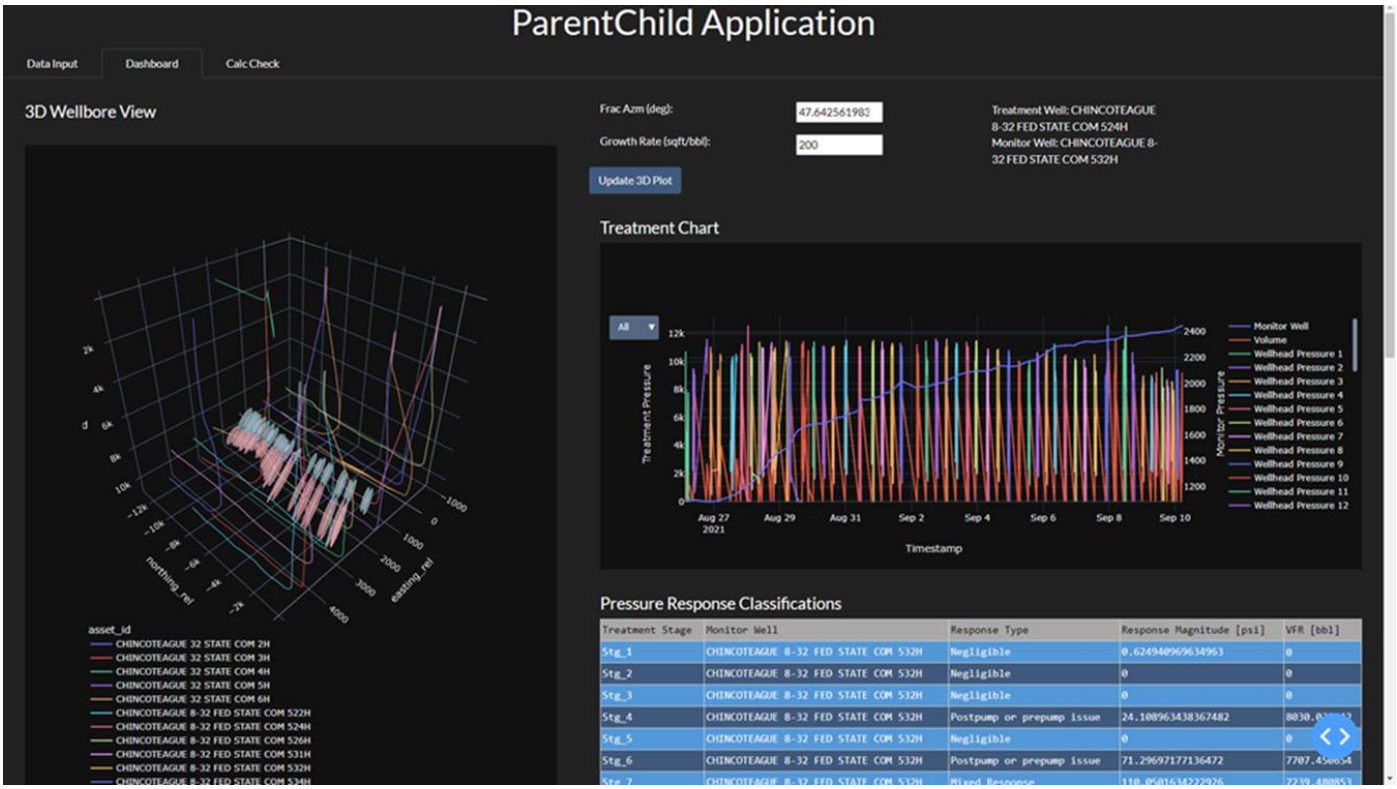

Figure 101: Dashboard Tab of Application with Fractures and Results Table Visualized

The third tab displays column charts for calculated VFR, fracture length, and depletion length for each stage (Figure 102). These charts allow the user to visualize the variation in the stage results for the properties of volume to first response, frac length, depletion length. These are the main outputs of the workflow and are critical for the diagnosis of depletion volume and new fracture infill growth. This table is used for summary reporting or new updates as additional data comes into the tool. Bar charts like this allow the user to quickly interpret fracture asymmetry, heel biased growth, or anomalous stages very quickly.

Figure 102: Third Tab Example Displaying Summary of Results

6.3 BACKEND DESIGN

Wellbore Survey and Well Distance Math

Wellbore distances from stage to stage are very important for the fracture geometry inversion in this method. The technique simplifies the wellbore survey into Northing, easting components (in feet), this ensures that the computed geometry and distances from wells are all aligned. If northing and easting values are not provided, these values are calculated from the latitude and longitude values. Since northing and easting values are in units of feet, they are better location descriptors to plot, from a user experience point of view, and more commonly used in industry. The survey plot on the "Data Input" tab plots the uploaded wellbores in 3-D using northing, easting, and true vertical depth. After the treatment well is selected on this tab, relative distances of each wellbore can be calculated. These are the values that a user would likely be

familiar with, i.e. Wells A, B, and C should have 400 ft spacing. The 3-D wellbore plot on the "Dashboard" tab uses this relative distance from the treatment well on the x and y axes to further improve the utility of the plot.

The timeseries data is cleansed and labeled as per the user selected well and channel names. For each stage, as labeled in the timeseries data, a start time is assigned by finding the first timestamp where the stage's slurry volume is greater than 10 bbl, and an end time is assigned at the last timestamp where wellhead pressure is greater than 8,500 psi. This criterion has worked well for all treatment wells thus far, but in the future more robust identification methods could be implemented, if needed.

Derivative Math to Auto-pick Responses and Identify Types

A pre-pump period is defined as the 45 seconds before the start time. The slope of this pre-pump monitor well pressure data is extrapolated, and the pressure delta is computed. Taking the derivative of the monitor pressure curve allows for an automatic pick of the volume to response. After various iterations of these computations, it was found that the second derivative local maximum is the most consistent and widely applicable methods to automatically identify a response. Various other threshold techniques can be deployed based on signal variability and data smoothness. This method can be seen in Seth et al. (2019) and Seth et al. (2020).

A post-pump period is defined as the 15 seconds after the calculated stage end time. After the volume to first response is automatically identified, the pre-pump pressure trend is extrapolated to the post-pump period, where a total delta pressure is computed from the stage response. After the delta is computed, we use curve recognition techniques to label the response type based on the post pumping behavior of the fracture driven interaction signature. The responses computed can

be seen in the following table and the logic and methods used can be found in Seth et al. (2019), Seth and Elliott, (2020).

The implementation method from Seth, has been included in the dashboard and has been enhanced through several iterations of the platform. A sample result can be seen in Figure 103. Each dashed vertical white line represents the time and volume of the response picked on the monitor well pressure trend. This identified volume to first response varies stage to stage and is identified and tracked as the key parameter that is then used to quantity fracture geometry. As mentioned before a specialized derivative technique is used to magnify the rate of change of the pressure trend to capture the distinct inflection. The user should tune this threshold to capture varying signatures and response types, for example SWPM signatures are several orders of magnitudes smaller than parent-child frac hit data, and need a more tuned derivative threshold. Once the pick of the fracture interaction is made, the total slurry volume pumped to that event is referenced and stored in the dataframe.

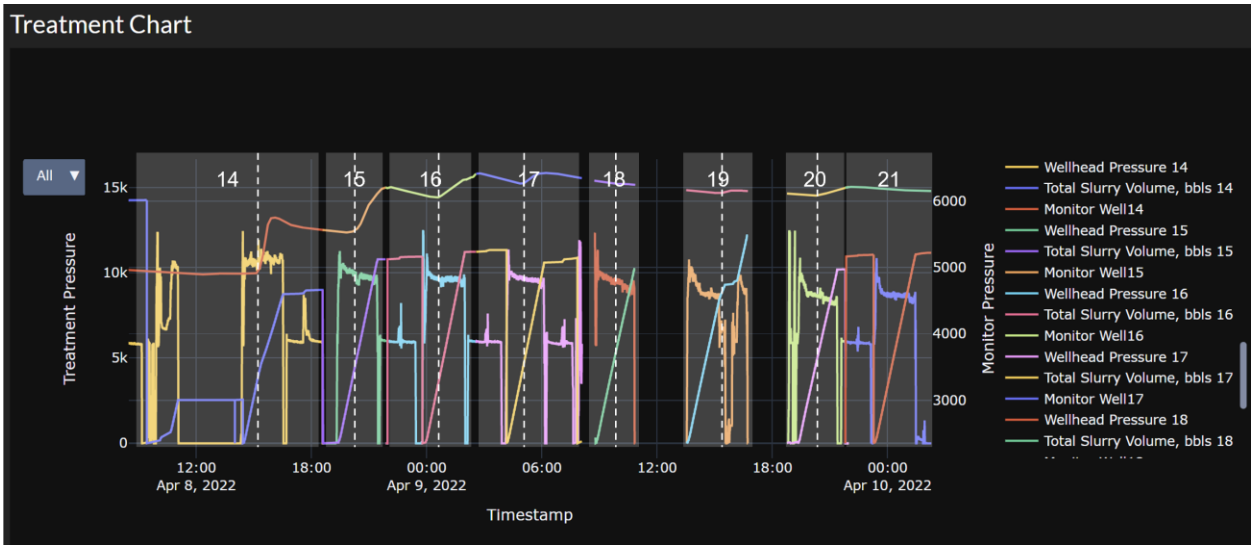

Figure 103: Example treatment stages with the volume to first response occurrence time annotated for each stage.

Lastly, a table of the pressure diagnostic results is computed and rendered in the front end of the dashboard. A sample table is seen in Figure 104, which summarizes the automatically

computed results in an easily digestible format, displaying the response type, response magnitude, and the VFR for each stage. If no response is observed, a flag of "Negligible" is recorded for that stage.

Pressure Response Classifications

Treatment Stage	Monitor Well	Response Type	Response Magnitude [psi]	VFR [bbl]
Stg_1	Chinco_532H___Smooth_DHP	Negligible	0.624940969634963	0
Stg_2	Chinco_532H___Smooth_DHP	Negligible	0	0
Stg_3	Chinco_532H___Smooth_DHP	Negligible	0	0
Stg_4	Chinco_532H___Smooth_DHP	Postpump or prepump issue	24.108963438367255	8030.032842
Stg_5	Chinco_532H___Smooth_DHP	Negligible	0	0
Stg_6	Chinco_532H___Smooth_DHP	Postpump or prepump issue	71.29697177136472	7707.450654
Stg_7	Chinco_532H___Smooth_DHP	Mixed Response	110.05016342229192	7239.480853
Stg_8	Chinco_532H___Smooth_DHP	Mixed Response	69.86619731386031	7477.476689
Stg_9	Chinco_532H___Smooth_DHP	Mixed Response	32.02432253246684	3487.065292
Stg_10	Chinco_532H___Smooth_DHP	Mixed Response	25.76461340701553	7640.453826
Stg_11	Chinco_532H___Smooth_DHP	Mixed Response	6.009842331114896	1773.375128
Stg_12	Chinco_532H___Smooth_DHP	Mixed Response	3.6368629850546768	6500.694235
Stg_13	Chinco_532H___Smooth_DHP	Negligible	0	0
Stg_14	Chinco_532H___Smooth_DHP	Mixed Response	12.259253483945031	6740.147568
Stg_15	Chinco_532H___Smooth_DHP	Mixed Response	81.88105743376855	2226.538529
Stg_16	Chinco_532H___Smooth_DHP	Mixed Response	14.01344899397327	5515.518142
Stg_17	Chinco_532H___Smooth_DHP	Negligible	0	0
Stg_18	Chinco_532H___Smooth_DHP	Mixed Response	17.980997508941755	2771.056025
Stg_19	Chinco_532H___Smooth_DHP	Mixed Response	12.453639370922701	3961.484667
Stg_20	Chinco_532H___Smooth_DHP	Mixed Response	9.48360485291255	2715.539387
Stg_21	Chinco_532H___Smooth_DHP	Mixed Response	3.0217542361135656	2553.986322
Stg_22	Chinco_532H___Smooth_DHP	Mixed Response	3.6020089412181733	807.9606049
Stg_23	Chinco_532H___Smooth_DHP	Mixed Response	12.959062392677424	5784.034658
Stg_24	Chinco_532H___Smooth_DHP	Negligible	0	0
Stg_25	Chinco_532H___Smooth_DHP	Mixed Response	2.781597511376276	127.3411905
Stg_26	Chinco_532H___Smooth_DHP	Mixed Response	2.4592603085134215	2466.663747
Stg_27	Chinco_532H___Smooth_DHP	Negligible	0	0
Stg_28	Chinco_532H___Smooth_DHP	Negligible	0	0
Stg_29	Chinco_532H___Smooth_DHP	Negligible	0	0

Figure 104: Table of fracture responses

A treatment well fracture azimuth is calculated as the angle perpendicular to the lateral's as-drilled direction. This value appears in the front end after calculation and can be edited by the user if desired. Likewise, an initial growth rate of 200 ft^2/bbl is used, but this value can be edited by the user. It should be noted that the growth rate can range in the varying unconventional plays

but with diligent measurements an operator can quickly develop a catalogue and range of estimates that generally represent fracture growth rates in each specific area.

Parent Child Geometry Calculations

To calculate values needed to plot the fracture and depletion ellipses, the locations of each stage are interpolated along the well. The fracture length is computed using Equation 6 (as seen and described in chapter 5).

$$L = \sqrt{\frac{GR}{\pi} * VFR} \qquad \text{Eq . 6}$$

An ellipse at the given stage depth with a major radius equal to fracture length is rotated to be oriented along the fracture azimuth. Three points on the ellipse are defined: one at the stage's measured depth along the wellbore, another at the tip of the fracture, and a third at the bottom of the ellipse. A vector V_{12} is calculated using the first two points and another V_{13} using the first and third points. The cross product of these vectors defines the normal vector, which should mirror the wellbore passing through the ellipse (Figure 105).

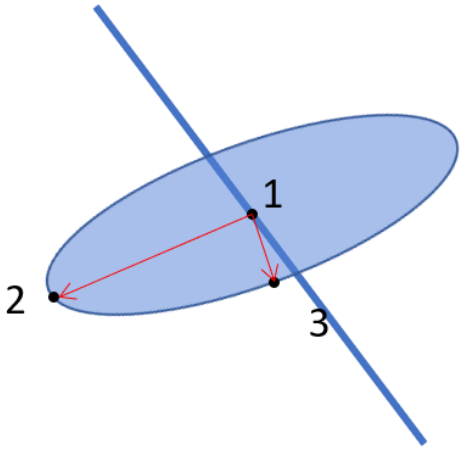

Figure 105: Three Points on ellipse to define the shape of displayed fractures

A check is performed to see if the plane intersects the monitor well between any two consecutive survey points along the lateral. If an intersection point exists, the distance between the treatment well and the intersection point is calculated. A depletion ellipse is drawn at the location of intersection along the monitor well with a major radius equal to the difference in well-to-well distance and fracture length, also along the fracture azimuth (Figure 106). If the treatment stage does not intersect the monitor well anywhere along the lateral, no well-to-well distance is calculated, and no ellipse is drawn. The new fracture growth (on azimuth) before it intersects the depleted fracture region is displayed in blue, while the approximate depleted fracture network is represented in red. For the case below we interpret new fracture growth in undepleted rock to be in the range of 600-800 ft, while the depleted region is approximated at 200-400ft. This intersection identified by the yellow dashed line is the likely extent of the depleted SRV from the parent well. The final interpreted values account for the wellbore and stage geometry, the fracture pumping time and volume, rates, clusters, as well as the parent well response time, volumes, and magnitudes to make this final realization. As can be seen, this is a very useful result supported by physical field measurements and backed by the various techniques and processes displayed in this dissertation. The operator or user can quickly evaluate varying depletion trends along the lateral, the efficiency of multiple infill stimulation designs, and the impact of well spacing on parent child frac hit frequency, timing and magnitudes.

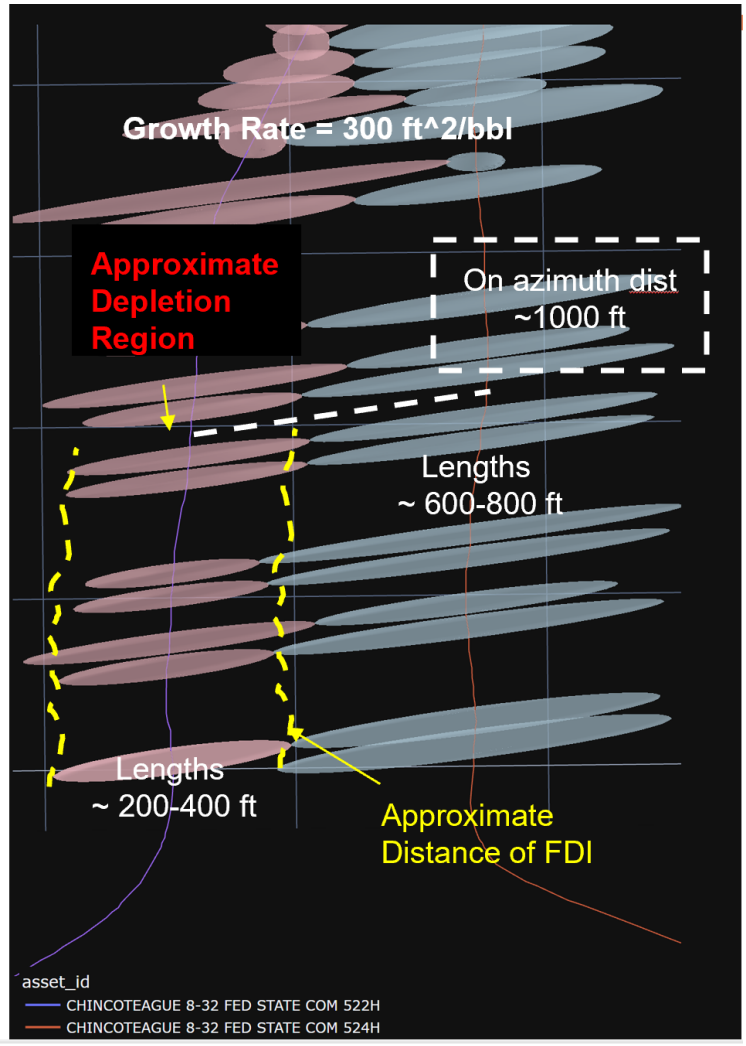

Figure 106: Example result displaying depletion region (red) and new fracture growth (blue)

6.4 Field Use case of Dashboard (Fault Identification)

Project description and background

The Dashboard was deployed in the Austin Chalk play in Texas. Fracturing data from the third well drilled by the operator was interpreted and the pressure responses processed through the interactive dashboard described above. The 2H wellbore, was drilled about 6000 ft to the west of

the 1H wellbore and was fracture stimulated, while the surface pressure response was monitored in the 1H.

Project details and interpretation

Prior to the start of fracturing the 2H wellbore, the 1H wellbore had a high resolution surface pressure gauge installed on the wellhead to monitor any fracture driven interactions from the 2H stimulation. The overall treating pressure and resulting monitor wells response can be seen in Figure 107. The blue color displays the treatment stages on the active well while the orange curve is the parent well pressure response. Note these wells are 6000 ft away and major communication was not expected, but was necessary to monitor for future infill development planning.

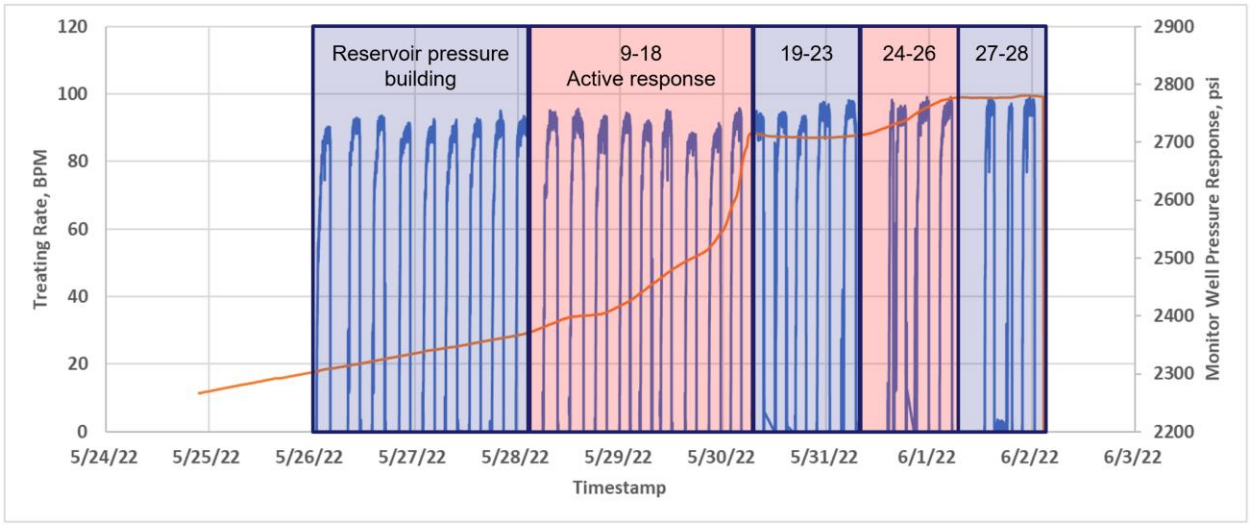

Figure 107: Fracture Stage treating rate on 2H and offset Pressure responses on 1H

As can be seen the response magnitude built to 2390 psi before any offset responses were observed on the parent well. Then through stages 9-18 the pressure built up to 2750 with several distinct inflections indicating fracture interactions from the offset treatment. Stages 19-23 were flat with little to no interactions, and again during stages 24-26 there were additional responses from the fracture treatment. This behavior was interpreted with the dashboard, the resulting spatial image

and pressure plot can be seen in Figure 108. New fracture geometry can be seen in light blue on the 2H wellbore. A large red line is approximating the 70 deg fracture azimuth in the area, and as can be seen is in good alignment with the toe of the parent wellbore around stage 9, where the first high confidence fault was interpreted and picked for the active well during drilling.

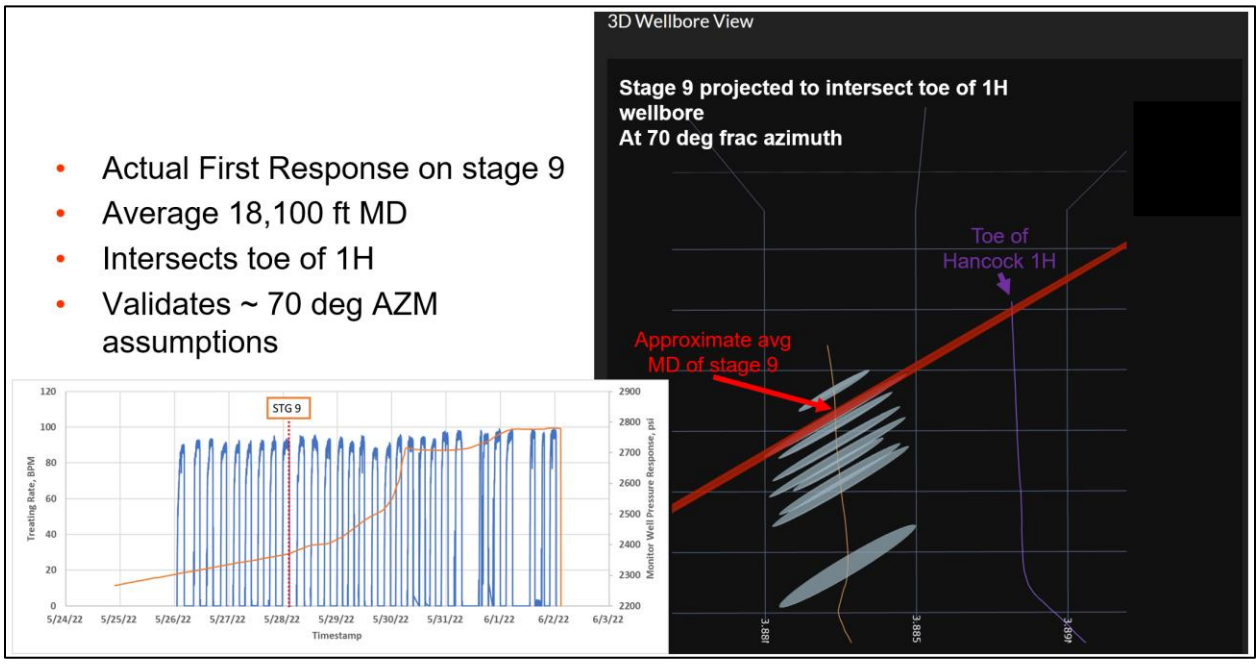

Figure 108: Dashboard image of 1H and 2H wellbore with First active stage and fracture azimuth identified

While reviewing the subsequent interpretation the team was concerned about the variability of the fracture signatures and the gaps in the interpreted responses. Upon further investigation and through the integration with the geology team, we were able to resolve a distinct relationship with the interpreted faults from the geosteering of the well. The geosteering interpretation can be seen in Figure 109 which displays the faults as large vertical red lines and calls out the measured depths along the horizontal wellbore and approximates the stage number. These features align very well with the larger pressure inflections on the parent well indicating that these regional are more likely to be fracture driven interactions from child well to parent well, or possibly a reactivated fault systems between the wells. Crossing these faults also resulted in substantial gas flares during

drilling and these ecorrelate very well with the fault picks and the pressure signatures during fracturing the active well.

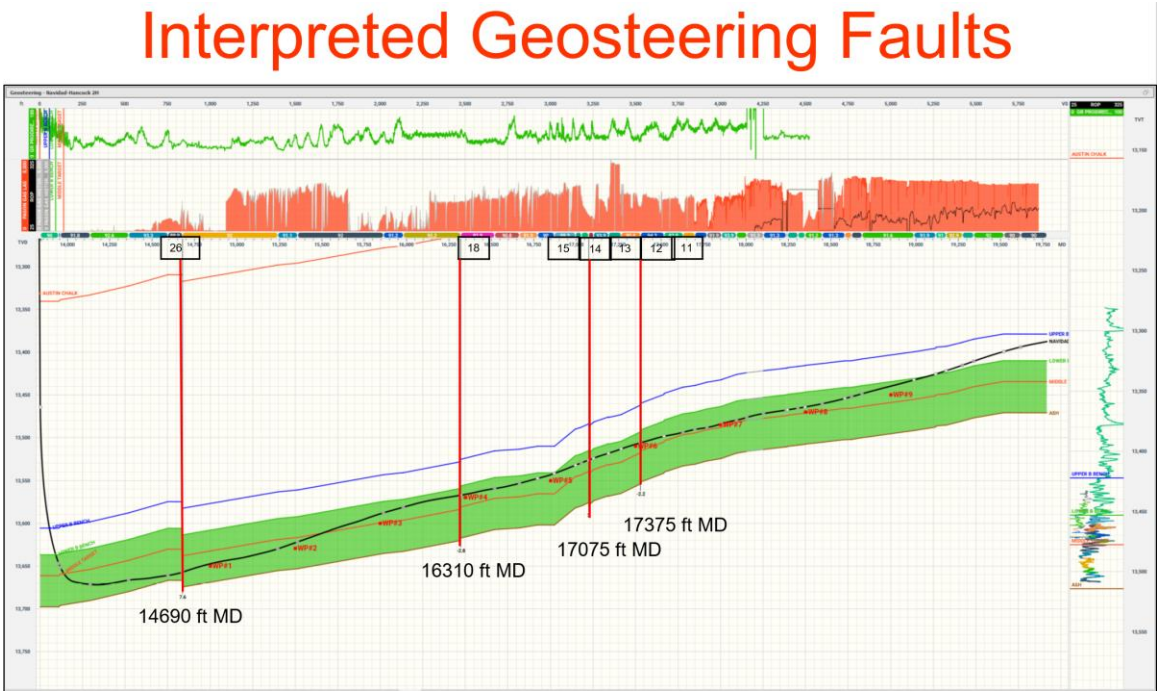

Figure 109: Interpreted Geosteering Faults on 2H wellbor

Using the dashboard the user can draw larger features which represent the fault systems between these wells. They are in good agreement where the interpreted pressure response shows activity we show faulting, and where we have quiet regions, there are little to no pressure responses or faults. This is displayed in Figure 110 below, with new fracture growth in blue and faults displayed in red. It should be noted that if fractures from the active well (2H) do not reach the monitor well (1H) that no interpretation can be made, thus the geometry can not be plotted, in which case the assumption made is the fracture did not reach the monitor or interact with other fracture systems that intersect the monitor well.

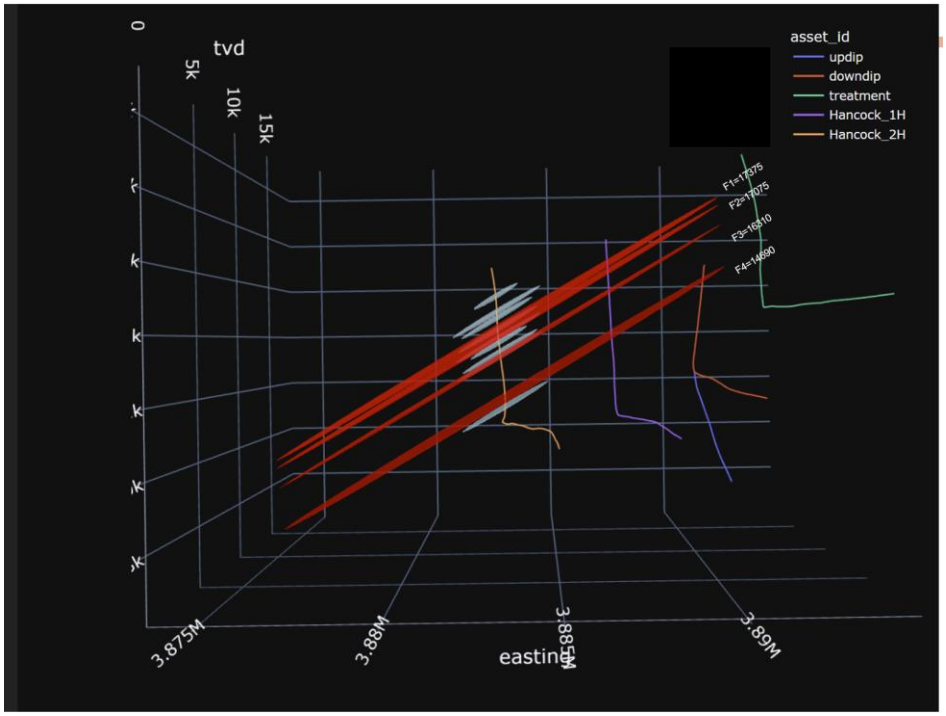

Figure 110: Dashboard display of new fracture generation and interpreted faults from geosteering reports

6.5 USE CASE OF DASHBOARD (DEPLETION REGION AROUND PARENT WELL)

This section investigates the technique to develop an estimated depletion geometry around a parent wellbore based on the offset pressure responses and fracture driven interactions between the well pair. This technique builds on previous research and numerical modeling in Chapter 5 and extends on previous work from Seth et. al. (2019), Manchanda et. al. (2018) , and Haffener et. al. (2022). This work was also presented at the Annual Hydraulic Fracturing and Sand Control Joint Industry project meeting from 2021 to 2024.

Project description and background case

The project setting for this case study is the Delaware basin Leonard/Avalon formation. Several existing parent wellbores were drilled and completed in the Brushy Canyon, Avalon Shale

and the 2nd Bone Spring Sandstone at the time of the study. The new infill wells were drilled in the Avalon B interval offsetting existing production by the 532H wellbore. For this case study the 532H wellbore will be considered as the Parent wellbore. The closest infill, the 524H will be considered the child wellbore. This study focuses on fracture driven interactions between these two wellbores. On the east side of the pad two monitor wellbores were used to calibrate the expected growth rates in this interval (P_522H and P532H). Since the eastern side of the section was not developed at the time, and the 534H, 526H, 522H, and 532H were all new child wells in virgin rock, the interactions specifically between the 526H and 522H could calibrate virgin growth rates for this section. It was determined that 200-500 ft^2/bbls were appropriate for the range of observations between the well pair. No interactions were observed on other parent wells in this unit, so only the 524H fractures growing toward the 532H parent wellbore are investigated here.

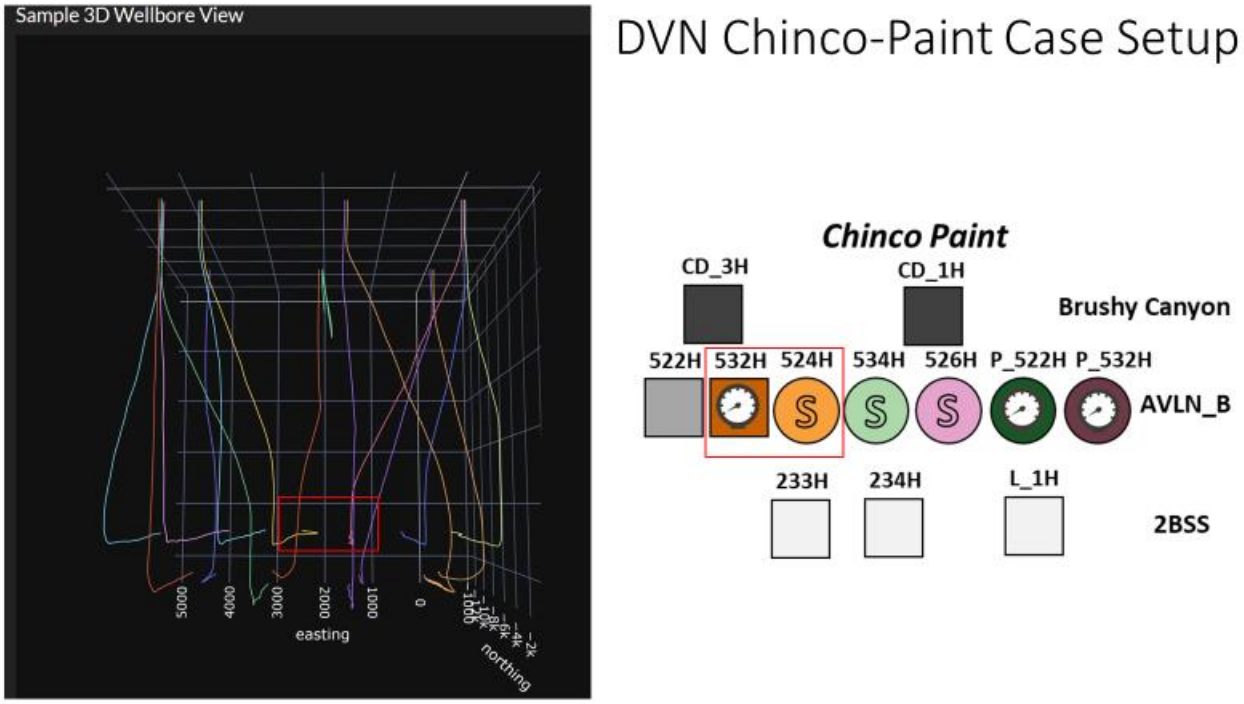

Figure 111: Devon Chinco-Paint Case Setup

Project details and interpretation

During the stimulation of the 524H, the surface pressure was monitored on the 532H wellbore. This provided the parent-child fracture interaction dataset for this study. As can be seen in Figure 112 the wellhead treating pressure of the infill child well range from 8000psi to 11,500 psi, and the monitor wellhead gauge shows readings from 1100 psi that build with nearly each progressive stage to over 2400 psi. The subtle pressure inflections will be interpreted here using the derivative threshold process described in chapter 5.

Figure 112: Treating Pressure and Monitor well response for 524H fractures intersecting the 532H wellbore

The Stimulation Design for these wells included a 10,000 bbls per stage volume of slickwater with 500,000 lbs per stage of proppant in 10 clusters for every stage. The volume design was expected to be large enough to interact with the parent well fracture system as seen from previous field experience. This project had the goal to characterize the parent well volume with detailed stage by stage analysis of the interpreted frac hit signatures.

Figure 113 displays the tabular summary of the interpreted response events using the dashboard and automated picking process. The response magnitudes and volume to First Response can be seen in the two far right columns. This show that the typical response volume from the infill child

well stimulation was on the order of 4500 bbls, and can range from 1773 to 8030 bbls. Note the lower volume responses (<1000 bbls) are far too quick for new fracture growth rates and are likely short circuit stages or communicating with the previous stage due to wellbore isolation issues.

Pressure Response Classifications

Treatment Stage	Monitor Well	Response Type	Response Magnitude [psi]	VFR [bbl]
Stg_1	Chinco_532H___Smooth_DHP	Negligible	0.624940969634963	0
Stg_2	Chinco_532H___Smooth_DHP	Negligible	0	0
Stg_3	Chinco_532H___Smooth_DHP	Negligible	0	0
Stg_4	Chinco_532H___Smooth_DHP	Postpump or prepump issue	24.108963438367255	8030.032842
Stg_5	Chinco_532H___Smooth_DHP	Negligible	0	0
Stg_6	Chinco_532H___Smooth_DHP	Postpump or prepump issue	71.29697177136472	7707.450654
Stg_7	Chinco_532H___Smooth_DHP	Mixed Response	110.05016342229192	7239.480853
Stg_8	Chinco_532H___Smooth_DHP	Mixed Response	69.86619731386031	7477.476689
Stg_9	Chinco_532H___Smooth_DHP	Mixed Response	32.02432253246684	3487.065292
Stg_10	Chinco_532H___Smooth_DHP	Mixed Response	25.76461340701553	7640.453826
Stg_11	Chinco_532H___Smooth_DHP	Mixed Response	6.009842331114896	1773.375128
Stg_12	Chinco_532H___Smooth_DHP	Mixed Response	3.6368629850546768	6500.694235
Stg_13	Chinco_532H___Smooth_DHP	Negligible	0	0
Stg_14	Chinco_532H___Smooth_DHP	Mixed Response	12.259253483945031	6740.147568
Stg_15	Chinco_532H___Smooth_DHP	Mixed Response	81.88105743376855	2226.538529
Stg_16	Chinco_532H___Smooth_DHP	Mixed Response	14.01344899397327	5515.518142
Stg_17	Chinco_532H___Smooth_DHP	Negligible	0	0
Stg_18	Chinco_532H___Smooth_DHP	Mixed Response	17.980997508941755	2771.056025
Stg_19	Chinco_532H___Smooth_DHP	Mixed Response	12.453639370922701	3961.484667
Stg_20	Chinco_532H___Smooth_DHP	Mixed Response	9.48360485291255	2715.539387
Stg_21	Chinco_532H___Smooth_DHP	Mixed Response	3.0217542361135656	2553.986322
Stg_22	Chinco_532H___Smooth_DHP	Mixed Response	3.6020089412181733	807.9606049
Stg_23	Chinco_532H___Smooth_DHP	Mixed Response	12.959062392677424	5784.034658
Stg_24	Chinco_532H___Smooth_DHP	Negligible	0	0
Stg_25	Chinco_532H___Smooth_DHP	Mixed Response	2.781597511376276	127.3411905
Stg_26	Chinco_532H___Smooth_DHP	Mixed Response	2.4592603085134215	2466.663747
Stg_27	Chinco_532H___Smooth_DHP	Negligible	0	0
Stg_28	Chinco_532H___Smooth_DHP	Negligible	0	0
Stg_29	Chinco_532H___Smooth_DHP	Negligible	0	0

Figure 113: Tabular Summary of the Interpreted Pressure responses from 524H stimulation to the 532H Monitor well

A commonly used technique in this workflow and dashboard is to visualize a range of fracture growth rates based on historical field observations of previous projects where this has been measured. Elliott et. Al. (2022), shows that varying fracture growth rates are affected by injection rate, rock mechanical properties, cluster efficiency and leakoff rates. Here the measured growth

rate or typical range is expected to be from 200-500 ft^2/bbl according to unpublished Devon field experience and previous studied in this specific area. Figure 114 shows the realization of fracture growth rates given that range of inputs, the blue fracture geometries represent the new fracture growth before entering the depleted area of the 532H parent monitor well, while the red geometries are the approximate distance of the depleted region around the Parent well. Note, these linear features are meant to be a guide and not an explicit description of the fracture geometry. This sensitivity gives the user guidance as to the possible depleted volume, and size of the conductive region of the parent well. As can be seen the lower growth rate (200 ft^2/bbl) , or slower propagation speed would yield the smallest new SRV stimulated and the larger depleted volumes, while the faster growth rate (500 ft^2/bbl) yields the largest new SRV and the smallest parent well depletion region.

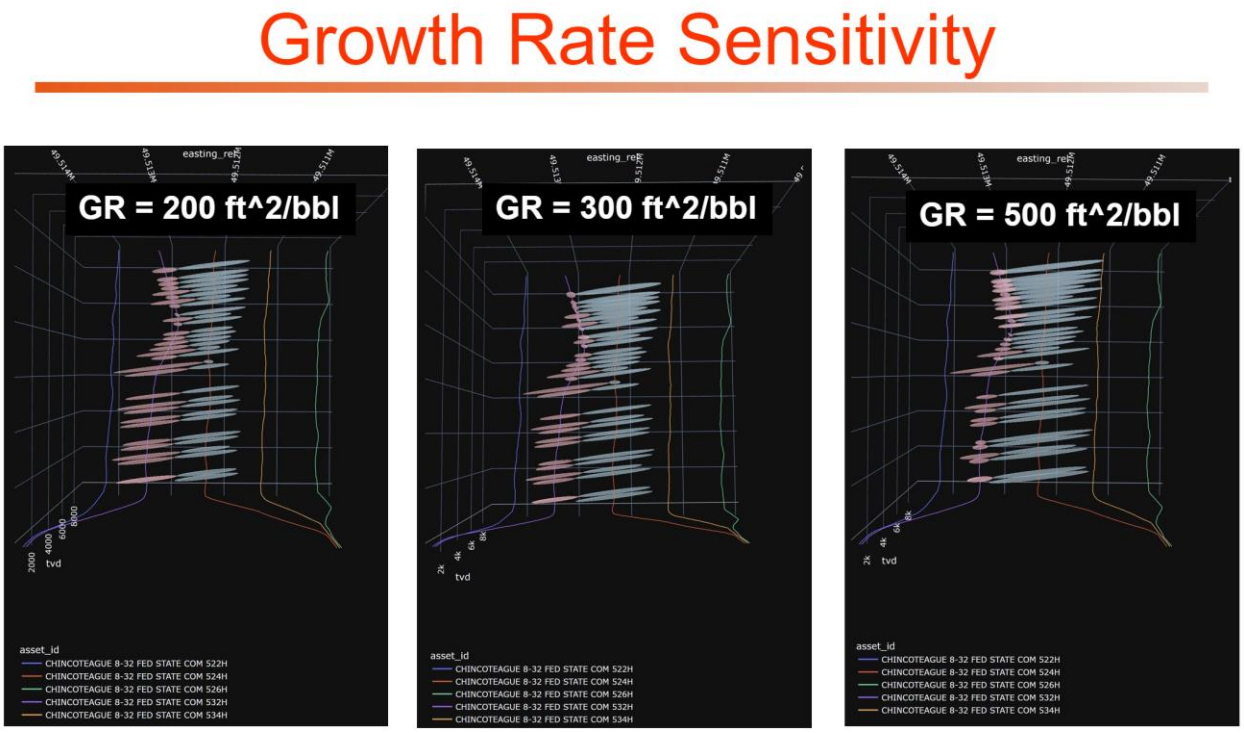

Figure 114: Growth Rate sensitivity and Inverted Fracture geometry realizations

Through several conversations with the operator and evaluation of prior project it was determined that the 300 ft^2/bbl was the most appropriate fracture growth rate to use for the final interpretation. Utilizing the 300 ft^2/bbl fracture growth in un-depleted rock yields a range of 600-800 ft, while the depleted region is approximated at 200-400ft. The region where these two fracture ellipses meet is the extend of the parent well depleted volume, or a 3 dimensional realization of where the frac hit event occurred and when the new fracture propagation was altered by the parent well volume. The final interpreted values account for the wellbore and stage geometry, the fracture pumping time and volume, rates, clusters, as well as the parent well response time, volumes, and magnitudes to make this final realization (Figure 115).

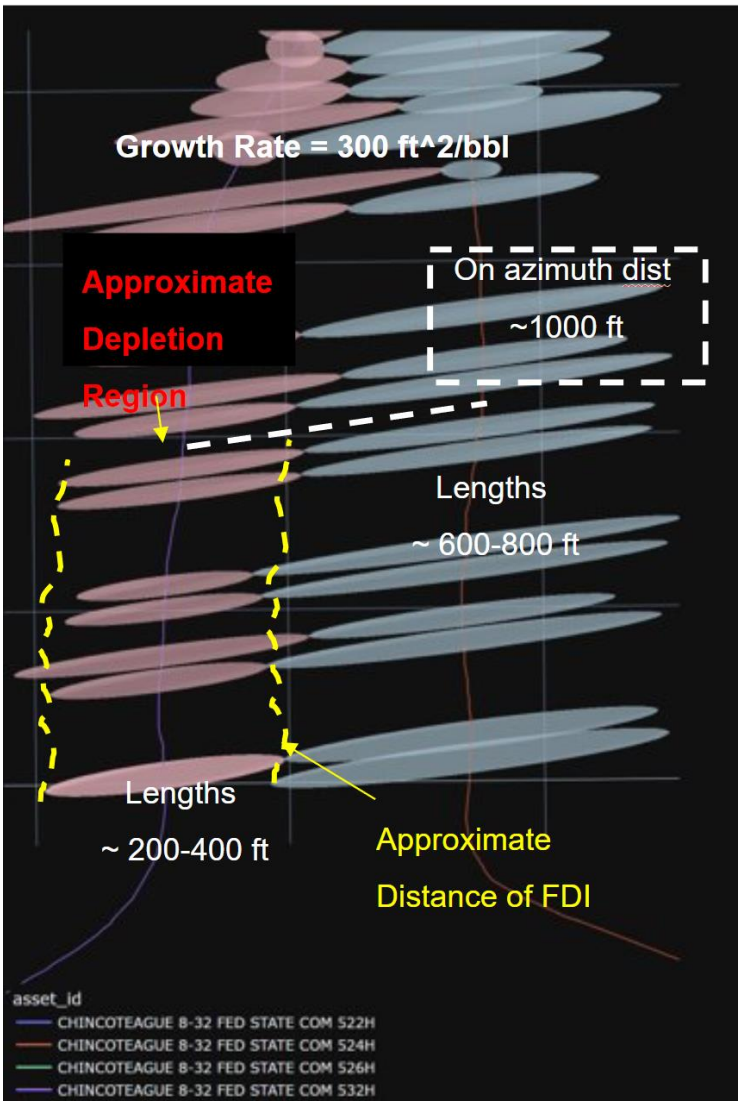

Figure 115: Detailed Summary of Final Interpreted Fracture geometries. New Fracture Growth (blue), depleted volume (red)

The final element of the dashboard is the results tab which displays the resulting Volume to First Response, the new fracture propagation length, and the approximate depleted length along the well by stage. As can be seen for this case in figure XX there is an average VFR of 4500 bbls, and each stage shows the representative dimension along the lateral as each unique fracture pressure inflection were interpreted wit the dashboard. These results help to inform the operator appropriate design volumes, stage architecture and perf efficiency. Finally a note on the computed depletion

distances shows a variable heel to toe depletion extrapolation. The first 20 stages show minimal drainage extents at the toe of the well while the heel portion shows a much larger drained region. This is quite common in unconventional wells, displaying a heel bais production profile.

Figure 116: Output values tab from dashboard displaying the summary data along the wellbore

Conclusions

As the industry approaches ever increasing complexity in unconventional development strategies, there will continue to be a necessity for a deep physical understanding of fracture mechanics with paralleled speed of interpretation and decision making. The goal of this work and dissertation was to utilize wellbore measurements and fracture diagnostics to optimize hydraulic fracturing. It was shown that utilizing fairly simple concepts like strain, and pressure, we can develop an enormous toolkit for fracture diagnostics and near real time optimization. Efficient analytical models and inversion solutions speed up multiple fracture shadow interpretations, and allow us to estimate height, length, and pressure of fractures. Coupled numerical simulations ran on supercomputers allows greater understanding of propagating fracture interactions on the wellbore in the subsurface. Those simulations were then validated with laboratory experiments on actual oilfield tubulars, and further matched with analytical displacement models. Those results enhanced our understanding of fracture propagation and allows a physical interpretation to the subsurface coupling of the formation and the wellbore during fracturing across a wide range of formation properties, pressures, and stimulation designs. Advancing the physics first observations from the numerical modeling this works displayed multiple techniques to interpret wellbore pressure data, casing deformation, and pipe ovality without complex numerical models. Finally, a novel dashboard was developed that allows the user to interpret these physical and readily observable pressure responses across the thousands of wells a year that are drilled and completed in the US and abroad. This innovative coupling of physics first fracturing fundamentals, along with analytical and numerical modeling, with novel thinking in advanced interpretations and practical dashboard tools is what makes this work unique. The techniques displayed are useful across multiple disciplines and sets

the foundation for the industry to utilize the wellbore as a key fracture diagnostic technology for the future.

References

Ajani, A. A., & Kelkar, M. G. (2012, January 1). Interference Study in Shale Plays. Society of Petroleum Engineers. doi:10.2118/151045-MS

Awada, A., Santo, M., Lougheed, D., Xu, D., & Virues, C. (2016, October 1). Is That Interference? A Work Flow for Identifying and Analyzing Communication Through Hydraulic Fractures in a Multiwell Pad. Society of Petroleum Engineers. doi:10.2118/178509-PA

Ballinger, Bradley, Green, Brett, Vajjha, Pavan, Haffener, Jackson, Edwards, Mark, Almasoodi, Mouin, and Kyle Haustveit. "Understanding the Hydraulic and Conductive Half Lengths in the Bakken/Three Forks Play – Coupling Sealed Wellbore Pressure Monitoring SWPM & Chow Pressure Group CPG." Paper presented at the SPE Hydraulic Fracturing Technology Conference and Exhibition, The Woodlands, Texas, USA, February 2022. doi: https://doi.org/10.2118/209144-MS

Barree, R. D., Miskimins, J. L., & Svatek, K. J. (2017, January 24). Reservoir and Completion Considerations for the Refracturing of Horizontal Wells. Society of Petroleum Engineers. doi:10.2118/184837-MS

Brinkley, Kourtney , Ingle, Trevor , Haffener, Jackson , Chapman, Philip , Baker, Scott , Hart, Eric , Haustveit, Kyle , and Jon Roberts. "An Eagle Ford Case Study: Monitoring Fracturing Propagation Through Sealed Wellbore Pressure Monitoring." Paper presented at the SPE Hydraulic Fracturing Technology Conference and Exhibition, Virtual, May 2021. doi: https://doi.org/10.2118/204140-MS

Chin, Adam, Miller, Patrick, Redpath, Darcy, Dauncey, Keane, Nakaska, Daniel, and Farhan Alimahomed. "Sealed Wellbore Pressure Monitoring in the Montney: Early Learnings." Paper presented at the SPE Canadian Energy Technology Conference, Calgary, Alberta, Canada, March 2022. doi: https://doi.org/10.2118/208921-MS

Cipolla, Craig, McKimmy, Michael, Hari-Roy, Stephanie, Wolters, Jennifer, Haffener, Jackson, Haustveit, Kyle, and Mouin Almasoodi. "Evaluating Stimulation Effectiveness with Permanent Optical Fiber and Sealed Wellbore Pressure Monitoring: Bakken Shale Case Study." *SPE Drill & Compl* 38 (2023): 146–154. doi: https://doi.org/10.2118/209129-PA

Daneshy, A. A., Au-yeung Jessica, Thompson, T., & Tymko, D. W. (2012, January 1). Fracture Shadowing: A Direct Method for Determination of the Reach and Propagation Pattern of Hydraulic Fractures in Horizontal Wells. Society of Petroleum Engineers. doi:10.2118/151980-MS

Daneshy, A. A., & Pomeroy, M. D. (2012, January 1). In-situ Measurement of Fracturing Parameters from Communication Between Horizontal Wells. Society of Petroleum Engineers. doi:10.2118/160480-MS

Daneshy, Ali. 2017. “Analysis of Front and Tail Stress Shadowing in Horizontal Well Fracturing: Their Consequences With Case History.” in *SPE Hydraulic Fracturing Technology Conference and Exhibition*. Society of Petroleum Engineers.

Daneshy, A. A. (2014, October 27). Fracture Shadowing: Theory, Applications and Implications. Society of Petroleum Engineers. doi:10.2118/170611-MS

Dawson, M., & Kampfer, G. (2016, August 1). Breakthrough in Hydraulic Fracture & Proppant Mapping: Achieving Increased Precision with Lower Cost. Unconventional Resources Technology Conference. doi:10.15530/URTEC-2016-2432330

Detournay, E. 2004. “Propagation Regimes of Fluid-Driven Fractures in Impermeable Rocks.” *International Journal of Geomechanics* 4(1):35–45.

Elliott, B. 2018 source data written up for the SPE fracture driven communication report, unpublished

Elliott, B., Manchanda, R., Seth, P., & Sharma, M. (2019, July 31). Interpreting Inter-Well Poroelastic Pressure Transient Data: An Analytical Approach Validated with Field Case Studies. Unconventional Resources Technology Conference. doi:10.15530/urtec-2019-449

Elliott, Brendan. “19HFTC Plenary Session Presentations.” *SPE Digital Assets: Collection Preview*, Society of Petroleum Engineeers, 5 Feb. 2019, spe.widencollective.com/c/yjgm9v1w.

Elliott, Brendan, Zheng, Shuang, Russel, Rod, Sharma, Mukul, Haustveit, Kyle, and Jackson Haffner. "Integration of Sealed Wellbore Pressure Monitoring Responses with Wellbore Strain and Deformation Measurements for Fracture Diagnostics." Paper presented at the SPE Hydraulic Fracturing Technology Conference and Exhibition, The Woodlands, Texas, USA, February 2022. doi: https://doi.org/10.2118/209120-MS

Gala, D. P., Manchanda, R., & Sharma, M. M. (2018, August 9). Modeling of Fluid Injection in Depleted Parent Wells to Minimize Damage Due to Frac-Hits. Unconventional Resources Technology Conference. doi:10.15530/URTEC-2018-2881265

Green, A. E. and I. N. Sneddon. 1950. “The Distribution of Stress in the Neighbourhood of a Flat Elliptical Crack in an Elastic Solid.” *Mathematical Proceedings of the Cambridge Philosophical Society* 46(01):159.

Haffener, Jackson, Haustveit, Kyle, and Trevor Ingle. "Did We Break New Rock? Utilizing Diagnostics to Differentiate New Fracture Creation vs Old Fracture Reactivation: A Meramec and Wolfcamp Study." Paper presented at the SPE Hydraulic Fracturing

Technology Conference and Exhibition, The Woodlands, Texas, USA, February 2022. doi: https://doi.org/10.2118/209123-MS

Haustveit, Kyle , Elliott, Brendan , Haffener, Jackson , Ketter, Chris , O'Brien, Josh , Almasoodi, Mouin , Moos, Sheldon , Klaassen, Trevor , Dahlgren, Kyle , Ingle, Trevor , Roberts, Jon , Gerding, Eric , Borell, Jarret , Sharma, Sundeep , and Wolfgang Deeg. "Monitoring the Pulse of a Well Through Sealed Wellbore Pressure Monitoring, a Breakthrough Diagnostic With a Multi-Basin Case Study." Paper presented at the SPE Hydraulic Fracturing Technology Conference and Exhibition, The Woodlands, Texas, USA, February 2020. doi: https://doi.org/10.2118/199731-MS

Haustveit, K., Dahlgren, K., Greenwood, H., Peryam, T., Kennedy, B., & Dawson, M. (2017, January 24). New Age Fracture Mapping Diagnostic Tools-A STACK Case Study. Society of Petroleum Engineers. doi:10.2118/184862-MS

N. Hummel, S. A. Shapiro, Microseismic estimates of hydraulic diffusivity in case of non-linear fluid-rock interaction, *Geophysical Journal International*, Volume 188, Issue 3, March 2012, Pages 1441–1453, https://doi.org/10.1111/j.1365-246X.2011.05346.x

Hwang, J., Szabian, M. J., & Sharma, M. (2017, July 24). Hydraulic Fracture Diagnostics and Stress Interference Analysis by Water Hammer Signatures in Multi-Stage Pumping Data. Unconventional Resources Technology Conference. doi:10.15530/URTEC-2017-2687423

Iriarte, Jessica , Hoda, Samid , Guest, Ryan , and Mary Van Domelen. "Turning a Breakthrough Technology into a Scalable Process: Sealed Wellbore Pressure Monitoring." Paper presented at the SPE Hydraulic Fracturing Technology Conference and Exhibition, Virtual, May 2021. doi: https://doi.org/10.2118/204193-MS

Jones E, Oliphant E, Peterson P, et al. SciPy: Open Source Scientific Tools for Python, 2001, http://www.scipy.org/ [Online; accessed 2019-04-26

Kampfer, Günther, D. Ph, Statoil Asa, Matthew Dawson, and D. Ph. 2016. “A Novel Approach to Mapping Hydraulic Fractures Using Poromechanic Principles.” *ARMA*.

King, G. E., Rainbolt, M. F., & Swanson, C. (2017, October 9). Frac Hit Induced Production Losses: Evaluating Root Causes, Damage Location, Possible Prevention Methods and Success of Remedial Treatments. Society of Petroleum Engineers. doi:10.2118/187192-MS

Kurtoglu, B., & Salman, A. (2015, November 9). How to Utilize Hydraulic Fracture Interference to Improve Unconventional Development. Society of Petroleum Engineers. doi:10.2118/177953-MS

Lawal, H., Jackson, G., Abolo, N., & Flores, C. (2013, June 10). A Novel Approach To Modeling and Forecasting Frac Hits In Shale Gas Wells. Society of Petroleum Engineers. doi:10.2118/164898-MS

Lawal, H., Abolo, N., Jackson, G., Sahai, V., & Flores, C. P. (2014, May 21). A Quantitative Approach to Analyze Fracture Area Loss in Shale Gas Reservoirs. Society of Petroleum Engineers. doi:10.2118/169406-MS

Lehmann, J., Budge, J., Palghat, A., Petr, C., & Pyecroft, J. (2016, February 1). Expanding Interpretation of Interwell Connectivity and Reservoir Complexity through Pressure Hit Analysis and Microseismic Integration. Society of Petroleum Engineers. doi:10.2118/179173-MS

Lindsay, G., Miller, G., Xu, T., Shan, D., & Baihly, J. (2018, January 23). Production Performance of Infill Horizontal Wells vs. Pre-Existing Wells in the Major US Unconventional Basins. Society of Petroleum Engineers. doi:10.2118/189875-MS

Lund Snee, Jens-Erik & D. Zoback, Mark. (2016). State of stress in Texas: Implications for induced seismicity. Geophysical Research Letters. 43. 10.1002/2016GL070974.

Mack, M. G., Taylor, S. M., Rich, J., Kahn, D., King, J., Schaeffer, B., … Biholar, A. (2017, August 7). Can Moment Tensor Inversion Aid Engineering Decisions? A Delaware Basin Case Study. Unconventional Resources Technology Conference. doi:10.15530/URTEC-2017-2693686

Manchanda, Ripudaman. 2015. “A General Poro-Elastic Model for Pad-Scale Fracturing of Horizontal Wells.”

Manchanda, Ripudaman, Shuang Zheng, Sho Hirose, and Mukul M. Sharma. 2019. “Integrating Reservoir Geomechanics with Multiple Fracture Propagation and Proppant Placement.” SPE Journal under review

Manchanda, R., Elliott, B., Seth, P., and M. M. Sharma. "Interpreting Inter-Well Poroelastic Pressure Transient Data: An Analytical Approach." Paper presented at the 53rd U.S. Rock Mechanics/Geomechanics Symposium, New York City, New York, June 2019.

Manchanda, R., Bhardwaj, P., Hwang, J., & Sharma, M. M. (2018, January 23). Parent-Child Fracture Interference: Explanation and Mitigation of Child Well Underperformance. Society of Petroleum Engineers. doi:10.2118/189849-MS

Martinez, R., Rosinski, J., & Dreher, D. T. (2012, January 1). Horizontal Pressure Sink Mitigation Completion Design: A Case Study in the Haynesville Shale. Society of Petroleum Engineers. doi:10.2118/159089-MS

Miller, G., Lindsay, G., Baihly, J., & Xu, T. (2016, May 5). Parent Well Refracturing: Economic Safety Nets in an Uneconomic Market. Society of Petroleum Engineers. doi:10.2118/180200-MS

Morales, A., Zhang, K., Gakhar, K., Marongiu Porcu, M., Lee, D., Shan, D., … Acock, A. (2016, February 1). Advanced Modeling of Interwell Fracturing Interference: An Eagle Ford Shale Oil Study - Refracturing. Society of Petroleum Engineers. doi:10.2118/179177-MS

Nordgren, R. P. 1972. “Propagation of a Vertical Hydraulic Fracture.” *Society of Petroleum Engineers Journal* 12(04):306–14.

Olson, Karen, Merritt, Joshua, Barraez, Rair, Fowler, Garrett, Haffener, Jackson, and Kyle Haustveit. "Sealed Wellbore Pressure Monitoring (SWPM) and Calibrated Fracture Modeling: The Next Step in Unconventional Completions Optimization." Paper presented at the SPE Hydraulic Fracturing Technology Conference and Exhibition, The Woodlands, Texas, USA, January 2023. doi: https://doi.org/10.2118/212367-MS

Perkins, T. K. and L. R. Kern. 1961. “Widths of Hydraulic Fractures.” *Journal of Petroleum Technology* 13(09):937–49.

Plotly Technologies Inc., “Dash Layout”, 2022, https://dash.plotly.com/layout

Ramirez, Alberto, Basic, Damir, Merritt, Josh, Olson, Karen, and Mary Van Domelen. "Automating a Breakthrough Technology for Real-Time Diagnostics: Sealed Wellbore Pressure Monitoring." Paper presented at the SPE Hydraulic Fracturing Technology Conference and Exhibition, The Woodlands, Texas, USA, February 2022. doi: https://doi.org/10.2118/209161-MS

Roussel, N. P. (2017, January 24). Analyzing ISIP Stage-by-Stage Escalation to Determine Fracture Height and Horizontal-Stress Anisotropy. Society of Petroleum Engineers. doi:10.2118/184865-MS

Roussel, N. P., & Agrawal, S. (2017, July 24). Introduction to Poroelastic Response Monitoring - Quantifying Hydraulic Fracture Geometry and SRV Permeability from Offset-Well Pressure Data. Unconventional Resources Technology Conference. doi:10.15530/URTEC-2017-2645414

Rainbolt, M. F., & Esco, J. (2018, January 23). Frac Hit Induced Production Losses: Evaluating Root Causes, Damage Location, Possible Prevention Methods and Success of Remediation Treatments, Part II. Society of Petroleum Engineers. doi:10.2118/189853-MS

Seth, Puneet, Ripudaman Manchanda, Ashish Kumar, and Mukul Sharma. 2018. “Estimating Hydraulic Fracture Geometry by Analyzing the Pressure Interference Between Fractured Horizontal Wells.” in *SPE Annual Technical Conference and Exhibition*. Society of Petroleum Engineers.

Seth, Puneet, Ripudaman Manchanda, Shuang Zheng, Deepen Gala, and Mukul Sharma. 2019. “Poroelastic Pressure Transient Analysis: A New Method for Interpretation of Pressure

Communication Between Wells During Hydraulic Fracturing." In SPE Hydraulic Fracturing Technology Conference and Exhibition. Society of Petroleum Engineers. https://doi.org/10.2118/194358-MS.

Seth, P., Shrivastava, K., Kumar, A. and Sharma M.M. 2019. Pressure Interference between Fractured Horizontal Wells: Impact of Complex Fracture Growth on Offset Well Pressure Measurements. Accepted for publication at the 53rd US Rock Mechanics/Geomechanics Symposium to be held in New York, NY, USA, 23–26 June 2019.

Seth, P., Manchanda, R., Elliott, B., Zheng, S. and Sharma M.M. 2019. Diagnosing Multi-Cluster Fracture Propagation Using Dynamic Poroelastic Pressure Transient Analysis. Accepted for publication at the Unconventional Resources Technology Conference to be held in Denver, Colorado, USA, 22-24 July 2019.

Seth, P., Manchanda, R., Elliott, B., Zheng, S. and Sharma M.M. 2019. Estimating Fracture Network Area and SRV Permeability by Analyzing Offset Well Pressure Measurements during Fracturing. Accepted for publication at the SPE Annual Technical Conference and Exhibition to be held in Calgary, Alberta, Canada, 30 September - 2 October 2019.

Shahri, Mojtaba , Tucker, Andrew , Rice, Craig , Lathrop, Zach , Ratcliff, Dave , McClure, Mark , and Garrett Fowler. "High Fidelity Fibre-Optic Observations and Resultant Fracture Modeling in Support of Planarity." Paper presented at the SPE Hydraulic Fracturing Technology Conference and Exhibition, Virtual, May 2021. doi: https://doi-org.ezproxy.lib.utexas.edu/10.2118/204172-MS

Shapiro, S. A., C. Dinske, and E. Rothert (2006), Hydraulic-fracturing controlled dynamics of microseismic clouds, *Geophys. Res. Lett.*, 33, L14312, doi:10.1029/2006GL026365.

Sneddon, I. N., The distribution of stress in the neighbourhood of a crack in an elastic solid187Proceedings of the Royal Society of London. Series A. Mathematical and Physical Sciences. http://doi.org/10.1098/rspa.1946.0077

Spicer, S., & Coenen, E. (2018, August 9). Estimation of Fracture Geometries From Poroelastic Pressure Responses in Offset Wells. Unconventional Resources Technology Conference. doi:10.15530/URTEC-2018-2886118

Ugueto, Gustavo, Wu, Kan, Jin, Ge, Zhang, Zhishuai, Haffener, Jackson, Mojtaba, Shahri, Ratcliff, David, Bohn, Rob, Chavarria, Andres, Wu, Yinghui, Guzik, Artur, Srinivasan, Aishwarya, Gibson, Richard, and Alexei Savitski. "A Catalogue of Fiber Optics Strain-Rate Fracture Driven Interactions." Paper presented at the SPE Hydraulic Fracturing Technology Conference and Exhibition, The Woodlands, Texas, USA, January 2023. doi: https://doi-org.ezproxy.lib.utexas.edu/10.2118/212370-MS

Warpinski, N. R., S. L. Wolhart, and C. a. Wright. 2004. “Analysis and Prediction of Microseismicity Induced by Hydraulic Fracturing.” SPE Journal 9(01):24–33.

Yu, W., Xu, Y., Weijermars, R., Wu, K., & Sepehrnoori, K. (2017, January 24). Impact of Well Interference on Shale Oil Production Performance: A Numerical Model for Analyzing Pressure Response of Fracture Hits with Complex Geometries. Society of Petroleum Engineers. doi:10.2118/184825-MS

Zhe, L., Younis, R., & Jiang, J. (2016, August 1). A Diagnostic Framework for Bashed; Wells in Unconventional Reservoirs: A Numerical Simulation and Model Selection Theory Approach. Unconventional Resources Technology Conference. doi:10.15530/URTEC-2016-2448463

Zheng, S., Manchanda, R., Sharma, M.M., 2019. Development of a fully implicit 3-D geomechanical fracture simulator. J. Pet. Sci. Eng. 179, 758–775. https://doi.org/10.1016/j.petrol.2019.04.065

Vita

Brendan Elliott is an Engineering Advisor at Devon Energy working in a corporate subsurface technology role. His main responsibilities include completion design and optimization, DFIT analysis, fracture diagnostics and complex multi-interval planning. Currently focused in the Delaware Basin, developing multiple stacked pay intervals and leads a subsurface technical team to investigate depletion mitigation and fracture interference. Brendan also works alongside Devon's Business development and New Energy Ventures groups to evaluate new technologies and methods in expanding our energy future. Brendan holds a BS in Petroleum Engineering from Texas A&M University, and MS from the University of Texas, and is finalizing PhD at the University of Texas. During his time at UT Austin, he was lead or co-author on 16 technical papers and won SPE Hydraulic Fracturing Technical Session Outstanding Graduate Student in 2023.

Permanent contact email <Brendan07elliott@gmail.com>